

Nearfield Optical Interactions of Nano-Plasmonic Particle Assemblies

THÈSE N° 5666 (2013)

PRÉSENTÉE LE 23 MAI 2013
À LA FACULTÉ DES SCIENCES DE BASE
LABORATOIRE DE SCIENCE À L'ÉCHELLE NANOMÉTRIQUE
PROGRAMME DOCTORAL EN PHYSIQUE

ÉCOLE POLYTECHNIQUE FÉDÉRALE DE LAUSANNE

POUR L'OBTENTION DU GRADE DE DOCTEUR ÈS SCIENCES

PAR

Moritz ESSLINGER

acceptée sur proposition du jury:

Prof. C. Hébert, présidente du jury
Prof. K. Kern, directeur de thèse
Prof. C. Hafner, rapporteur
Prof. C. Lienau, rapporteur
Prof. O. Martin, rapporteur



ÉCOLE POLYTECHNIQUE
FÉDÉRALE DE LAUSANNE

Suisse
2013

Abstract

This thesis deals with both theoretical aspects of nearfield microscopy as well as experimental investigations of structures, applicable in plasmonic data transport and processing. An imaging theory of apertureless scanning nearfield optical microscopy (aSNOM) is developed directly from Maxwell equations, showing great similarity to the Tersoff-Hamann approach to scanning tunneling microscopy. The theory is applied to experimental recorded images and verifies our empirical findings that the measured quantity in cross-polarized aSNOM is proportional to the z-component of the unperturbed sample nearfield, as in absence of any probe tip. In our experimental implementation of an aSNOM, we outline a rational alignment procedure to suppress background signals to *zero* level, ensuring optimal signal-to-noise ratio.

The instrument is used to characterize various plasmonic systems. We measure the nearfield of optical Yagi-Uda antennas, showing its element coupling and directionality. We further outline a general approach for efficient matching of plasmonic structures to the illumination, placing nearfield couplers in proximity of the structure. As one example, unidirectional launchers of waveguided plasmons are discussed. The dependence of sample excitation on the illumination conditions is studied. On extended samples of amorphously distributed plasmonic scatterers, we find non-local, long range plasmonic interactions, leading to the formation of hotspots.

For next generation plasmonic elements, we extend the search for new materials from materials showing a surface plasmon polariton to polaritons in general. As one example, we show confined nearfield modes in bismuth selenide as well as its applicability for optoelectronic devices in the same volume.

Keywords Plasmonics, Nearfield Microscopy, crosspolarized aSNOM, Reciprocity Theorem, Optical Antennas, Yagi-Uda, Phase Engineering, Unidirectional Plasmon Launchers, Amorphous Plasmonics, Nearfield Coupling, Polaritonics, Bismuth Selenide

Zusammenfassung

Diese Arbeit behandelt sowohl theoretische Aspekte der Nahfeldmikroskopie als auch experimentelle Untersuchungen plasmonischer Strukturen für Datenverarbeitung und -transport. Eine Abbildungstheorie der aperturlosen optischen Rasternahfeldmikroskopie (apertureless scanning nearfield optical microscopy, aSNOM) wird direkt aus den Maxwell Gleichungen entwickelt. Die Beschreibung zeigt große Ähnlichkeit mit dem Ansatz von Tersoff und Hamann zur Rastertunnelmikroskopie. Durch die Theorie werden unsere empirischen Ergebnisse, dass das experimentell gemessene Signal eines kreuzpolarisierten aSNOMs proportional zur z -Komponente des von der Spitzen-Sonde ungestörten Nahfeldes ist, bestätigt. Wir beschreiben den experimentellen Aufbau unseres Nahfeldmikroskops, und wie durch geschickte Justage der Hintergrund im gemessenen Signal auf exakt null reduziert werden kann. Hierdurch wird ein optimales Signal-zu-Rausch Verhältnis erreicht.

Mit diesem Instrument werden verschiedene plasmonische Systeme untersucht. Wir vermessen die optischen Nahfelder von Yagi-Uda Antennen und zeigen die Direktionalität der Antenne sowie die Art der Kopplung zwischen einzelnen Elementen. Außerdem beschreiben wir einen generellen Ansatz zur Anregung plasmonischer Strukturen durch Koppler in der Nähe einer Struktur. Als ein Beispiel werden Strukturen zur unidirektionalen Erzeugung von Plasmonen in Wellenleitern besprochen. Weiterhin wird die Abhängigkeit der Probenanregung von den Beleuchtungsbedingungen untersucht. Auf großflächigen Proben mit amorph verteilten Gold-Nanoscheibchen finden wir eine nichtlokale, langreichweitige Wechselwirkung zwischen den Scheibchen, die zur Bildung von hot-spots (Punkten starker Feldüberhöhung) führt.

Um die Anforderungen an die nächste Generation plasmonischer Strukturen erfüllen zu können, werden neuartige Materialien benötigt. Wir erweitern die Suche nach neuen Materialien von Stoffen, die ein Oberflächen-Plasmon-Polariton zeigen, zu Oberflächen-Polaritonen. Als ein Beispiel zeigen wir Feldlokalisierung auf Sub-Wellenlängenskala in Bismutselenid. Dieses Material ist optisch stark anisotrop und

erlaubt die direkte Kombination mit optoelektronischen Bauteilen im selben Volumen.

Schlagwörter Plasmonik, Nahfeldmikroskopie, kreuzpolarisiertes aperturloses Rasternahfeldmikroskop (aSNOM), Reziprozitätstheorem, optische Antennen, Yagi-Uda, Unidirektionale Plasmonen-Koppler, Amorphe Plasmonik, Nahfeld-Kopplung, Polaritonik, Bismutselenid

Contents

Abstract	iii
Zusammenfassung	vi
1. Introduction	3
2. Imaging Theory of Apertureless SNOM	7
2.1. Motivation	7
2.2. Reciprocity Theory	10
2.2.1. The Reciprocity Theorem	10
2.2.2. The Left Hand Side	11
2.2.3. The ED Terms	12
2.2.4. The HB Terms	14
2.2.5. The Ej Terms	14
2.2.6. Collecting All Terms	14
2.2.7. The Monochromatic, non-Magnetic Case	16
2.3. Angular Spectrum Representation	18
2.4. Evaluation of the Integral	19
2.5. Point-Like Tip Model	21
2.6. Evaluation of the System Response	22
2.6.1. Coupled Dipole Model	25
2.6.2. Crosspolarized aSNOM	26
2.6.3. Reciprocal Crosspolarized aSNOM	29
2.6.4. Horizontal component mapping aSNOM	29
3. Perfect Background Suppression in Apertureless Nearfield Microscopy	35
3.1. The Apertureless Scanning Nearfield Optical Microscope	35

3.2. Alignment and Verification	40
3.3. The Nature of the Phase Singularity	42
4. Optical Antenna Phase Arrays	45
4.1. Feedgap Antennas	45
4.2. Yagi-Uda Antennas	47
4.3. Unidirectional Plasmon Launchers	51
5. Amorphous Plasmonic Systems	57
5.1. Distance Dependence of Interaction Strength	57
5.2. Simulation of the Systems	58
5.3. Illumination Conditions	58
6. Plasmons in Tensorial Media	63
6.1. Introduction	63
6.2. Ellipsometry	64
6.3. Planar Interfaces	66
6.4. Particle Polaritons	68
6.5. Photocurrent on Bismuth Selenide Schottky Diodes	72
6.6. Discussion	74
7. Summary and Outlook	75
Bibliography	79
A. Publications and Curriculum Vitae	101
A.1. Publications	101
A.2. Curriculum Vitae	102

List of publications that are part of this thesis

- W. Khunsin, B. Brian, J. Dorfmueller, M. Esslinger, R. Vogelgesang, C. Etrich, C. Rockstuhl, A. Dmitriev, and K. Kern. *Long-distance indirect excitation of nanoplasmonic resonances*. Nano Letters, **11**(7):2765–2769, 2011. doi: 10.1021/nl201043v.
- J. Dorfmueller, D. Dregely, M. Esslinger, W. Khunsin, R. Vogelgesang, K. Kern, and H. Giessen. *Near-field dynamics of optical Yagi-Uda nanoantennas*. Nano Letters, **11**(7):2819–2824, 2011. doi: 10.1021/nl201184n.
- M. Esslinger, J. Dorfmueller, W. Khunsin, R. Vogelgesang, and K. Kern. *Background-free imaging of plasmonic structures with cross-polarized apertureless scanning near-field optical microscopy*. Review of Scientific Instruments, **83**(3):033704, 2012. doi: 10.1063/1.3693346.
- M. Esslinger and R. Vogelgesang. *Reciprocity theory of apertureless scanning near-field optical microscopy with point-dipole probes*. ACS Nano, **6**(9):8173–8182, 2012. doi: 10.1021/nm302864d.
- Moritz Esslinger, Worawut Khunsin, Nahid Talebi, Tongda Wei, Jens Dorfmueller, Ralf Vogelgesang, and Klaus Kern. *Phase Engineering of Subwavelength Unidirectional Plasmon Launchers*. (submitted)
- Moritz Esslinger, Ralf Vogelgesang, Nahid Talebi, Worawut Khunsin, Pascal Gehring, Stefano de Zuani, Bruno Gompf, and Klaus Kern. *Anisotropic Polaritonics at Optical Frequencies*. (in preparation)

Chapter 1.

Introduction

Surface plasmon polaritons are electromagnetic waves bound to metal-dielectric interfaces.[1] They stem from coupling of a photon to a polariton and achieve sub-wavelength confinement of optical fields. Electric fields in plasmonic structures can be strongly enhanced compared to incident fields, offering applications like ultrasensitive detectors, [2] bio-medical diagnostics and therapeutics. [3]

Plasmonics is also an eminent candidate to meet the requirements for taking the next step in increased communication bandwidths in conventional data processing by using optical carrier frequencies of several hundred THz.[4, 5, 6, 7] Confinement of light to subwavelength regions allows for small optical circuit elements and high integration density.[8] Therefore, plasmonics is being used to put forward optical device miniaturization.[9, 10, 11, 4, 12, 13, 14]

Different wavevectors of photons and plasmons impose a challenge for efficient excitation of plasmonic devices. The wavevector difference must somehow be compensated (see Fig. 1.1). In surface plasmon polariton sensing, often a Kretschmann or Otto configuration is used to excite propagating plasmons on extended surfaces. Here, the large wavevector of light waves in glass is coupled to plasmonic modes. Another way is to use a grating, which can deliver the grating wavenumber in addition to the photon momentum. Also steps, edges and other discontinuities, that are broad in Fourier space, can provide a suitable wavevector to launch plasmons.

Semi-infinite structures, like one-dimensional waveguides, are used for example for data transmission. [15] Subwavelength confinement of light allows for much denser arrays of waveguides than possible with dielectric structures. In recent years, many functional elements implemented in plasmonic waveguides have been developed, ranging from amplifiers [16, 17] and beam-splitters [8] to interferometric logic gate elements. [18] Yet, many of these elements are larger than the light wavelength and still have potential for miniaturization.

Finite sized structures can act as resonators for plasmons with corresponding particle resonances. Modes with a dipolar moment can be directly excited by light. A prominent class of particle plasmon devices are optical antennas. Antennas – in general – are all matching devices from far-field photonic modes to plasmonic ones. [19, 20, 21] The ability of antennas to confine light fields to small regions with a

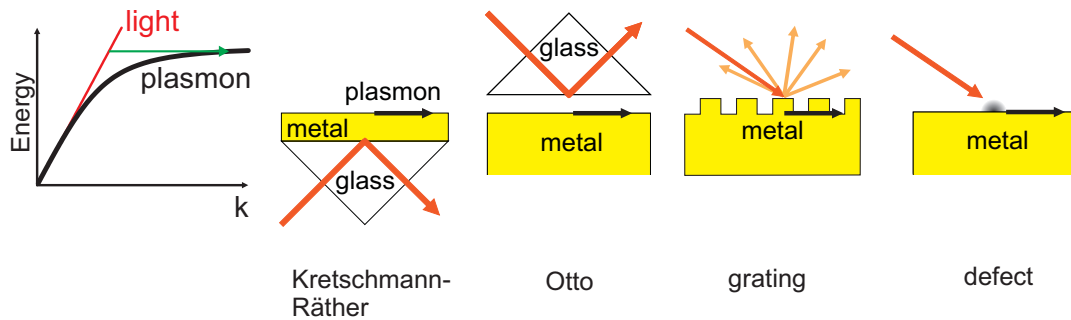


Figure 1.1.: Wavevectors of surface plasmon polaritons and free space light are mismatched. On extended surfaces, plasmons can only be excited if the missing momentum is provided. This can be achieved, for example, in a Kretschmann or Otto configuration, coupling the wavevector of light in glass to a metal-air interface, or by gratings and point-defects on a surface.

high field enhancement makes them ideal structures for sensor applications. [19, 22] Compared to surface plasmon sensors on extended surfaces, they show strong field enhancement in small regions and allow for ultrasensitive optical probing of small sample volumes. [19] Another field of application is optical data transmission, where antennas act as sending or receiving devices and efficiently couple far-field signals to local devices. Recently, complex antenna concepts, like an optical Yagi-Uda antenna, have been successfully demonstrated at optical frequencies. [23, 24] For efficient excitation, structures are optimized in size [25, 26, 12] and shape [27, 28, 29] to the illumination conditions. For complex structures, in general full-field simulations are necessary to optimize the device geometry. For one dimensional (thin) wires, also an analytic description exists. [30] They can be seen as Fabry Perot resonators, [31], with resonances depending on the wire length. [19]

In plasmonic devices, ohmic losses are a challenging drawback, which limit plasmonic devices, - compared to dielectric components, - to relatively short distance applications like on-chip communication [32, 33] or novel quantum plasmonic effects. [34, 35] For next generation plasmonics, new materials are required. [36] Promising candidates have been found, e.g., in doped semiconductors, which act as Drude-metals with tunable plasma frequency [37] and quantum metamaterials [38]. Also other quasi-particles than the plasmon polariton can achieve bound modes of sub-wavelength extent. [39]. This was recently shown in the nearfield for the the phonon polariton. [40] Thus, bound modes are expected for polaritons in general.

Typically, plasmon and other polariton wavelengths are smaller than the light wavelength. To gain understanding of the function of plasmonic devices, high resolution imaging techniques are required. Unfortunately, far field optical imaging techniques are diffraction limited, offering hardly better resolution than half the

light wavelength. In recent years, a number of techniques became available that routinely achieve resolutions of 10 nm at optical energies. [41] Transmission electron microscopy, cathodoluminescence microscopy, and photo electron emission microscopy use electrons for excitation or detection. They take advantage of the high resolution achievable in electron microscopes. However, these techniques can not offer the possibility to measure an optical phase.

Nearfield optical microscopy is an all-optical technique that also achieves high resolution. It breaks the optical diffraction limit by placing a probe in proximity of the sample, accessing near-fields carrying high resolution optical fields. In scanning nearfield optical microscopy (SNOM), a tapered glass fiber with metal coating is used as probe. The probe has a subwavelength aperture, collecting light from a small region on the sample. In apertureless SNOM, a tip with sharp apex is brought in vicinity of the sample and scatters light into the farfield. Deep subwavelength spatial resolution is achieved for example in imaging of local dielectric constant [42] or nearfield distributions of plasmonic samples.[43, 44] Often, a metallic tip is used as the local probe, which interacts strongly with the sample, resulting in detectable farfield scattering of high intensity. For dielectric samples, with an appropriate model for the tip-sample interaction, one can obtain local dielectric constant contrast at a sample surface, i.e., maps of the material composition.[45] For plasmonic structures, however, maps of the local field distribution are at the center of interest. Unfortunately, such samples may themselves exhibit resonant eigenmodes, leading to non-trivial mode hybridization effects between the tip and the sample.[46] This coupling strongly influences the resulting images.[47, 48, 49, 50]

In this thesis, many of the aspects mentioned above are covered. In chapter 2, we derive an exact description for the measurement process in nearfield microscopy, starting from the Maxwell equations. The practical implementation of our apertureless SNOM, measuring the z-component of electric fields on a sample, is described in chapter 3. It achieves perfect background subtraction by a rational alignment procedure employing a cross-polarization scheme. The following chapters discuss the application of apertureless SNOM for characterization of plasmonic devices. In chapter 4, we discuss the coupling of individual elements of an optical Yagi-Uda antenna to constructively excite the central element and provide experimental evidence for its directionality. In the following section 4.3, we use point-like antenna elements in proximity of a structure to convert far-field excitation to plasmonic modes via nearfield coupling. By matching excitation strength, phase, and position to the incident light field, in general a configuration can be found where desired modes on the target structure are excited, while undesired ones are suppressed. As an example for this concept, we experimentally show unidirectional plasmon launchers designed based on this principle. In chapter 5, we discuss the influence of illumination conditions on the sample nearfields. We find that on large-area samples of amorphously distributed plasmonic resonant discs, a long range interaction occurs, that drastically changes the local excitation and has direct implications to the understanding of

the formation of hot-spots. In chapter 6, we propose layered materials like bismuth selenide for polaritonic devices. In bismuth selenide, the negative electric permittivity necessary to apply plasmonic concepts is achieved not by the surface plasmon polariton, but with an exciton polariton. In contrast to most semiconductor materials, the polaritonic relevant energies are well above the semiconductor bandgap, opening new possibilities for optoelectronic devices.

Chapter 2.

Imaging Theory of Apertureless SNOM

Apertureless SNOM offers imaging with deep subwavelength resolution at optical energies. Unfortunately, the high-resolution contrast in apertureless SNOM does not necessarily come with easy, faithful interpretation of recorded images. To beat the diffraction limit, the evanescent nearfields must be accessed by some kind of (scanning) probe.[51] The intricate interaction between an unknown sample under study and the probe is all but fully understood. A detailed model for recorded signals would also be very beneficial in inverse scattering problems.[52, 53] Here we concentrate on scanning nearfield optical microscopy. For a handful of special cases successful models are available, which represent the signal measured in terms of easily understood quantities. [45, 54, 55, 56] In this chapter, we derive an exact, closed form expression for the measured signal in nearfield microscopy, starting from Maxwell equations.

2.1. Motivation

The current situation in SNOM is somewhat reminiscent of scanning tunneling microscopy (STM) in the early 1980ies. Ab initio theories were available but cumbersome to use, and simplified models based on ad hoc assumptions often lead to paradoxical interpretations. This changed, when Tersoff and Hamann provided their celebrated interpretation framework,[57, 58] which allowed STM images to be easily interpreted with certainty and largely without a priori knowledge or further simulations.

In STM the interpretation of recorded signals is based on Bardeen's formula for the current across a tunneling barrier.[59] It presumes weak coupling between the two electrodes referred to as "sample" and "tip". Weak coupling is appropriate for electronic states that decay evanescently into the gap between the electrodes. Tersoff and Hamann proceeded by introducing the simplest conceivable model for a tip, namely a point-like s-wave emitter.[57, 58] Their elegant analytical expression for

the tunneling current showed it is simply proportional to the wavefunction of the bare sample at the location of the point-like tip.

Some of the earliest results in SNOM were inspired by the successes of STM, emulating the evanescent coupling character. Possibly the closest equivalent, albeit somewhat exotic, is the observation of photon-tunneling through a gap filled with liquid metal.[60] Illumination by total internal reflection and pick up by a nearfield probe that frustrates the evanescent fields shares similar evanescent field features with the STM.[61, 62] In the late 1990ies also a number of general and exact descriptions of SNOM have been proposed, which arrive at formulae that closely resemble that of Bardeen.[63] Remarkably, no explicit assumption of weak coupling between sample and tip is necessary in their derivation. In principle, therefore, these formulae do also describe the operation of SNOMs – aperture-based or apertureless – that do not operate in the weak-coupling regime.[64, 42]

The correlation between the general expressions for the electronic tunneling matrix elements and the optical reciprocity relations[65, 66, 67, 68] roots in the intimate relations between the Schrödinger equation and the Maxwell-Helmholtz equation,[69, 70] which are the respective wave equations for the electron and photon. This suggests the possibility of picking up the idea of Tersoff and Hamann of a point-like probe tip for SNOM, as well. We show that it is possible to express recordable signals as an integral of the probing tip volume. Consequently, for apertureless or scattering-type SNOM – which are indeed point-like at the wavelength scale – an analytical, closed-form expression is obtained for the measured signals in SNOM that is analogous to the Tersoff-Hamann results. We demonstrate the utility of this framework in discussing how different forms of apertureless SNOM are used to map local electric field components, and how these are related to the bare sample nearfields.

Bardeen’s formula $M_{\mu\nu} = -(\hbar^2/2m) \int d\vec{S} \cdot (\overline{\psi_\mu} \vec{\nabla} \psi_\nu - \psi_\nu \vec{\nabla} \overline{\psi_\mu})$ describes the flow of charge (or equivalently probability density) across a fictitious plane inserted in the gap between probe tip and sample. An analogon for SNOM has been derived earlier by Carminati, Greffet, and co-workers, who used reciprocity theory in their approach.[65, 66]

Reciprocity describes the relation between two scenarios (1, 2) under reciprocal illumination. [71] Fig. 2.1 displays a typical application for SNOM: in scenario 1 only the tip is present and in scenario 2 both tip and sample. The tip can thus be defined and characterized (in scenario 1) without reference to any sample. This allows unravelling sample properties from the unknown signal generated by the sample being probed (in scenario 2).

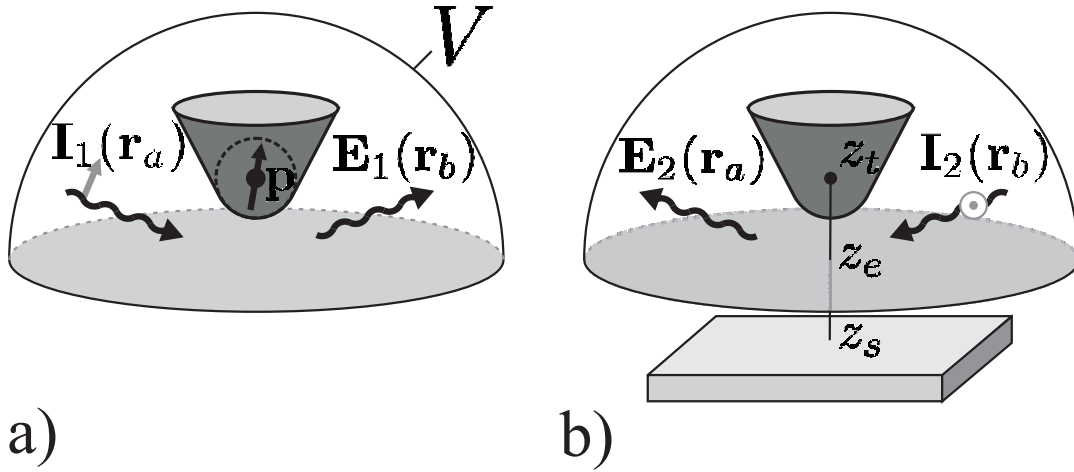


Figure 2.1.: The two reciprocal scenarios. a) In scenario 1, a source \vec{I}_1 at position \vec{r}_a emits radiation, which is scattered by the tip and detected at position \vec{r}_b . b) In the reciprocal scenario 2, an additional sample is present, whose surface right below the probe tip is at height z_s . Source and detector have exchanged their respective roles. A virtual evaluation plane is considered at height z_e in the gap between tip and sample.

To motivate the application of reciprocity theory, it is convenient to draw attention to an often unnoted intimate relation between reciprocity and energy conservation. Indeed, at first sight, the flow of energy across an interface separating a sample from a nearfield probe tip might seem like an opportune candidate to establish an optical analog to the probability flow in Bardeen's case. The flow of energy is represented by the Poynting field $\vec{S} = \vec{E} \times \vec{H}$, and the associated theorem for optical energy conservation is well known.[72] Its close relative, the reciprocity theorem, contains terms of similar shape ($\vec{E}_2 \times \vec{H}_1 - \vec{E}_1 \times \vec{H}_2$). It constitutes a relation between the fields in two scenarios 1 and 2 under different illumination conditions. [73]

To treat energy conservation and reciprocity in the same formalism, we rewrite the Poynting vector as $2\vec{S} = (\vec{E}_2 \times \vec{H}_1 + \vec{E}_1 \times \vec{H}_2)$ with both scenarios being identical. In the following we consider generalized terms ($\vec{E}_2 \times \vec{H}_1 + \zeta \vec{E}_1 \times \vec{H}_2$). This puts reciprocity theory on par with energy conservation. The sign factor $\zeta = \pm 1$ automatically tracks both energy and reciprocity theory, and an explicit choice is made after it has become evident which theorem is best suited.

2.2. Reciprocity Theory

2.2.1. The Reciprocity Theorem

We start from the Maxwell equations in SI units

$$\vec{\nabla} \cdot \vec{D} = \rho \quad (2.1a)$$

$$\vec{\nabla} \times \vec{E} = -\dot{\vec{B}} \quad (2.1b)$$

$$\vec{\nabla} \cdot \vec{B} = 0 \quad (2.1c)$$

$$\vec{\nabla} \times \vec{H} = \dot{\vec{D}} + \vec{j} \quad (2.1d)$$

with the constitutive equations

$$\vec{D} = \hat{\epsilon} \vec{E} \quad (2.2a)$$

$$\vec{B} = \hat{\mu} \vec{H} \quad (2.2b)$$

$$\vec{j} = \hat{\sigma} \vec{E} \quad (2.2c)$$

All material properties are described by unit bearing quantities, i.e., they are *not* measured relative to the vacuum values ϵ_0 and μ_0 . $\hat{\epsilon}$ and $\hat{\mu}$ are the electric and magnetic permittivity, respectively, and $\hat{\sigma}$ the conductivity. By multiplying $\vec{H} \cdot$ with Eq. (2.1b) and $\vec{E} \cdot$ with Eq. (2.1d), one obtains

$$\vec{H}_1(\vec{\nabla} \times \vec{E}_2) = -\vec{H}_1 \dot{\vec{B}}_2 \quad (2.3a)$$

$$\zeta \vec{H}_2(\vec{\nabla} \times \vec{E}_1) = -\zeta \vec{H}_2 \dot{\vec{B}}_1 \quad (2.3b)$$

$$\zeta \vec{E}_1(\vec{\nabla} \times \vec{H}_2) = \zeta \vec{E}_1(\dot{\vec{D}}_2 + \vec{j}_2) \quad (2.3c)$$

$$\vec{E}_2(\vec{\nabla} \times \vec{H}_1) = \vec{E}_2(\dot{\vec{D}}_1 + \vec{j}_1) \quad (2.3d)$$

We add up all equations to

$$\begin{aligned} -\vec{\nabla} \cdot \left(\vec{E}_2 \times \vec{H}_1 + \zeta \vec{E}_1 \times \vec{H}_2 \right) &= \vec{H}_1 \dot{\vec{B}}_2 + \zeta \vec{H}_2 \dot{\vec{B}}_1 \\ &+ \vec{E}_2 \dot{\vec{D}}_1 + \zeta \vec{E}_1 \dot{\vec{D}}_2 \\ &+ \vec{E}_2 \vec{j}_1 + \zeta \vec{E}_1 \vec{j}_2 \end{aligned} \quad (2.4)$$

Here the fields $\vec{E}, \vec{D}, \vec{H}, \vec{B}, \vec{j}$ are all real-valued functions of space and time. The indices 1 and 2 refer to the two, different scenarios, as depicted in Fig. 2.1. In both scenarios, a volume V is considered to enclose the scattering probing tip located at \vec{r}_t . The distribution of material scatterers inside the volume does not change, but the fields are generally very different. In scenario 1 a source \vec{I}_1 at position \vec{r}_a

emits radiation, giving rise to \vec{E}_1 at position \vec{r}_b . In the reciprocal scenario 2 an additional sample is present outside the integration volume. Source and detector have exchanged their places; source \vec{I}_2 at position \vec{r}_b emits radiation, which leads to a field \vec{E}_2 at position \vec{r}_a .

The material operators $\hat{\epsilon}, \hat{\mu}, \hat{\sigma}$ we consider as local functions of space, describing causal responses in time, most easily represented as Kramers-Kronig compatible functions of frequency. This calls naturally for a complex-valued representation, which is carefully introduced by substituting $\vec{E} \rightarrow \Re \vec{E} = 1/2 (\vec{E} + \overline{\vec{E}})$, etc.

By evaluating each term on the left and right hand side of Eq. (2.4) for the scenarios considered here, the reciprocity theorem can be simplified significantly. This is discussed in the following, rather technical paragraphs, resulting in Eq. (2.35).

2.2.2. The Left Hand Side

We first consider the left hand side of Eq. (2.4). It is most convenient for near-monochromatic scenarios [74, 75], such as those excited by narrow-band laser sources, to represent all time-dependent phenomena in frequency space in a narrow band $\Delta\omega$ around a central frequency ω_0 . We represent the fields in both scenarios as

$$\vec{E}_2(t) = \int_{\omega_0 \pm \Delta\omega} d\omega \vec{E}_2(\omega) e^{-i\omega t} \quad (2.5)$$

$$\vec{E}_1(t) = \int_{\omega_0 \pm \Delta\omega} d\omega' \vec{E}_1(\omega') e^{-i\omega' t} \quad (2.6)$$

$$\Re \vec{E}_2 \times \Re \vec{H}_1 = \frac{1}{2} (\vec{E}_2 + \overline{\vec{E}_2}) \times \Re \vec{H}_1 \quad (2.7)$$

$$= \frac{1}{2} \Re (\vec{E}_2 \times \vec{H}_1 + \overline{\vec{E}_2} \times \vec{H}_1) \quad (2.8)$$

$$= \frac{1}{2} \Re \iint d\omega d\omega' \cdot$$

$$\vec{E}_2(\omega) \times \vec{H}_1(\omega') e^{-i(\omega+\omega')t} + \overline{\vec{E}_2(\omega)} \times \vec{H}_1(\omega') e^{-i(\omega'-\omega)t} \quad (2.9)$$

Products of fields from both scenarios split up into terms proportional to $e^{-i(\omega+\omega')t}$, oscillating with (approximately) twice the fundamental frequency ω_0 , and slowly varying terms $e^{-i(\omega'-\omega)t}$, which vary on frequency scales smaller or equal to $\Delta\omega$.

As we show below, for the non-magnetic case $\hat{\mu} = \mu_0$ this term can be further simplified.

2.2.3. The ED Terms

For terms of the form $\vec{E}\dot{\vec{D}}$ in Eq. (2.4), we carefully introduce complex valued fields \vec{E} by

$$\Re\vec{E}_2\Re\dot{\vec{D}}_1 = \frac{1}{2}\Re\left(\vec{E}_2 + \overline{\vec{E}_2}\right)\partial_t\left(\hat{\epsilon}\vec{E}_1\right) \quad (2.10)$$

$$= -\frac{1}{4\pi}\Re\iint d\omega d\omega'\left(\vec{E}_2(\omega)e^{-i\omega t} + \overline{\vec{E}_2(\omega)}e^{i\omega t}\right) i\omega'\hat{\epsilon}(\omega')\vec{E}_1(\omega')e^{-\omega't} \quad (2.11)$$

The sum of both terms $\vec{E}_2\dot{\vec{D}}_1 \pm \vec{E}_1\dot{\vec{D}}_2$ is in complex notation

$$\begin{aligned} \Re\vec{E}_2\Re\dot{\vec{D}}_1 + \zeta\Re\vec{E}_1\Re\dot{\vec{D}}_2 &= -\frac{i}{4\pi}\Re\iint d\omega d\omega' \quad (2.12) \\ &\left(\vec{E}_1(\omega)\left(\zeta i\omega'\hat{\epsilon}(\omega') + i\omega\hat{\epsilon}(\omega)^T\right)\vec{E}_2(\omega')e^{-i(\omega+\omega')t}\right. \\ &\left. + \overline{\vec{E}_1(\omega)}\left(\zeta i\omega'\hat{\epsilon}(\omega') - i\omega\overline{\hat{\epsilon}(\omega)^T}\right)\vec{E}_2(\omega')e^{-i(\omega'-\omega)t}\right) \end{aligned}$$

Without loss of generality, we split up the permittivity in its symmetric and anti-symmetric part $\hat{\epsilon} = \hat{\epsilon}^S + \hat{\epsilon}^{AS}$ or its Hermitian and anti-Hermitian part $\hat{\epsilon} = \hat{\epsilon}^H + \hat{\epsilon}^{AH}$. This algebraic trick allows us to rewrite the transpose of permittivity as

$$\hat{\epsilon}^S = (\hat{\epsilon}^S)^T \quad (2.13)$$

$$\hat{\epsilon}^{AS} = -(\hat{\epsilon}^{AS})^T \quad (2.14)$$

and the transpose conjugate

$$\hat{\epsilon}^H = (\overline{\hat{\epsilon}^H})^T \quad (2.15)$$

$$\hat{\epsilon}^{AH} = -(\overline{\hat{\epsilon}^{AH}})^T \quad (2.16)$$

respectively.

$$\begin{aligned} \Re\vec{E}_2\Re\dot{\vec{D}}_1 + \zeta\Re\vec{E}_1\Re\dot{\vec{D}}_2 &= -\frac{i}{4\pi}\Re\iint d\omega d\omega' \quad (2.17) \\ &\vec{E}_1(\omega)\left(\zeta\omega'\hat{\epsilon}^S(\omega') + \omega\hat{\epsilon}^S(\omega)\right)\vec{E}_2(\omega')e^{-i(\omega+\omega')t} \\ &+ \vec{E}_1(\omega)\left(\zeta\omega'\hat{\epsilon}^{AS}(\omega') - \omega\hat{\epsilon}^{AS}(\omega)\right)\vec{E}_2(\omega')e^{-i(\omega+\omega')t} \\ &+ \overline{\vec{E}_1(\omega)}\left(\zeta\omega'\hat{\epsilon}^{AH}(\omega') + \omega\hat{\epsilon}^{AH}(\omega)\right)\vec{E}_2(\omega')e^{-i(-\omega+\omega')t} \\ &+ \overline{\vec{E}_1(\omega)}\left(\zeta\omega'\hat{\epsilon}^H(\omega') - \omega\hat{\epsilon}^H(\omega)\right)\vec{E}_2(\omega')e^{-i(-\omega+\omega')t} \end{aligned}$$

At first sight, this transformation might seem more complicated than the previous equation. However, in the near-monochromatic limit, we can drop some of the terms, so that only one of the symmetric and antisymmetric part of the permittivity contributes to the equation. (The same holds for the Hermitian and anti-Hermitian terms). For scalar media, antisymmetric and anti-Hermitian parts are zero, so that in this case the equations further simplify.

$$\begin{aligned}
 \Re \vec{E}_2 \Re \dot{\vec{D}}_1 + \zeta \Re \vec{E}_1 \Re \dot{\vec{D}}_2 \approx & - \frac{1}{4\pi} \Re \iint d\omega d\omega' \left(\right. & (2.18) \\
 & \vec{E}_1(\omega) (2i\omega' \hat{\epsilon}^S(\omega') \delta_{\zeta,+1}) \vec{E}_2(\omega') e^{-i(\omega+\omega')t} \\
 & - \vec{E}_1(\omega) (2i\omega' \hat{\epsilon}^{AS}(\omega') \delta_{\zeta,-1}) \vec{E}_2(\omega') e^{-i(\omega+\omega')t} \\
 & + \overline{\vec{E}_1(\omega)} (2i\omega' \hat{\epsilon}^{AH}(\omega') \delta_{\zeta,+1}) \vec{E}_2(\omega') e^{-i(-\omega+\omega')t} \\
 & + \overline{\vec{E}_1(\omega)} i \left(\frac{-\omega' \hat{\epsilon}^{AH}(\omega') + \omega \hat{\epsilon}^{AH}(\omega)}{-i(-\omega + \omega')} \right) \delta_{\zeta,-1} \vec{E}_2(\omega') \partial_t e^{-i(-\omega+\omega')t} \\
 & + \overline{\vec{E}_1(\omega)} i \left(\frac{\omega' \hat{\epsilon}^H(\omega') - \omega \hat{\epsilon}^H(\omega)}{-i(-\omega + \omega')} \right) \delta_{\zeta,+1} \vec{E}_2(\omega') \partial_t e^{-i(-\omega+\omega')t} \\
 & \left. - \overline{\vec{E}_1(\omega)} (2i\omega' \hat{\epsilon}^H(\omega') \delta_{\zeta,-1}) \vec{E}_2(\omega') e^{-i(-\omega+\omega')t} \right)
 \end{aligned}$$

The sums are easily performed $\hat{\epsilon}(\omega') + \hat{\epsilon}(\omega) \approx 2\hat{\epsilon}(\omega')$. Care has to be taken when subtracting two permittivities at similar frequencies. For the fast oscillating terms, the difference averages to zero when integrating over frequency space, integrals over slowly oscillating terms can be rewritten as follows: [75]

$$\begin{aligned}
 \Re \vec{E}_2 \Re \dot{\vec{D}}_1 + \zeta \Re \vec{E}_1 \Re \dot{\vec{D}}_2 & = \frac{1}{2} \Re \partial_t \vec{E}_1 (\hat{\epsilon}^S \delta_{\zeta,+1} - \hat{\epsilon}^{AS} \delta_{\zeta,-1}) \vec{E}_2 \\
 & + \Re i \omega_0 \overline{\vec{E}_1} (\hat{\epsilon}^H \delta_{\zeta,-1} - \hat{\epsilon}^{AH} \delta_{\zeta,+1}) \vec{E}_2 \\
 & + \frac{1}{2} \Re \partial_t \overline{\vec{E}_1} \partial_\omega (\omega \hat{\epsilon}^H \delta_{\zeta,+1} - \omega \hat{\epsilon}^{AH} \delta_{\zeta,-1}) \vec{E}_2 \quad (2.19)
 \end{aligned}$$

in the near-monochromatic limit $0 < \Delta\omega \ll \omega_0$.

2.2.4. The HB Terms

In close analogy to the previous section, we derive the expressions for the terms of the form $\vec{H}\vec{B}$ in Eq. (2.4):

$$\begin{aligned}
 \Re\vec{H}_1\Re\vec{B}_2 + \zeta\Re\vec{H}_2\Re\vec{B}_1 &= \frac{1}{2}\Re\partial_t\vec{H}_2(\hat{\mu}^S\delta_{\zeta,+1} - \hat{\mu}^{AS}\delta_{\zeta,-1})\vec{H}_1 \\
 &+ \Re i\omega_0\overline{\vec{H}_2}(\hat{\mu}^H\delta_{\zeta,-1} - \hat{\mu}^{AH}\delta_{\zeta,+1})\vec{H}_1 \\
 &+ \frac{1}{2}\Re\partial_t\overline{\vec{H}_2}\partial_\omega(\omega\hat{\mu}^H\delta_{\zeta,+1} - \omega\hat{\mu}^{AH}\delta_{\zeta,-1})\vec{H}_1 \quad (2.20)
 \end{aligned}$$

2.2.5. The Ej Terms

When considering the terms $\vec{E}\vec{j}$ in Eq. (2.4), it is advantageous to split the current densities into external source and scattering parts, $\vec{j} = \vec{j}^{(sou)} + \vec{j}^{(sca)}$. We express the scattered current density as $\vec{j}^{(sca)} = \hat{\sigma}\vec{E}$ and obtain

$$\begin{aligned}
 \vec{E}_2\vec{j}_1^{(sca)} + \zeta\vec{E}_1\vec{j}_2^{(sca)} &= \Re\vec{E}_2(\hat{\sigma}^S\delta_{\zeta,+1} + \hat{\sigma}^{AS}\delta_{\zeta,-1})\vec{E}_1 \\
 &+ \frac{1}{2}\Re i\partial_t\overline{\vec{E}_2}\partial_\omega(\hat{\sigma}^{AH}\delta_{\zeta,+1} + \hat{\sigma}^H\delta_{\zeta,-1})\vec{E}_1 \\
 &+ \Re\overline{\vec{E}_2}(\hat{\sigma}^H\delta_{\zeta,+1} + \hat{\sigma}^{AH}\delta_{\zeta,-1})\vec{E}_1 \quad (2.21)
 \end{aligned}$$

2.2.6. Collecting All Terms

As Eq. (2.4) holds at all times, slow and fast oscillating parts on both sides of the equation must be equal independently. Thus, there are four possible equations, namely the fast and slow terms in the energy ($\zeta = +1$) or reciprocity ($\zeta = -1$) theorem.

slow energy conservation

$$\begin{aligned}
 -\Re\vec{\nabla}\left(\overline{\vec{E}_2}\times\vec{H}_1 + \overline{\vec{E}_1}\times\vec{H}_2\right) &= \Re\partial_t\overline{\vec{H}_2}\partial_\omega(\omega\hat{\mu}^H)\vec{H}_1 \\
 &- \Re\overline{\vec{H}_2}2i\omega\hat{\mu}^{AH}\vec{H}_1 \\
 &+ \Re\partial_t\overline{\vec{E}_2}(i\partial_\omega\hat{\sigma}^{AH})\vec{E}_1 \\
 &+ \Re\left(\overline{\vec{E}_1}\vec{j}_{sou2} + \overline{\vec{E}_2}\vec{j}_{sou1}\right) \\
 &+ \Re\partial_t\overline{\vec{E}_1}\partial_\omega(\omega\hat{\epsilon}^H)\vec{E}_2 \\
 &- \Re\overline{\vec{E}_1}(2i\omega\hat{\epsilon}^{AH})\vec{E}_2 \\
 &+ \Re\overline{\vec{E}_2}2\hat{\sigma}^H\vec{E}_1 \quad (2.22)
 \end{aligned}$$

fast energy conservation

$$\begin{aligned}
 -\Re \vec{\nabla} \left(\vec{E}_2 \times \vec{H}_1 + \vec{E}_1 \times \vec{H}_2 \right) = & \Re \partial_t \vec{H}_2 \hat{\mu}^S \vec{H}_1 \\
 & + \Re \vec{E}_2 (2i\omega_0 \hat{\epsilon}^S + 2\hat{\sigma}^S) \vec{E}_1 \\
 & + \Re \left(\vec{E}_1 \vec{j}_{sou2} + \vec{E}_2 \vec{j}_{sou1} \right) \quad (2.23)
 \end{aligned}$$

slow reciprocity theorem

$$\begin{aligned}
 -\frac{1}{2} \Re \vec{\nabla} \left(\overline{\vec{E}}_2 \times \vec{H}_1 - \overline{\vec{E}}_1 \times \vec{H}_2 \right) = & \frac{1}{2} \Re \overline{\vec{H}}_2 (2i\omega \hat{\mu}^H) \vec{H}_1 \\
 & - \frac{1}{2} \Re \partial_t \overline{\vec{H}}_2 \partial_\omega (\omega \hat{\mu}^{AH}) \vec{H}_1 \\
 & + \frac{i}{2} \Re \partial_t \overline{\vec{E}}_2 (\partial_\omega \hat{\sigma}^H) \vec{E}_1 \\
 & + \Re \overline{\vec{E}}_2 \hat{\sigma}^{AH} \vec{E}_1 \\
 & + \frac{1}{2} \Re \left(-\overline{\vec{E}}_1 \vec{j}_{sou2} + \overline{\vec{E}}_2 \vec{j}_{sou1} \right) \\
 & - \frac{1}{2} \Re \partial_t \overline{\vec{E}}_1 \partial_\omega (\omega \hat{\epsilon}^{AH}) \vec{E}_2 \\
 & - \frac{1}{2} \Re \overline{\vec{E}}_1 (-2i\omega \hat{\epsilon}^H) \vec{E}_2 \quad (2.24)
 \end{aligned}$$

fast reciprocity theorem

$$\begin{aligned}
 -\frac{1}{2} \Re \vec{\nabla} \left(\vec{E}_2 \times \vec{H}_1 - \vec{E}_1 \times \vec{H}_2 \right) = & -\frac{1}{2} \Re \partial_t \vec{H}_2 \hat{\mu}^{AS} \vec{H}_1 \\
 & + \Re \vec{E}_2 \hat{\sigma}^{AS} \vec{E}_1 \\
 & + \frac{1}{2} \Re \left(-\vec{E}_1 \vec{j}_{sou2} + \vec{E}_2 \vec{j}_{sou1} \right) \\
 & - \frac{1}{2} \Re \partial_t \vec{E}_1 \hat{\epsilon}^{AS} \vec{E}_2 \quad (2.25)
 \end{aligned}$$

Note that a distinction between fast and slowly oscillating terms is only possible in the near-monochromatic case, considering a finite bandwidth. However, the separated equations for slow and fast terms also hold for the monochromatic case independently.

2.2.7. The Monochromatic, non-Magnetic Case

Here we concentrate on the the exact monochromatic approximation $\Delta\omega \rightarrow 0$. We subsume the conductivity tensor for all scattering media in the dielectric permeability, $\hat{\epsilon} = \hat{\epsilon} - \hat{\sigma}/i\omega$. Further we assume non-magnetic materials $\hat{\mu} = \mu_0$.

$$\begin{aligned}
 & \text{slow energy conservation:} \\
 -\Re \vec{\nabla} \left(\vec{E}_2 \times \vec{H}_1 + \vec{E}_1 \times \vec{H}_2 \right) &= \Re \left(\vec{E}_1 \vec{j}_{sou2} + \vec{E}_2 \vec{j}_{sou1} \right) \\
 & - \Re \vec{E}_1 \left(i\omega \hat{\epsilon}^{AH} \right) \vec{E}_2 \tag{2.26}
 \end{aligned}$$

$$\begin{aligned}
 & \text{fast reciprocity theorem:} \\
 -\Re \vec{\nabla} \left(\vec{E}_2 \times \vec{H}_1 - \vec{E}_1 \times \vec{H}_2 \right) &= \Re \left(-\vec{E}_1 \vec{j}_{sou2} + \vec{E}_2 \vec{j}_{sou1} \right) \\
 & - \Re \partial_t \vec{E}_1 \hat{\epsilon}^{AS} \vec{E}_2 \tag{2.27}
 \end{aligned}$$

Besides the great similarity between slow energy conservation and the fast reciprocity theorem, we notice subtle, yet crucial differences. Whereas we do make no assumptions about the symmetry of the material tensors, the first terms on the right-hand sides of the energy and reciprocity relation contain, respectively, only the anti-Hermitian and anti-symmetric parts. If these terms do not vanish by symmetry, they can pose considerable numerical difficulties in further applications of the equations.

One may choose one or the other, depending on whether the material tensors are hermitian or symmetric, respectively. (Note that this concerns only the inside of the hemispherical volume.) Energy conservation is successfully applied to magneto-optically active and other materials that break (local) time-reversal symmetry.[76] Here we use the reciprocity theorem, as it facilitates dissipative media, which break (optical) energy conservation. These algebraic considerations hint at the underlying deeper symmetries that exist between energy conservation, time-reversal symmetry, and reciprocity.[65]

For non-magnetic materials, we transform the left hand side of Eq. (2.27) using the Maxwell curl equations

$$\vec{E}_1 \times \vec{H}_2 = \vec{E}_1 \times \left(\frac{1}{i\omega_0\mu_0} \vec{\nabla} \times \vec{E}_2 \right) \tag{2.28}$$

$$\vec{\nabla} \left(\vec{E}_1 \times \vec{H}_2 \right) = \frac{1}{i\omega_0\mu_0} \vec{\nabla} \left(\vec{E}_1 \times \left(\vec{\nabla} \times \vec{E}_2 \right) \right) \tag{2.29}$$

$$= \frac{1}{i\omega_0\mu_0} \partial_i (E_{1,j} \partial_i E_{2j} - E_{1,j} \partial_j E_{2,i}) \tag{2.30}$$

$$= \frac{1}{i\omega_0\mu_0} \left((\partial_i E_{1,j})(\partial_i E_{2j}) + E_{1,j} \Delta E_{2j} - (\partial_i E_{1,j})(\partial_j E_{2,i}) \right) \tag{2.31}$$

$$\Re \vec{\nabla} \left(\vec{E}_2 \times \vec{H}_1 - \vec{E}_1 \times \vec{H}_2 \right) = \Re \frac{1}{i\omega_0\mu_0} (E_{2j}\Delta E_{1,j} - E_{1,j}\Delta E_{2j}) \quad (2.32)$$

$$= \Re \frac{1}{i\omega_0\mu_0} \partial_i (E_{2j}(\partial_i E_{1,j}) - E_{1,j}(\partial_i E_{2j})) \quad (2.33)$$

We insert this result in the fast reciprocity relation Eq. (2.27) and integrate over a volume containing the tip. We assume symmetric dielectric functions $\hat{\epsilon}^{AS} = 0$. Employing the Gauss theorem, we transform the integral into a surface integral.

$$- \int dV \vec{\nabla} \left(\vec{E}_2 \times \vec{H}_1 - \vec{E}_1 \times \vec{H}_2 \right) = \int dV \left(\vec{E}_2 \vec{j}_{sou1} - \vec{E}_1 \vec{j}_{sou2} \right) \quad (2.34)$$

$$\frac{1}{i\omega\mu_0} \oint_{\delta V} dS \vec{n}_i (E_{1j}\partial_i E_{2j} - E_{2j}\partial_i E_{1j}) = \int dV \vec{E}_1 \cdot \vec{j}_2^{(sou)} - \vec{E}_2 \cdot \vec{j}_1^{(sou)} \quad (2.35)$$

For point-like current sources, $\vec{j}_{1,2}^{(sou)} = \vec{I}_{1,2}\delta(\vec{r}-\vec{r}_{a,b})$, we can then write the reciprocity theorem as [66]

$$\frac{1}{i\omega\mu_0} \oint_{\delta V} dS \vec{n}_i (E_{1j}\nabla_i E_{2j} - E_{2j}\nabla_i E_{1j}) = \vec{E}_1 \cdot \vec{I}_2 \Big|_{\vec{r}_b} - \vec{E}_2 \cdot \vec{I}_1 \Big|_{\vec{r}_a} \quad (2.36)$$

Formally, this integral is the equivalent of Bardeen's expression for a matrix element of the tunneling current.[59] Bardeen's formula is an approximation for scalar (evanescent) wavefunctions solving the Schrödinger equation. Eq. (2.36) solves the Maxwell equations exactly for vectorial fields, provided the materials inside the integration volume are non-magnetic and have symmetric dielectric tensors.

The great advantage of Eq. (2.36) are the terms on the right-hand-side. The currents are set parallel to the polarizations of the exciting (\vec{I}_2) and the detected (\vec{I}_1) radiation.[77] The electric signal measured in a given experiment is the term $\vec{E}_2 \cdot \vec{I}_1$. The term $\vec{E}_1 \cdot \vec{I}_2$ is an undesired background term that needs careful attention. In many cases it is actually eliminated, e.g., if \vec{r}_b is outside of V , that is, in a transmission type of experiment. The same term also vanishes if $\vec{E}_1 \perp \vec{I}_2$, which is the basis of the so-called cross-polarization scheme.[78]

To apply the reciprocity theorem Eq. (2.36) to SNOM, it is advantageous to choose a half-space confined by a plane parallel to the xy-plane as integration volume (Fig. 2.1). On the upper boundary the surface integral vanishes under the Sommerfeld radiation condition. The remaining integral surface, the evaluation plane, allows for a successful treatment of the most general case in Fourier space.

In close analogy with experiment, the tip is chosen vertically aligned and the evaluation plane in the tip-sample gap. We proceed with computing the fields scattered by the tip alone $\vec{T} := \vec{E}_1|_{z_e}$ and the whole tip-sample system $\vec{S} := \vec{E}_2|_{z_e}$ on the evaluation plane. This is conveniently accomplished in angular spectrum representation.

2.3. Angular Spectrum Representation

Angular spectrum representation is a representation of fields based on a two-dimensional Fourier transform.

$$\vec{E}(\vec{k}_{\parallel}, z) = \frac{1}{2\pi} \iint d^2k_{\parallel} \vec{E}(\vec{r}) \exp(-i\vec{k}_{\parallel}\vec{r}_{\parallel}) \quad (2.37)$$

Fields are displayed by wavevectors \vec{k}_{\parallel} in a plane and by a real space coordinate out of plane. Here, we use the z -axis as out of plane coordinate. In vacuum, the Helmholtz equation constitutes the out-of plane propagation constant k_z

$$k_0^2 = k_{\parallel}^2 + k_z^2 = \omega^2 \mu_0 \epsilon_0 \quad (2.38)$$

Extracting the root of k_z^2 allows both plus and minus sign, which we associate with components traveling upwards ($\xi = +1$) and downwards ($\xi = -1$). The upward and downward travelling field components $E_i^{\xi}(\vec{k}_{\parallel}, z_0)$ can be separated in Fourier space through the use of a projection operator,

$$\begin{aligned} \vec{E}^{\xi}(\vec{k}_{\parallel}, z) &= \frac{\xi k_z - i\partial_z}{2k_z} \vec{E}(\vec{k}_{\parallel}, z) \quad (2.39) \\ k_z &= +\sqrt{k_0^2 - k_{\parallel}^2} \text{ for propagating modes} \\ k_z &= +i\sqrt{k_{\parallel}^2 - k_0^2} \text{ for evanescent modes} \end{aligned}$$

Notice that this requires besides the field in the evaluation plane also its normal derivative. An alternative scheme may be more convenient for certain numerical implementations. If the derivative of the field in the transformation plane is not available, but the fields are known in two parallel planes separated by vacuum, the projections can also be obtained as

$$\vec{E}^{\xi}(\vec{k}_{\parallel}, z) = \xi \frac{\vec{E}(\vec{k}_{\parallel}, z) - \vec{E}(\vec{k}_{\parallel}, z + \Delta z) \exp(-\xi i k_z \Delta z)}{2i \sin(k_z \Delta z)} \exp(-\xi i \vec{k}_{\parallel} \vec{r}_{\parallel}) \quad (2.40)$$

Once the fields are distinguished into their upwards and downwards traveling components, one can propagate them easily from one plane to another:

$$\vec{E}^{\xi}(\vec{k}_{\parallel}, z) = \vec{E}^{\xi}(\vec{k}_{\parallel}, z_0) \exp(\xi i k_z (z - z_0)) \quad (2.41)$$

if both planes z and z_0 are separated by vacuum. Considering both components traveling upwards and downwards, we write the field in angular spectrum representation

as

$$E_i(\vec{r}) = \sum_{\xi=\pm 1} \frac{1}{2\pi} \iint d^2k_{\parallel} E_i^{\xi}(\vec{k}_{\parallel}, z_0) \exp(i\vec{k}_{\parallel}\vec{r}_{\parallel}) \exp(\xi ik_z(z - z_0)) \quad (2.42)$$

2.4. Evaluation of the Integral

In order to solve Eq. (2.36), we use the self-consistent scattered field expression for the tip field,

$$T_i(\vec{r}) = \frac{k_0^2}{\epsilon_0} \int d^3r' T_m(\vec{r}') \Delta\epsilon_{mj}(\vec{r}') \left(1_{ij} + \frac{\nabla_j \nabla_i}{k_0^2} \right) \frac{e^{ik_0|\vec{r}-\vec{r}'|}}{|\vec{r}-\vec{r}'|} \quad (2.43)$$

Here, $\Delta\hat{\epsilon}$ is the difference between the scatterer permittivity and the background medium. The integration volume covers only the finite tip volume, where $\Delta\hat{\epsilon}$ is nonzero. We further employ the the angular spectrum representation of the downwards propagating part of the scalar Green function[79]

$$\frac{e^{ik_0|\vec{r}|}}{|\vec{r}|} = -\frac{i}{8\pi^2} \int d^2\tilde{k}_{\parallel} \frac{1}{\tilde{k}_z} e^{-i\tilde{k}_z r_z} e^{-i\tilde{k}_{\parallel}\vec{r}_{\parallel}} \quad (2.44)$$

Together with the volume equivalent representation [80] for the tip field, we obtain from Eq. (2.36) the exact expression for the measurable SNOM signal. We substitute Eq. (2.43) for \vec{T} and Eq. (2.42) for \vec{S} in Eq. (2.36):

$$\begin{aligned} \vec{E}_1 \cdot \vec{I}_2 \Big|_{\vec{r}_b} - \vec{E}_2 \cdot \vec{I}_1 \Big|_{\vec{r}_a} &= -\frac{i}{8\pi^2} \frac{k_0^2}{\epsilon_0} \frac{1}{i\omega\mu_0} \frac{1}{2\pi} \sum_{\xi=\pm 1} \int d^2r_{\parallel} d^3r' d^2k_{\parallel} d^2\tilde{k}_{\parallel} \\ &\cdot T_m(\vec{r}') \Delta\epsilon_{mj}(\vec{r}') \left(1_{ij} + \frac{\tilde{k}_j \tilde{k}_i}{k_0^2} \right) \frac{1}{\tilde{k}_z} \\ &\cdot \exp(-i\tilde{k}_z(z - z')) \exp(-i\tilde{k}_{\parallel}\vec{r}'_{\parallel}) \exp(i\tilde{k}_{\parallel}\vec{r}_{\parallel}) \\ &\cdot S_i^{\xi}(\vec{k}_{\parallel}, z_0) \exp(\xi ik_z(z - z_0)) \exp(i\vec{k}_{\parallel}\vec{r}_{\parallel}) \\ &\cdot \left(\xi ik_z + i\tilde{k}_z \right) \end{aligned} \quad (2.45)$$

In Fourier space we can conveniently perform the spatial derivatives ∂_z , which are expressed as the factor $(\xi ik_z + i\tilde{k}_z)$ in the above equation. We first evaluate the integral over d^2r_{\parallel}

$$\int_{\delta V} d^2r_{\parallel} \exp(-i\tilde{k}_{\parallel}\vec{r}'_{\parallel}) \exp(i\vec{k}_{\parallel}\vec{r}_{\parallel}) = 4\pi^2 \delta(\vec{k}_{\parallel} - \tilde{k}_{\parallel}) \quad (2.46)$$

This means both wavevectors of the angular spectrum representation of tip field and the whole system are equal in plane $\vec{k}_{\parallel} = \vec{\tilde{k}}_{\parallel}$. The magnitude of the z-component is thus also equal $k_z = \tilde{k}_z$ and the factor $(\xi i k_z + i \tilde{k}_z)$ vanishes for $\xi = -1$: Only the upwards propagating part of the tip-sample system \vec{S}^+ contributes to the integral.[65]

$$\begin{aligned} \vec{E}_1 \cdot \vec{I}_2 \Big|_{\vec{r}_b} - \vec{E}_2 \cdot \vec{I}_1 \Big|_{\vec{r}_a} &= -\frac{i\omega}{2\pi} \int d^3 r' d^2 k_{\parallel} \\ &\cdot T_m(\vec{r}') \Delta \epsilon_{mj}(\vec{r}') \left(1_{ij} + \frac{k_j k_i}{k_0^2} \right) \\ &\cdot \exp(i\vec{k}_{\parallel} \vec{r}'_{\parallel}) \cdot S_i^+(\vec{k}_{\parallel}, z_0) \exp(ik_z(z' - z_0)) \end{aligned} \quad (2.47)$$

We express \vec{k} as spatial derivative of \vec{r}' . This allows later the permutation with the integral over the wavevector $d^2 k_{\parallel}$.

$$\vec{k} = -i\vec{\nabla}' \quad (2.48)$$

$$\begin{aligned} \vec{E}_1 \cdot \vec{I}_2 \Big|_{\vec{r}_b} - \vec{E}_2 \cdot \vec{I}_1 \Big|_{\vec{r}_a} &= -\frac{i\omega}{2\pi} \int d^3 r' d^2 k_{\parallel} \\ &\cdot T_m(\vec{r}') \Delta \epsilon_{mj}(\vec{r}') \left(1_{ij} + \frac{\nabla'_j \nabla'_i}{k_0^2} \right) \\ &\cdot \exp(i\vec{k}_{\parallel} \vec{r}'_{\parallel}) \cdot S_i^+(\vec{k}_{\parallel}, z') \end{aligned} \quad (2.49)$$

We introduce $\vec{S}^+(\vec{r})$ as the synthetic field

$$\vec{S}^+(\vec{r}) = \frac{1}{2\pi} \int d^2 k_{\parallel} \vec{S}^+(\vec{k}_{\parallel}, z) \exp(i\vec{k}_{\parallel} \vec{r}_{\parallel}) \quad (2.50)$$

$$\vec{S}^+(\vec{k}_{\parallel}, z) = \frac{1}{2\pi} \int d^2 r_{\parallel} \vec{S}^+(\vec{r}) \exp(-i\vec{k}_{\parallel} \vec{r}_{\parallel}) \quad (2.51)$$

denoting the back-transformation of the upwards traveling components of \vec{S} in real space. The measured field can thus be written as

$$\begin{aligned} \vec{E}_1 \cdot \vec{I}_2 \Big|_{\vec{r}_b} - \vec{E}_2 \cdot \vec{I}_1 \Big|_{\vec{r}_a} &= -\frac{i\omega}{2\pi} \int d^3 r' d^2 k_{\parallel} \\ &\cdot T_m(\vec{r}') \Delta \epsilon_{mj}(\vec{r}') \left(1_{ij} + \frac{\nabla'_j \nabla'_i}{k_0^2} \right) \exp(i\vec{k}_{\parallel} \vec{r}'_{\parallel}) \\ &\cdot \frac{1}{2\pi} \int d^2 \vec{r}'_{\parallel} S_i^+(\vec{r}'_{\parallel}, z') \exp(-i\vec{k}_{\parallel} \vec{r}'_{\parallel}) \end{aligned} \quad (2.52)$$

We perform the integral over d^2k_{\parallel}

$$\int d^2k_{\parallel} \exp(i\vec{k}_{\parallel}\vec{r}'_{\parallel}) \exp(-i\vec{k}_{\parallel}\vec{r}_{\parallel}) = 4\pi^2\delta(\vec{r}'_{\parallel} - \vec{r}_{\parallel}) \quad (2.53)$$

and obtain

$$\begin{aligned} \vec{E}_1 \cdot \vec{I}_2 \Big|_{\vec{r}_b} - \vec{E}_2 \cdot \vec{I}_1 \Big|_{\vec{r}_a} &= -i\omega \int d^3r \\ &\cdot T_m(\vec{r}) \Delta\epsilon_{mj}(\vec{r}) \left(1_{ij} + \frac{\nabla_j \nabla_i}{k_0^2} \right) S_i^+(\vec{r}) \end{aligned} \quad (2.54)$$

The field \vec{S}^+ is propagated from a plane z_0 above the sample through vacuum to the evaluation plane z_e and further to z . As the whole propagation to the position of tip scattering is entirely in vacuum, $\nabla_i S_i^+(\vec{r}) = 0$ vanishes exactly in source-free space.

Our result for the exact measured signal scattered by an extended tip over a sample is

$$\vec{E}_2 \cdot \vec{I}_1 \Big|_{\vec{r}_a} = \vec{E}_1 \cdot \vec{I}_2 \Big|_{\vec{r}_b} - i\omega \int d^3r \vec{T}(\vec{r}) \Delta\hat{\epsilon}(\vec{r}) \vec{S}^+(\vec{r}) \quad (2.55)$$

where \vec{S}^+ is a synthetic field, denoting the upwards traveling components of the coupled tip-sample field in the evaluation plane, as represented in angular spectrum representation.

Such integrals over small tip volumes are easily manageable with modern numerical Maxwell solvers. One may consider Eq. (2.55) as a fall-back option for delicate cases, or if specifically crafted probe tips deviated significantly from the point-like dipole model, which is considered next.

2.5. Point-Like Tip Model

In the form of Eq. (2.55), reciprocity theory is fully general, applicable to both aperture-based and apertureless versions of SNOM. We now ask, what algebraic simplification and intuitive understanding can be gained, if we restrict ourselves to point-like tips in the apertureless case? Nanoscopic probe tips, in the spirit of the dipole tip model,[64] are often treated as a point-like dipolar moment $\vec{p}(\vec{r}_t) = V_t \vec{T}(\vec{r}_t) \Delta\hat{\epsilon}(\vec{r}_t)$. This replacement turns Eq. (2.55) into the central result of this chapter, the simple scalar relation for the measured signal

$$\vec{E}_2 \cdot \vec{I}_1 \Big|_{\vec{r}_a} = \vec{E}_1 \cdot \vec{I}_2 \Big|_{\vec{r}_b} - i\omega \vec{p}(\vec{r}_t) \cdot \vec{S}^+(\vec{r}_t) \quad (2.56)$$

It is the equivalent of the Tersoff-Hamann formula $I \propto D_t(E_F) |\psi_\nu(\vec{r}_t)|^2$ for the tunneling current in STM. There, the measured signal is proportional to the square-modulus of the sample wavefunction $|\psi_\nu(\vec{r}_t)|^2$ at the location of the tip, multiplied with the density of states D_t of the tip. In close analogy, the detected electric field is proportional to the field $\vec{S}^+(\vec{r}_t)$ at the tip position, projected by the inner product on the dipole moment \vec{p} of the tip. One difference between STM and aSNOM is noteworthy, though: whereas $|\psi_\nu(\vec{r}_t)|^2$ is a property of the bare sample, \vec{S}^+ describes the fully coupled tip-sample system. Therefore, in the following we discuss how the field \vec{S}^+ is related to the unperturbed sample nearfield \vec{S}^{unpert} in the absence of any probe tip.

2.6. Evaluation of the System Response

To evaluate the components of the system field \vec{S} at the evaluation plane which travel upwards, we adopt a Born series treatment of the tip-sample interaction [81]. Diagrammatically, the propagator of the coupled tip-sample system is represented by

$$\begin{aligned}
 \left. \begin{array}{l} \text{Diagram 1} \\ \text{Diagram 2} \end{array} \right\} \vec{S}^0 \\
 + \left. \begin{array}{l} \text{Diagram 3} \\ \text{Diagram 4} \\ \text{Diagram 5} \\ \text{Diagram 6} \\ \dots \end{array} \right\} \vec{S}^- \\
 + \left. \begin{array}{l} \text{Diagram 7} \\ \text{Diagram 8} \\ \text{Diagram 9} \\ \text{Diagram 10} \\ \dots \end{array} \right\} \vec{S}^+
 \end{aligned} \tag{2.57}$$

where the evaluation plane is indicated by the dotted horizontal line and sample and tip interfaces by a solid straight and curved line, respectively. Wiggly arrows represent the well known vacuum propagator

$$\hat{G}_{ij}^0(\vec{r}, \vec{r}') = - \left(1_{ij} + \frac{\vec{\nabla}_j \vec{\nabla}_i}{k_0^2} \right) \frac{\exp(ik_0 |\vec{r} - \vec{r}'|)}{4\pi |\vec{r} - \vec{r}'|} \tag{2.58}$$

Dotted arrows are self-depolarizations of the tip or sample,

$$\hat{\Sigma} = 1 + \text{Diagram 11} + \text{Diagram 12} + \text{Diagram 13} + \dots \tag{2.59}$$

containing all orders of interactions of the sample or tip with itself.

We immediately see that all components traveling upwards are scattered from the sample to the evaluation plane. The total field incident on the sample, however, is influenced by the nearfield probe. The direct contribution \vec{S}^0 of the source \vec{I}_2 may be part of \vec{S}^- or \vec{S}^+ , depending on whether its location \vec{r}_b is above or below

terminated after a suitable low order.

At this point, a cautious note regarding direct scattering from the tip to the detector may be in order. It is one of the major sources of undesired background, as it carries no information about the sample. Any measurable signal that stems directly from the tip is due either to $\vec{S}^0 \in \vec{S}^+$, if the source \vec{I}_2 at \vec{r}_b is located below the evaluation plane, or due to the term $(\vec{E}_1 \cdot \vec{I}_2)$, if \vec{r}_b is above the evaluation plane, inside the integration volume. Thus, this parasitic background signal cannot generally be assumed to vanish, unless special care is taken to ensure exactly normal field vectors, $\vec{E}_1 \perp \vec{I}_2$, [78] or this signal is suppressed by modulation/demodulation techniques to a level below the detector noise floor.

We may terminate the Born series after an appropriate order, for example, in the case of a vanishingly small contribution from the tip, (i.e., $\hat{\alpha}_t \rightarrow 0$, $\hat{\Gamma}_{st} \rightarrow 0$, $\hat{\Sigma}_t \rightarrow 1$). In that case, we find as the lowest order contributions to the measurable signal \vec{S}^+ the bare sample field and the first and second order terms,

$$\vec{S}^{unpert} = \text{[Diagram: Tip and source below plane]} = \hat{\Gamma}_{es} \hat{\Sigma}_s \vec{E}_s^{in} \quad (2.64a)$$

$$\vec{S}^{(1t)} = \text{[Diagram: Tip and source above plane]} = \hat{\Gamma}_{es} \hat{\Sigma}_s \hat{\Gamma}_{st} \hat{\Sigma}_t \vec{E}_t^{in} \quad (2.64b)$$

$$\begin{aligned} \vec{S}^{(2s)} &= \text{[Diagram: Tip and source above plane]} = \hat{\Gamma}_{es} \hat{\Sigma}_s \hat{\Gamma}_{st} \hat{\Sigma}_t \hat{\Gamma}_{ts} \hat{\Sigma}_s \vec{E}_s^{in} \\ &= \hat{\Theta}_{tt} \vec{S}^{unpert}(\vec{r}_t) \end{aligned} \quad (2.64c)$$

In virtually all implementations of aSNOM a modulation/demodulation scheme is employed. By oscillating the tip above the sample, \vec{r}_t varies periodically in time with a frequency Ω . With the evaluation point \vec{r}_t moving, the contributions to the measured signal $\vec{S}^+(\vec{r}_t(t))$ vary. Importantly, this alters \vec{E}_t^{in} , $\hat{\Gamma}_{st}$, and $\hat{\Gamma}_{ts}$ and hence all contributions to \vec{S}^+ . After demodulating the measured signal at the fundamental Ω one still measures considerable parasitic background signal due to \vec{S}^0 or $\vec{E}_1 \cdot \vec{I}_2$. Only by demodulation at the second or higher overtone of Ω these can – with some experimental care [82, 83] – be sufficiently suppressed. To lowest order the recorded signal is thus

$$\vec{E}_2 \cdot \vec{I}_1 \Big|_{\vec{r}_a} \approx i\omega \vec{p}(\vec{r}_t) \left(\vec{S}^{unpert} + \vec{S}^{(1t)} + \vec{S}^{(2s)} \right) \quad (2.65)$$

which confirms the long-established experimental approach.[84]

With the field \vec{S}^+ of the tip-sample system known, we apply Eq. (2.56) to obtain the signal in typically employed experimental schemes for aSNOM. These are commonly classified by polarization configurations of the exciting and scattered radiation at the current sources. By suitably aligned, symmetric optics one can ensure that the radiation has the same polarization at the center of the tip as at the source.

As a demonstration, we choose a sample represented by a set of scattering points in vacuum. Already in this simple model, we can quantitatively compare signal contributions from different terms of the Born series Eq. (2.63a) and learn which terms contribute to the signal in the general case. From the analytic relation of each term to the unperturbed field, measured signals on unknown samples are intuitively interpretable.

2.6.1. Coupled Dipole Model

The coupled dipole model considers situations, where the radiation at the tip from both \vec{I}_1 and \vec{I}_2 is parallel polarized. Both sources are assumed to be located at the same location $\vec{r}_a = \vec{r}_b$ inside the integration volume V . With additional assumptions regarding the reflection of the incident radiation at the sample interface[85, 86, 87, 88] and the actual shape of an elongated tip it is possible to approach a quantitative description. For situations where the probe tip is located above a flat, featureless substrate surface, the interaction of the tip with the surface is analytically described by the quasi-static coupled dipole model, whose most sophisticated version was given by Cvitkovic et al.[45]. For a point-like tip of polarizability α , the field scattered by the whole tip-sample system upon illumination with vertically polarized light is found proportional to

$$\vec{E}^{(sca)} \propto (1 + r_p)\alpha \left(1 - \frac{1}{16\pi R^3}\beta\alpha\right)^{-1} \times \left(r_p\vec{E}_s^{in} + \vec{E}_t^{in}\right) \quad (2.66)$$

where α is the polarizability of the tip, β and r_p the quasi-static and Fresnel reflection coefficients of the sample surface, respectively, and R is the height of the tip above the surface. An equivalent expression is found for the case of horizontally polarized radiation.

We recognize the great similarity to Eq. (2.63b). In Eq. (2.66) the contributions due to \vec{S}^0 and $\vec{E}_1 \cdot \vec{I}_2 \Big|_{\vec{r}_b}$ are not considered, as they are filtered out from the measured signal by demodulation, as discussed above. Both relations contain the full Born series of interactions, which allows extracting information about the material constants of the sample immediately underneath the tip. As no termination of a Born series is necessary, in this case any probing tip may be used, regardless of the strength of its influence on the sample, as long as the signal remains measurable.

An advantage of Eq. (2.63b) for future investigations is the possibility to extract more detailed information regarding the experimental conditions, such as the size of the lateral area over which the tip sample interaction effectively averages, or how exactly the signal evolves as the tip moves laterally over a material contrast boundary or some topography changes, etc. For extended analysis of the influence

of finite sized tips, Eq. (2.63) can be used in conjunction with the Eq. (2.55) instead of Eq. (2.56) for point-like tips.

2.6.2. Crosspolarized aSNOM

In the cross-polarized aSNOM configuration, the current source \vec{I}_1 in scenario 1 and the scattered field $\vec{E}_1(\vec{r}_a)$ are both p-polarized. If \vec{I}_2 is s-polarized, i.e., $\vec{E}_1 \cdot \vec{I}_2 = 0$, then according to Eq. (2.56) the recorded signal simplifies to

$$\vec{E}_2 \cdot \vec{I}_1 \Big|_{\vec{r}_a} = -i\omega \vec{p}(\vec{r}_t) \cdot \vec{S}^+(\vec{r}_t) \quad (2.67)$$

regardless of the location of \vec{r}_b . We assume the tip to be isotropic in the xy plane and mainly polarizable along the z -axis. Choosing a grazing incidence excitation of the tip, its dipole \vec{p} in scenario 1 is mainly vertically polarized. The measurement is thus sensitive mainly to the z -component of the field \vec{S}^+ of the tip-sample system in scenario 2. It is not clear at this point, though, what the disturbance due to the presence of the tip is. To this end we relate \vec{S}^+ to the field due to an unperturbed sample \vec{S}^{unpert} , in the absence of any probe tip.

We place the evaluation plane infinitesimally below the tip position. Under the assumption of a strongly anisotropically polarizable tip ($\hat{\alpha}_{tz} \gg \hat{\alpha}_{tx,y}$), the contribution $\vec{S}^{(1t)}$ to the signal becomes negligible, as the field \vec{E}_t^{in} incident at the tip induces hardly any polarization. The Born series is dominated by \vec{S}^{unpert} and $\vec{S}^{(2s)}$.

The measured signal is thus proportional to $\vec{S}^+ \approx (1 + \hat{\Theta}_{tt})\vec{S}^{unpert}(\vec{r}_t)$. The interaction tensor $\hat{\Theta}_{tt}$ involves multiple three-dimensional convolutions, its exact nature is an intricate function of sample and tip geometry and will have to be subject to further detailed investigations [89]. For weak tips $\hat{\Theta}_{tt} \ll 1$, the measured signal is proportional to the unperturbed field, convoluted with an lock-in demodulation effect.

To analyze this effect, we perform numerical simulations for tip and sample consisting of point-like dipoles. For computing optical scattering signals one first considers the source currents in scenario 1 and evaluates the tip dipole moment \vec{p} . In the second scenario, one considers currents in the place of the detector to excite scattered response fields at the location of the source. This may at first seem somewhat counter-intuitive. By combining the two scenarios, however, it is possible to establish a relation that directly represents the experimentally measured signal. The exact geometry of illumination and detection path is represented by the tensorial connection between source current $\vec{I}_{1,2}$ and incident field on tip and sample. In the simulation, we assume collimation optics for the point Sources $\vec{I}_{1,2}$ inside the integration volume. The illumination of the sample in scenario 2 is a plane wave of same polarization as the sources, making this tensor a multiple of the unit operator. The angle of illumination is 70° from the surface normal.

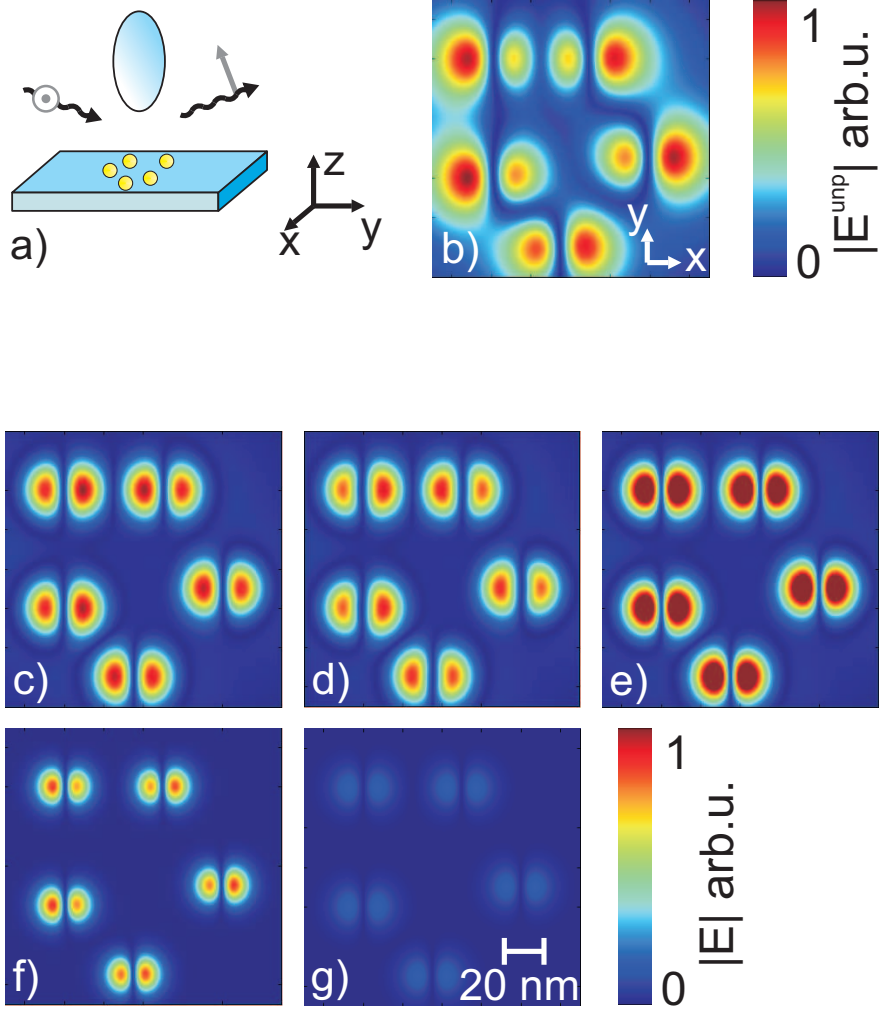


Figure 2.2.: Simulation of signal components in cross-polarized aSNOM at $\lambda = 1064$ nm for the special case of a point like tip and sample. (a) shows a sketch of the aSNOM configuration. A set of point-like dipoles representing spherical gold colloids is scanned by an anisotropic point-like tip, representing a silicon ellipsoid. Displayed are the z -components of (b) the unperturbed sample field \vec{S}^{unpert} in the absence of any probe tip, compared to (c) the full Born series signal \vec{S}^+ , (d) the approximated signal, which is the coherent sum of (e) \vec{S}^{unpert} , (f) $\vec{S}^{(1t)}$, and (g) $\vec{S}^{(2s)}$, deconvoluted at the second overtone of the tip oscillation frequency. Each colloid responds with two lobes of opposite optical phase.

To motivate further the application of reciprocity theory, we apply the field of the tip-sample system to the case of a sample consisting of point-like scatterers in vacuum. The scatterer polarizabilities represent spherical gold colloids of 10 nm diameter. The refractive index of gold at 1064 nm wavelength is taken from Johnson and Christy [90]. The tip-sample distance is 25 nm. The polarizability of the tip is assumed to be the same as a 10 nm diameter sphere of silicon for the in-plane components. We chose that value according to the data sheet of typical silicon tips employed in our experimental setup (ATEC-NC, Nano and More). In Figs. 2.2,2.4, we chose the out-of plane component of the tip polarizability 10 times as large as the in-plane components. In Fig. 2.5, the magnitude of dipolar moment is equal between individual tips $p_{x a,b} = p_{z c,d}$.

The (complex valued) measured signal at the second overtone of the tip oscillation frequency is proportional to

$$\vec{E}_2 \cdot \vec{I}_1 \Big|_{2\Omega} \propto \int_0^{2\pi/\Omega} dt \vec{p}(\vec{r}_t(t)) \cdot \vec{S}^+(\vec{r}_t(t)) \cdot \exp(2i\Omega t) \quad (2.68)$$

We plot the absolute value of the signal. The field incident on the tip in scenario 1 changes with the oscillating tip position. The dipolar moment \vec{p} changes with time, and also portions of \vec{S} changing linearly with tip-sample distance contribute to the signal. This includes far-field scattering of a substrate-air interface. The images in Fig. 2.2 are a demonstration of the Green function ansatz for discrete sample dipoles to show the Born series may be terminated after few orders.

Deconvoluting the signal at an overtone of the tip oscillation adds an additional spatial decay in the measured signal (compare Fig. 2.2b,e). In the limit of infinitesimally small tip oscillation amplitudes, the signal recorded at the n -th overtone is proportional to the $\partial^n / \partial z^n$ derivative of the field.[91] The recorded \vec{S}^+ image appears spatially sharpened relative to the unperturbed field image \vec{S}^{unpert} . This is particularly prominent if both objects and tips are point-like. Also at the edge of sample structures one may observe in cross-polarized aSNOM a more abrupt signal change than is actually present in \vec{S}^{unpert} . Above extended sample regions, which vary smoothly on the scale of the tip size and exhibit slowly varying fields, the spatial contrast enhancement mentioned above is less pronounced.

These considerations are illustrated in Fig. 2.2. Contrasting Fig. 2.2c and Fig. 2.2d affirms that the full Born series is well represented by the first order approximation Eq. (2.65), which in turn is dominated by \vec{S}^{unpert} and $\vec{S}^{(2s)}$ (Fig. 2.2f). The strongly z -polarizable tips conveniently used in cross-polarized aSNOM usually make the contribution $\vec{S}^{(1t)}$ to the full signal much weaker (Fig. 2.2e). This analysis confirms that images obtained with cross-polarized aSNOM are good linear representations of the unperturbed bare sample fields. This is in agreement with the empirical finding that aSNOM in cross polarization produces nearfield optical maps that are very well reproduced by simulated nearfield images of the bare substrate in the absence of any probing tip.[92, 31, 30, 93, 24]

2.6.3. Reciprocal Crosspolarized aSNOM

The reciprocal configuration of crosspolarized aSNOM is similar to crosspolarized aSNOM, but uses p -polarized light to illuminate tip and sample and detects s -polarized light. As both beams are orthogonally polarized, Eq. (2.67) holds also for this configuration. For weakly scattering tips, we sort the terms of the coupled tip-sample system Eq. (2.57) by orders of the tip polarizability. In analogy to the crosspolarization configuration, we find the relevant terms are identical to the ones in the cross-polarization scheme, with all Green functions multiplied in inverse order. We invert the multiplication order exploiting the symmetry of the Green function Eq. (2.58)

$$\hat{G}_{ij}^0(\vec{r}, \vec{r}') = \hat{G}_{ji}^0(\vec{r}, \vec{r}') = \hat{G}_{ij}^0(\vec{r}', \vec{r}) \quad (2.69)$$

to commute the terms. In reciprocal crosspolarization, we obtain the very same signal in optical amplitude and phase as in normal crosspolarization configuration (see Fig. 2.3). The measured signal is thus proportional to the z -component of the unperturbed field on the sample as if the sample was illuminated with s -polarized light. This result is also expected in reciprocity theory considering an apertureless SNOMs in crosspolarization configuration and replacing laser source and detector.

2.6.4. Horizontal component mapping aSNOM

Recently, Hillenbrand et al. introduced another aSNOM configuration to measure horizontal electric fields.[94] The approach is somewhat similar to the coupled-dipole scenario, in that both incident and analyzed radiation have the same polarization. However, in the present case they are s -polarized, which for very weakly s -polarizable probe tips generates an intricate interplay between the sample and the tip that is necessarily vectorial in nature.

Experimentally, two variations have been demonstrated. In transmission geometry, \vec{r}_b is below the evaluation plane and Eq. (2.56) takes the form of Eq. (2.67),

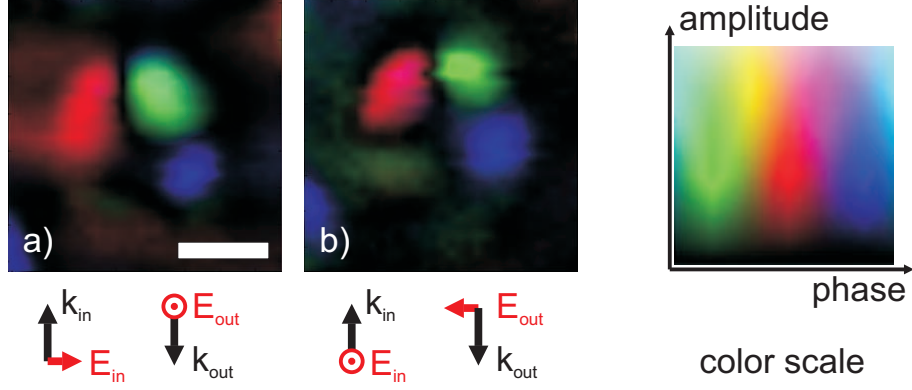


Figure 2.3.: Experimental nearfield images of a quadrupolar resonant gold disc in (a) crosspolarization configuration with incident s-polarized radiation and detection of the p-polarized scattered light and (b) inverted crosspolarization configuration with an p-polarized incident beam and detection of s-polarized light. Scale bar is 250 nm.

but includes an upward-propagating direct excitation $\vec{S}^0 \in \vec{S}^+$. In back-reflection geometry,[95] $\vec{r}_a = \vec{r}_b$ are both inside the integration volume, giving the measurable signal the form the full Eq. (2.56). Here, the direct illumination does not contribute, since $\vec{S}^0 \in \vec{S}^-$.

We may again assume the experimentally relevant case of a point-like tip that is mostly polarizable in the vertical direction, $\hat{\alpha}_{tz} \gg \hat{\alpha}_{tx,y} > 0$, but it must not be completely unpolarizable in the horizontal direction. Otherwise the s-polarized dipole component $\vec{p}(\vec{r}_t)$ picked up at the location of the tip would vanish, and no measurable signal could be recorded.

In Fig. 2.4, simulated nearfield images showing the individual contributions to the signal are displayed. Except for projecting out the x component, the simulations are performed with parameters identical to the cross-polarized configuration of Fig. 2.2. Note that whereas Figs. 2.2c-g are displayed with a common color scale, as are Figs. 2.4c-g, these colorscales differ between these two cases by about one order of magnitude. Mainly due to the assumed stronger vertical polarizability of the probe tip, the recordable signals are stronger in the cross-polarized case.

The comparison of Figs. 2.4c,d shows that, as in the case of cross-polarized aSNOM, the full Born series is well approximated by the two lowest relevant orders, following Eq. (2.65). Evidently, with the simulation parameters chosen in Fig. 2.4, the approximated field is dominated by the unperturbed field. For stronger interacting tips, also the higher order terms $\vec{S}^{(1t)}$ and $\vec{S}^{(2s)}$ will contribute to the signal significantly.

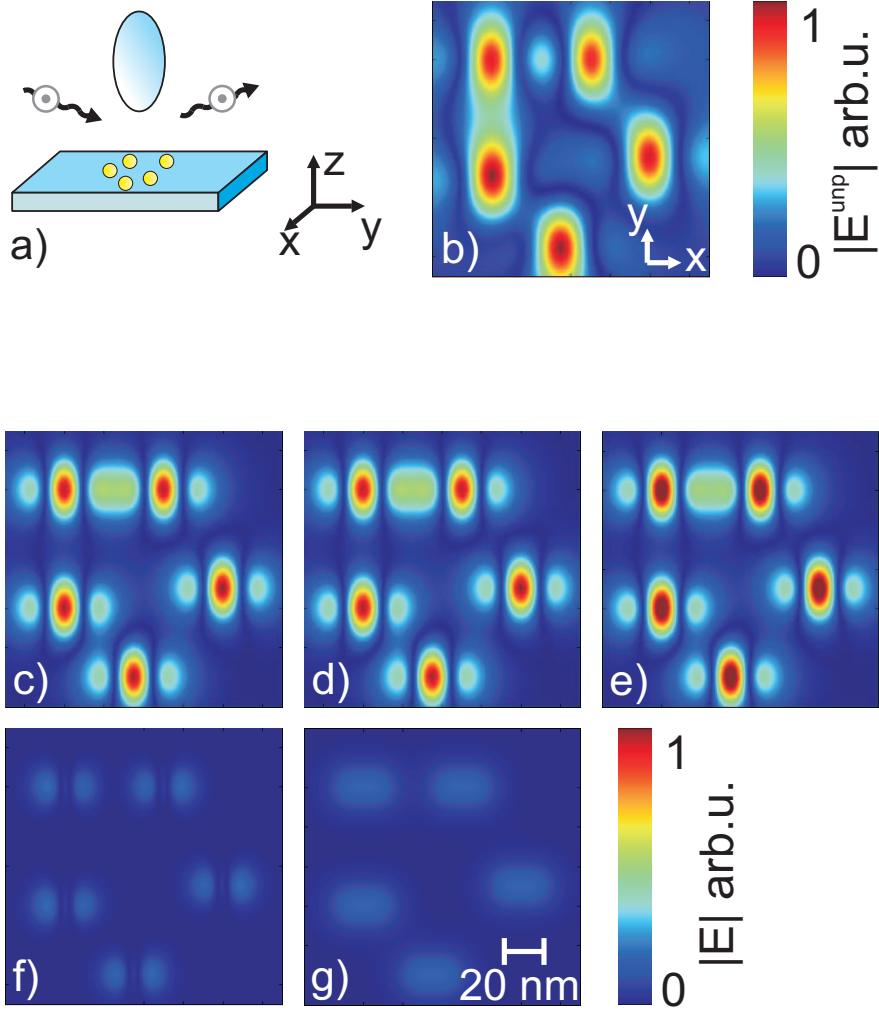


Figure 2.4.: Simulation of signal components obtained with horizontal component mapping aSNOM. (a) shows a sketch of the aSNOM configuration. Except for projecting out the s-polarized component, the simulations were performed with parameters identical to the crosspolarized configuration of Fig. 2.2. Displayed are the x -components of (b) the unperturbed sample field \vec{S}^{unpert} in the absence of any probe tip, and (c) the full Born series signal \vec{S}^+ , (d) the approximated signal, which is the coherent sum of (e) \vec{S}^{unpert} , (f) $\vec{S}^{(1t)}$, and (g) $\vec{S}^{(2s)}$, deconvoluted at the second overtone of the tip oscillation frequency. The response of each colloid is dominated by a central lobe, except for (f), where this lobe is symmetry-forbidden. For a single colloid, all terms are symmetric in amplitude and phase to a vertical axis through the center of the colloid. We discard the background term $\vec{E}_1 \cdot \vec{I}_2 \Big|_{\vec{r}_b}$ of Eq. (2.56).

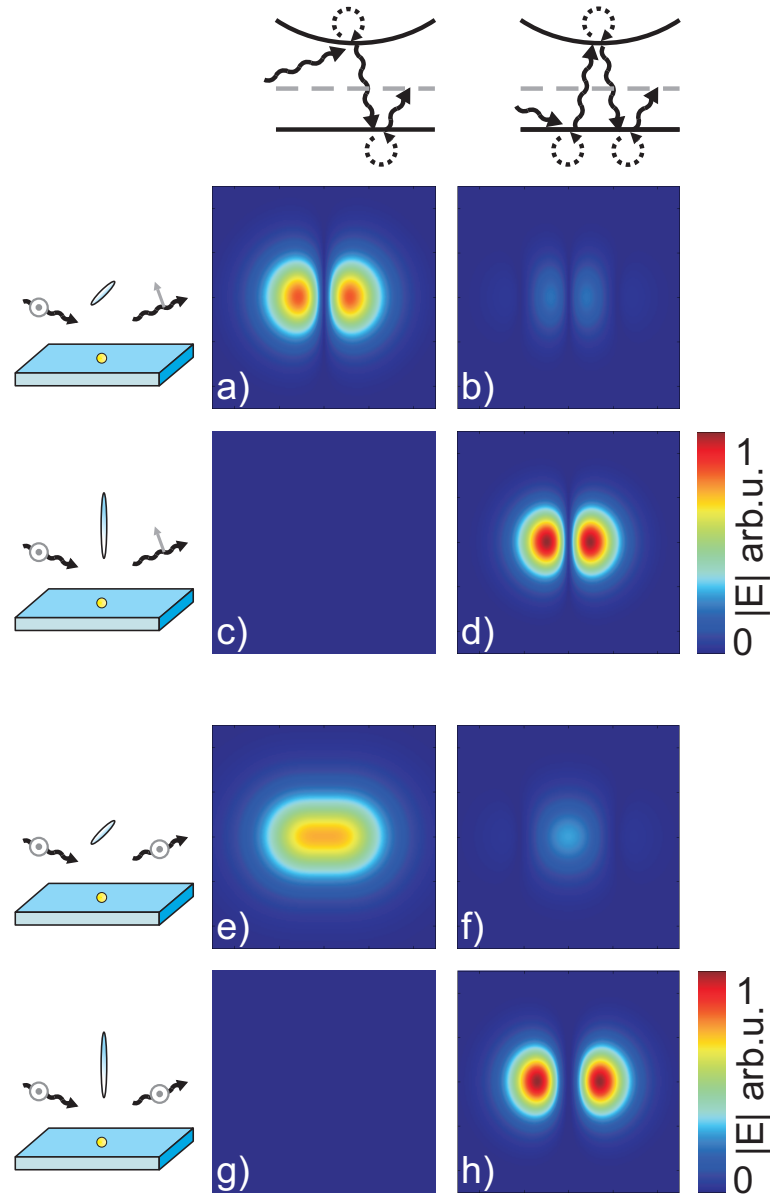


Figure 2.5.: Comparison of the first order contributions to the field \vec{S}^+ picked up by differently polarizable tips in different aSNOM configurations. All images show a point-like dipole representing a spherical gold colloid of 10 nm diameter, scanned by a point-like tip polarizable exclusively in x -direction (a,b,e,f) or in z -direction (c,d,g,h) by the same magnitude. The excitation is always assumed to be s-polarized radiation of 1064 nm wavelength. (a-d) show cross-polarized aSNOM images, (e-h) show horizontal component mapping aSNOM images. The left row (a,c,e,g) shows the $\vec{S}^{(1t)}$ contribution, the right row (b,d,f,h) shows $\vec{S}^{(2s)}$.

Both terms $\vec{S}^{(1t)}$ and $\vec{S}^{(2s)}$ can be of the same order and contribute coherently to the measured signal (Fig. 2.4e,f) in very different forms. To explore this situation further, we compare numerical aSNOM images generated with exclusively z - or x -polarizable tips in Fig. 2.5. For both cross-polarized and horizontal component mapping aSNOM z -polarizability exclusively contributes to $\vec{S}^{(2s)}$ (Figs. 2.5d,h). S-polarized incident light cannot excite the tip, and $\vec{S}^{(1t)}$ vanishes in these cases (Fig. 2.5c,g). Horizontal polarizability predominantly contributes to the signal term $\vec{S}^{(1t)}$, excited by light incident on the tip (Fig. 2.5a,e). However, the $\vec{S}^{(2s)}$ components are not zero in these cases (Fig. 2.5b,f). For probe tips predominantly polarizable in x -direction, $\vec{S}^{(2s)}$ can be suppressed in favor of $\vec{S}^{(1t)}$. [96]

Note that the aSNOM image presented in Fig. 2.5h only appears to be of dipolar character. Both lobes are symmetric in amplitude and phase and the central node line occurs for symmetry reasons. According to Eq. (2.64c) it represents the unperturbed field \vec{S}^{unpert} , convoluted with $\hat{\Theta}_{tt}$. In the yz symmetry plane of an excited x -dipole, however, no coupling to a z -polarizable tip is possible and $\hat{\Theta}_{tt}$ vanishes. The signal due to $\vec{S}^{(1t)}$ (Fig. 2.5e) is favorable in this respect. According to Eq. (2.64b), however, this signal represents not the unperturbed response of the sample to the field \vec{E}_s^{in} directly incident on the sample. Rather it represents a different sample response to an excitation emitted indirectly by the tip, $\vec{E}_s^{in} = \hat{\Gamma}_{st} \hat{\Sigma}_t \vec{E}_t^{in}$.

Chapter 3.

Perfect Background Suppression in Apertureless Nearfield Microscopy

In this chapter, we present advances in experimental techniques of apertureless scanning near-field optical microscopy (aSNOM). We outline a rational alignment procedure, which is based upon a phase singularity that occurs when scanning polarizers around the nominal cross-polarized configuration of s-polarized excitation and p-polarized detection. We discuss the theoretical origin of this topological feature of the setup, which is robust against small deviations, such as minor tip misalignment or shape variations. Setting the polarizers to this singular configuration point eliminates all background signal, allowing for reproducible plasmonic eigenmode mapping with optimal signal-to-noise ratio.

3.1. The Apertureless Scanning Nearfield Optical Microscope

Apart from perturbation of the sample by the nearfield probe, as discussed in the previous chapter, there is a second experimental challenge in apertureless nearfield microscopy: Both illumination and collection from the tip are diffraction limited, and large sample regions around the tip apex as well as the tip shaft scatter light to the detector. aSNOM is often plagued by background signal, which might even obscure any signal carrying information from the nearfield region. Under favorable circumstances it is possible to clean up recorded data by numerical postprocessing, but the resulting nearfield images are usually of inferior quality.[78] In order to achieve highest signal-to-noise ratios (SNR), a systematic approach is much desired to eliminate this background already at the time of recording.

In this section, we concentrate on the instrumentation and procedural aspects that facilitate the optimal alignment of aSNOM. We achieve nearly perfect background suppression using a topological singularity in the polarization phase space. Our rational alignment procedure results in routine, direct measurements of nearly unperturbed plasmonic eigenmodes with excellent quality.

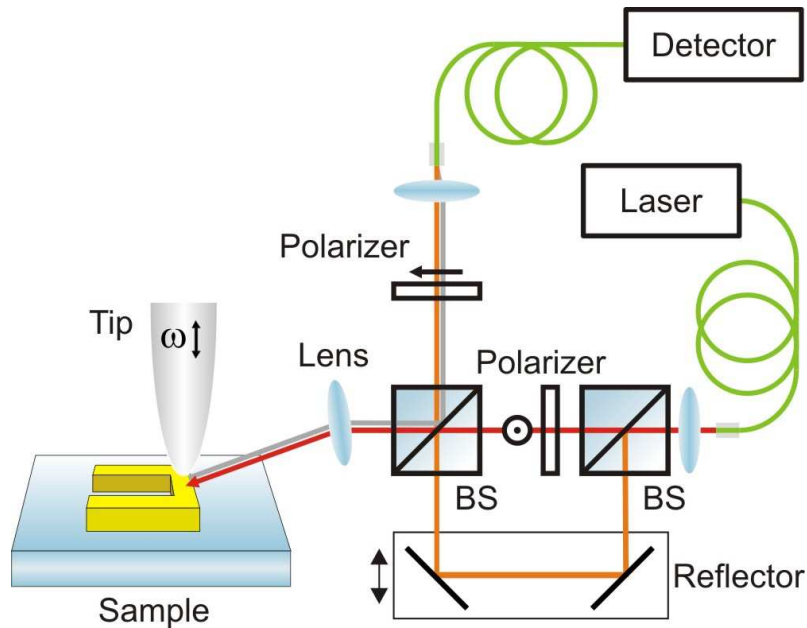


Figure 3.1.: Scheme of the experimental setup. Focused s-polarized radiation excites the sample. Backscattered light is modulated by the tip oscillation, polarization-analyzed in a cross-polarization scheme and interferometrically amplified before it is sent to a detector. The beamsplitters (BS) form a Mach-Zehnder type of interferometer.

Our setup is based on a commercial atomic force microscope (AFM, M5 Park Scientific). [78, 30, 97] We use a non-contact mode AFM tip to scatter local nearfields from a small sample region around the tip position (see Fig. 3.1). After a short review of standard aSNOM instrumentation techniques we employ, we give a detailed description of our implementation of a cross polarization scheme. [98, 78]

It is well known that a modulation–demodulation scheme facilitates the discrimination of nearfield signal against parasitic background signals [42, 83]: to this end, a lock-in amplifier is locked to the AFM cantilever deflection signal. Filtering the optical signal at a suitable harmonic of this frequency efficiently extracts the (spatially non-linear) nearfield contributions. Care has to be taken that no mechanical anharmonicities are present [99, 82].

In addition, we use a confocal arrangement for the optical microscopic detection path, where radiation is collected only from the diffraction limited image volume of a spatial filter centered at the tip apex. Single mode optical fibers (Thorlabs 780HP) provide convenient apertures for both delivering light from the laser source to the setup as well as from the setup to the detector. The light from the fiber is collimated into a 6 mm wide beam, which is focused on the tip by an aspheric lens (Geltech, 0.25 NA). The light scattered back is collimated by the same objective and sent onto

a fiber launch system (Thorlabs MBT613/M), which focusses on a fiber connected to the detector. Piezo positioners in the fiber launch system allow for easy adjustment of the fiber. The fiber also maximizes visibility of the interferometrically detected signal discussed below, as it acts as a nearly perfect spatial filter [100, 101, 102]. The radiation finally impinges on a PIN diode (FEMTO, HCA-S).

The combination of filtering techniques introduced above significantly reduces the total signal intensity. The damage threshold of the tip limits the illumination intensity to about 0.5 MW/cm^2 . [98] This limits the light intensity scattered from the nearfield region onto the detector. Additionally, the detector and amplifier bandwidths have to be higher than the AFM cantilever frequency and its higher harmonics. Signal strengths are often hardly above the noise-level of typical high-bandwidth, linear detectors. A standard way to overcome this is an optical amplification scheme [42]. The weak signal carrying beam $I^{(\text{sig})}$ is interferometrically mixed with a stronger reference beam $I^{(\text{ref})}$. The detected light has the intensity:

$$I = I^{(\text{sig})} + I^{(\text{ref})} + 2\Re\left(\mathbf{E}^{(\text{sig})}\overline{\mathbf{E}^{(\text{ref})}}\right) \quad (3.1)$$

The first term, $I^{(\text{sig})}$, is much weaker than the other terms and becomes negligible. The static $I^{(\text{ref})}$ does not contain any modulation and is filtered by the lock-in analyzer. In analogy to the local oscillator model in radio electronics [103], the remaining cross term denotes (the real part of) the amplified signal. Its intensity is proportional to the electric field of the backscattered light. Besides amplifying the signal, the reference beam also introduces additional noise to the detected signal. For an ideal linear detector, the standard deviation σ is determined by the shot noise $\sigma = \sqrt{\langle n \rangle} \propto \sqrt{I}$ for an average flux of $\langle n \rangle$ photons per unit time interval [104, 105] of all photons on the detector I . The signal is determined solely by the term $\mathbf{E}^{(\text{sig})}\overline{\mathbf{E}^{(\text{ref})}}$. Therefore, the maximum reachable signal-to-noise ratio (SNR) becomes independent of $I^{(\text{ref})}$: [98]

$$\text{SNR} \propto \frac{\sqrt{I^{(\text{sig})}}\sqrt{I^{(\text{ref})}}}{\sqrt{I}} \approx \sqrt{I^{(\text{sig})}} \quad (3.2)$$

in the limit $I^{(\text{sig})} \ll I^{(\text{ref})}$. Once the signal is amplified above the noise level of the detector-amplifier system, the SNR cannot be improved any further. Increasing the reference beam intensity becomes even detrimental to the SNR, namely, when the detector is driven into its non-linear regime. Thus, any improvement in signal quality must be achieved by other means – in our case through the careful optimization of the cross polarization condition.

In our setup, we use a Mach-Zehnder-type interferometric amplification scheme (see Fig. 3.1). After splitting off the reference beam, the excitation beam is polarized to the s-state by Glan-Taylor prism. A second polarizer selects the p-component

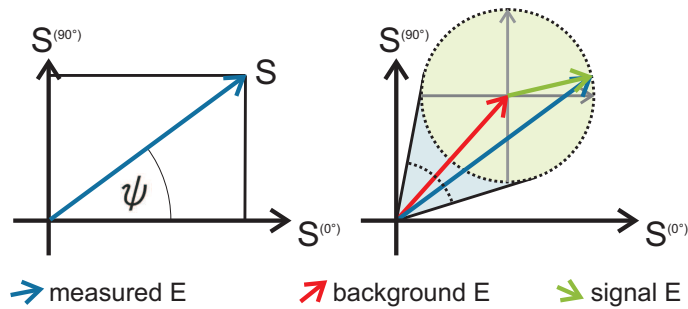


Figure 3.2.: A homodyne measurement consists of two values taken at different interferometric path differences. From those values, the complex valued signal can be reconstructed. A large, constant background (red) overlaying the signal (green) will result in a limited phase range of the measured signal (blue). Under these circumstances, signals of equal magnitude and opposite phase may appear as measured signals of different amplitude and similar phase.

of the superimposed beams behind the combining beam splitter. With motorized rotation stages for the two Glan-Taylor prisms we can systematically scan the polarizations to find the optimal configuration.

Interferometric amplification also allows extracting both the amplitude and relative phase between signal and reference beam. The intensity measured by the lock-in analyzer depends on the relative phase of both beams, as shown in equation (3.1). Over the years, in apertureless nearfield microscopy a number of schemes have been developed, in close analogy to information encoding techniques in signal processing electronics [103]: In the *homodyne scheme*, amplitude and phase are reconstructed by measuring twice with two different relative phases between both beams [84]. The relative phase can be shifted for example by changing the optical path length of the reference beam. The *phase-shifting* scheme is similar, but employs more than two different relative phases [106]. Another possibility is to use a (double) *heterodyne* scheme, where one (both) of the beams is frequency shifted and thus the phase difference continuously increases with time [84, 101]. In a *pseudo-heterodyne* scheme, a periodic modulation of the relative phase generates sidebands that are analyzed [107].

In our aSNOM we employ a homodyne scheme. The phase difference between both measurements is controlled by a home-built piezo-driven (PI Ceramic, P-887.50) mirror assembly. The phase difference of the reference path between the two measurements S_1 and S_2 is set to $+90^\circ$. Both measurements are projections of the complex valued total signal S on two lines with—in our case—an angle difference of

90° in the complex plane (see Fig. 3.2). Total amplitude and optical phase ψ are:

$$S = \sqrt{S_1^2 + S_2^2} \quad (3.3)$$

$$\tan \psi = \frac{S_2}{S_1} \quad (3.4)$$

To be able to address the full range of $\psi \in [0, 360^\circ[$ and to obtain a proper optical phase that coincides with numerical calculations [44], it is crucial to attribute a sign to the two measured amplitudes $S_{1,2}$. One way is to assign a negative amplitude whenever the lock-in detector phase (available range $-180^\circ \dots +180^\circ$) is below zero and positive otherwise. From the two signs of $S_{1,2}$ the value of ψ is thus fixed uniquely.

In the cross-polarization scheme, exciting and detected beams are orthogonally polarized [31, 92]. Using s-polarized light for illumination, the tip is hardly excited at all [108]. The sample, however, may exhibit structures with strong plasmonic resonances excitable by the s-polarized excitation. The tip efficiently picks up the local vertical field components of these resonances. Tip and sample scatter light into the farfield with a p-polarized component. We place a second polarizer in front of the detector, set to p-polarization.

Regarding the interferometric signal amplification the different types of interferometers demand different implementations. In a Michelson type interferometer the light is s-polarized in the illumination path. Passing a $\lambda/4$ -plate in the reference arm twice, the polarization turns by 90° . The now p-polarized reference beam is mixed with the signal from the tip, amplifying the p-polarized component of the scattered light [109].

We view a Mach-Zehnder interferometer as preferable since it allows an independent manipulation of the two partial beams, offering direct, full control of the polarization states in both paths. We split reference and signal carrying beam. While the reference beam is unpolarized, a Glan-Taylor polarizer in the sample illumination path is set to s-polarization. The scattered light is interfered with the reference beam by a second beam splitter, and a second polarizer projects on the p-component of both beams. The rotation stages of the Glan-Taylor polarizers are equipped with stepper motors (Controller: Physik Instrumente, PI 511), which allow for systematic scans of both polarizers to find the optimal configuration.

We use silicon non-contact AFM tips (Nanosensors, AdvancedTEC NC) [97, 47]. To our experience, this kind of probe provides sufficient scattering cross-section with little or no parasitic coupling. For plasmonic resonant gold structures in the visible to near infrared region, we do not observe perturbations of the sample compared to FDTD calculations not including the silicon tip [44]. For more delicate systems, more weakly interacting tips could be necessary.

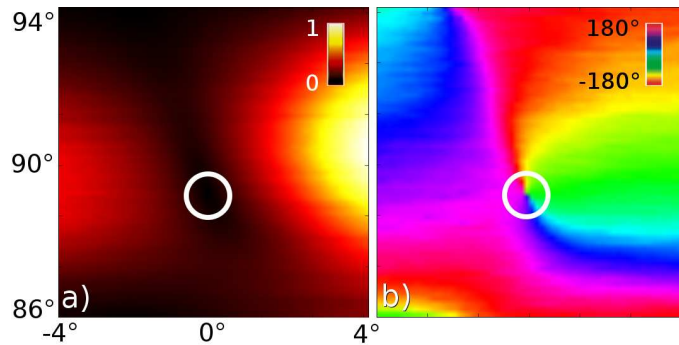


Figure 3.3.: Systematic search for the optimal polarizer angles. Polarizer (horizontal axis) and analyzer (vertical axis) are scanned around the nominal cross-polarization position $0^\circ/90^\circ$. The images show (a) optical amplitude in arbitrary units and (b) optical phase. The position of the phase singularity is marked in both images.

3.2. Alignment and Verification

For alignment of the setup, we first set the sample illuminating beam to s-polarization with respect to the sample. In this first step the analyzer is not perpendicular to the polarizer, but about 20° out of p-polarization to ensure that both polarizations pass. We block the reference beam and retract the sample from the tip. After a coarse alignment of the tip in the focus we align the single mode fiber of the detector to place the detection focus volume to the position with highest backscattering intensity. The lock-in analyzer deconvolutes the signal at the first harmonic of the cantilever oscillation frequency. To find the center of the focus, we scan the tip through the focus at constant height using the three-dimensional piezo scanner of the AFM head. As the size of the tip apex is much smaller than the (diffraction limited) focus size, we consider the tip as point scatterer, imaging the focus shape [110]. By comparing scans at different tip heights (continuously realigning the detector fiber) we determine the height of minimal focal diameter and maximum intensity.

Having situated the tip at the center of the three-dimensional focal volume, one usually finds a finite backscattering background in the cross-polarized detection channel. Without further optimization, this is essentially an unavoidable consequence of a variety of experimental imperfections: AFM tips are not suitably shaped and aligned, the illumination is not a properly Gaussian beam, etc. The next alignment step is therefore to examine whether optimal cross-polarization can be established by optimizing the polarizer settings. In our experience, it is usually possible to find polarizer settings, which show *zero* backscattering intensity.

The optimal configuration is indicated by the occurrence of a phase singularity in the backscattered radiation when scanning the polarizers. The theoretical back-

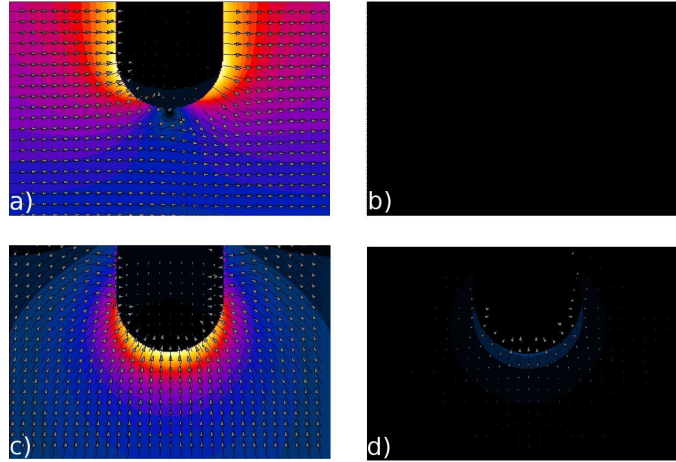


Figure 3.4.: Simulated nearfields at one end of a gold nanorod, excited by linearly polarized light of 900 nm wavelength. The apex radius is 30 nm, field of view is 180 nm x 120 nm. a),b) real and imaginary part of the electric field for horizontally polarized excitation (s-polarized). c),d) real and imaginary part of the electric field for vertically polarized excitation (p-polarized). The simulation is performed using an multiple multipole (MMP) method. [78, 111]

ground of this singularity is explained below. To locate it experimentally, we use interferometry to gain phase sensitivity, recording the homodyne amplitude and phase. The systematic search then involves raster-scanning the two linear polarizers each by a few degrees around the nominal alignment. Typical two-dimensional data of a polarization scan is displayed in Fig. 3.3.

The position $0^\circ/90^\circ$ for polarizer and analyzer marks the position of nominal cross polarization. The actual minimum in the amplitude scan is at a slightly different position. An indication for the optimal setting is found in the corresponding phase image. Encircling the lowest intensity pixel, a phase accumulation of 2π becomes evident – the classic signature of a topologically non-trivial feature. The implied phase singularity associated with this minimum is thus a mathematical *point* in parameter space. Barring the usual experimental caveats, such as accuracy in parameter setting, measurement noise, or stability, the background signal can be set not only below the detector noise, but to actual zero level. In our setup, this minimum is typically found at polarizer positions within $\pm 5^\circ$ off the nominal position.

After aligning the setup we approach the sample from below until it is in proximity of the tip. Keeping the tip fixed in space, we raster scan the sample with a piezo stage (Physik Instrumente P-517.3CD). From the AFM feedback loop and optical signal we obtain images of the topography as well as optical amplitude and phase.

3.3. The Nature of the Phase Singularity

The occurrence of a phase singularity in the polarizer scans described above is a natural consequence of two orthogonal tip modes being excited. As they are excited and recorded in the farfield with two orthogonally polarized modes (s- and p-polarization), it is convenient to employ the Jones formalism to describe the detected signal. Scattering from the tip apex region – when properly centered in a Gaussian focus – is well approximated by a polarization ellipsoid [108, 83, 45]. It responds to excitation by s- and p-polarized light with two orthogonal modes (see also Fig. 3.4).

The symmetry of this idealized system causes radiation emitted by the excited tip to be again linearly polarized in the same modes as the excitation radiation. Hence, off-diagonal elements of the Jones matrix describing the tip backscattering are zero,

$$\mathbf{T} = \begin{pmatrix} \alpha_s & 0 \\ 0 & \alpha_p \end{pmatrix} \quad (3.5)$$

where $\alpha_{s,p}$ are complex-valued coefficients describing the backscattering strength of the tip due to the two modes. The linear polarizers used in the excitation and detection path are described by

$$\mathbf{P}(\theta) = \begin{pmatrix} \cos(\theta) \cos(\theta) & \cos(\theta) \sin(\theta) \\ \sin(\theta) \cos(\theta) & \sin(\theta) \sin(\theta) \end{pmatrix} \quad (3.6)$$

The detected signal after passage through the whole system, with the two polarizers at angles $\theta_{in,out}$, reads

$$\mathbf{E}_{out} = \mathbf{P}(\theta_{out}) \cdot \mathbf{T} \cdot \mathbf{P}(\theta_{in}) \cdot \mathbf{E}_{in} \quad (3.7)$$

Typical examples for signal strengths simulated with Eq. (3.7) for different polarizer angles and polarizabilities are illustrated in Fig. 3.5. Generally, a phase singularity is observed located at the nominal cross-polarization position. The amplitude images exhibit an elliptical shape, whose orientation and eccentricity depends on both the relative magnitudes and phases of α_s and α_p . Only for the degenerate case of a relative phase difference between the two polarizabilities of zero or 180° does the phase singularity become a line of zero amplitude.

In passing we note the possibility to extract from such scans – with corresponding analysis, based on Eq. (3.7) – the complex valued ratio α_p / α_s . That is, the relative dipolar polarizabilities of an unknown tip can be characterized. In this sense, our polarizer scans are related to particle tip characterizations employed in previous studies. [112, 113]

In a real setup, the perfect symmetry stipulated above is not realized. However, the presence of a phase singularity is a *topological property* of the system. As such it

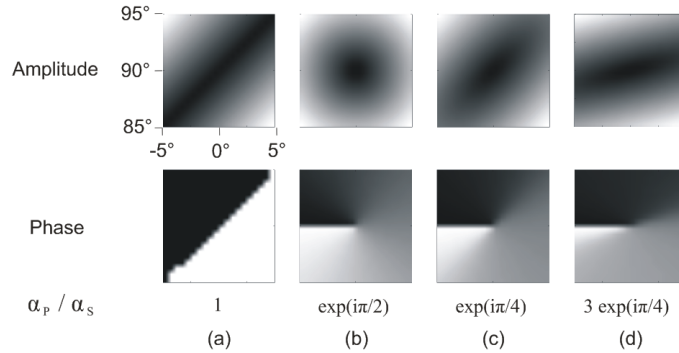


Figure 3.5.: Simulations of cross-polarization scans using equation 3.7. (a) When both modes of the tip $\alpha_{s,p}$ are degenerate, no singularity in phase is observed. Arbitrary phase differences other than $0, \pi$ lead to the occurrence of phase singularities in the cross-polarization position. The special case of $\alpha_p = i\alpha_s$, as displayed in (b), yields a perfectly round minimum. Different retardations (c) and strengths (d) of both modes lead to an elongated elliptical minimum.

is quite robust against small, continuous deviations. For example, small rotations or displacement of the tip in space – being adiabatic evolutions of the system – do not abruptly destroy the phase singularity. Slight adjustments to the polarizer angles allow it to be recovered.

Similar arguments hold for adiabatic deformations of the tip. These introduce small, non-dipolar polarizabilities, whose backscattering is superimposed on the dipolar response. Still, for not too large deformations, it is possible to find cross polarization. By slightly realigning the polarizers the coherent superposition of dipolar and (small) non-dipolar scattering is such that an exact linearly polarized state is formed at the analyzer.

It takes more drastic deviations from the presumed perfectly conical tip shape to develop sufficiently strong non-dipolar polarizabilities that always lead to some non-linearly polarized backscattered signal, regardless of input polarizer alignment. In this case, no phase singularity is observed in the polarizer scans, only a finite minimum amplitude. On the one hand, this forces us to reject some of the commercial AFM tips we employ (less than forty percent). On the other hand, the systematic cross-polarization scan provides a welcome rational method for screening the suitability of AFM tips for aSNOM.

Chapter 4.

Optical Antenna Phase Arrays

At radio frequencies, antennas are used to convert electric currents to electromagnetic radiation. With increasing bandwidth, that is increasing frequencies, frequencies reach the optical spectrum of electromagnetic waves. The optical carrier frequencies of several hundred THz allow for ultrafast data interconnects. Optical antennas are couplers from far-field radiation to confined modes [19, 20, 21] and other locally excitable modes like waveguided signals. Antennas can be seen as impedance matching devices between farfield optical modes to subwavelength modes in their vicinity. In sending mode, optical antennas can be used, for example, to enhance the emission of quantum dots [114, 115]. Efficient single photon emitters like quantum dots are needed in optical quantum computing and quantum cryptography [116]. In receiving mode, they can also be implemented to confine light to subwavelength regions [117]. Optical antennas behave similar to their radio counterparts [30, 118, 119]. In the radio regime, antennas behave as perfect conductors. At optical frequencies in the near-infrared, however, the conductance of typical metals is finite, and antennas typically suffer from ohmic losses. Not only does this pose challenges for the production of high quality plasmonic resonators. It also leads to plasmon wavelengths smaller than that of light. In this chapter, we discuss these differences between radio frequency and optical antennas as well as which concepts from radio antennas can be carried over to optical frequencies. [120, 121, 122]

4.1. Feedgap Antennas

As a first example, we discuss linear feed-gap antennas consisting of two gold wires separated by a small gap. Both antennas give rise to a very strong field in the gap, which has been studied for sensor applications and optical trapping. [123] The cross-polarized aSNOM technique is used to obtain faithful nearfield information from these rather complex plasmonic structures. The antennas are patterned by e-beam lithography and evaporation of gold on a silicon dioxide substrate. Fabrication and size parameters are systematically varied to tune the resonance frequencies and identify optimal structures with the desired optical response.

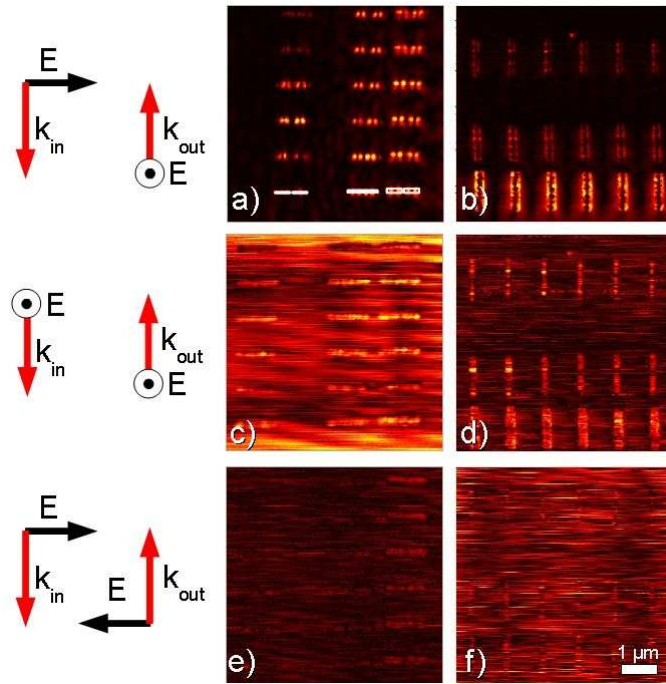


Figure 4.1.: Near-field images of feed-gap antennas under different illumination conditions at $\lambda = 911 \text{ nm}$. The antennas are made of gold on a silicon dioxide substrate. a), b): Cross-polarization scheme. In a), the topography of the lowest row is marked in white. From the left to the right, the wire thickness varies. From top to bottom, the gap size changes. In b), the sample is rotated in the image plane by 90° . Non-resonant transversal modes are excited. c), d): Both illumination and detection polarizers are aligned to p-polarization. e), f): Both polarizers are aligned to s-polarization.

Fig. 4.1a shows the images measured in cross-polarization. With the electric field of the incident beam in the direction of the wire, the antennas are strongly excited. In this configuration, lobes of the electric field strength are observed on the resonant wires. The plasmonic eigenmodes are mostly unperturbed [44]. Background signal in regions without metallic structures is low. The strong field in the gap is not observed, though. This field has mainly in-plane components, and the cross-polarization technique is sensitive to vertical field components (see chapter 2). When we place the antennas perpendicular to the incident electric field (Fig. 4.1b), we excite transverse modes of the wire. These do not depend on the wire length, only on its width. The structures are not resonant for this mode.

Using p-polarization for incident as well as detected light, both tip and sample are directly excited, couple to each other, and scatter back (see Fig. 4.1c,d). Much of the contrast observed here stems from variations in the backscattering cross-section of the coupled tip-sample system, which in turn largely depends on sample material. By comparing with simulations or a model [124], one can gain information about the dielectric constant of the sample or even its dielectric tensor [125].

When aligning both illumination and detection path to s-polarization, we obtain very low signal intensities in the near-infrared (see Fig. 4.1e,f). Evidently the tip cannot be efficiently excited by the incident beam, nor can it radiate efficiently with this polarization. In our setup, a strong background overwhelms the signal on the detector. In the mid-IR, for cases of particularly strong nearfields at a sample, such a configuration has been shown to allow mapping of in-plane components [124].

4.2. Yagi-Uda Antennas

While strong field enhancement like in feedgap antennas is required for sensitive detectors, in data transmission different antenna functionality is of interest. Here, the focus lies on efficient emission from a sending device or excitation of a receiver. One way to achieve this is using directional antennas: Radiating only in a small solid angle, the intensity in emission direction increases compared to a dipolar antenna emitting the same power. Also in receiving mode, the excitation of the antenna is enhanced compared to a dipolar antenna, increasing sensitivity. Directional antennas are widely used in radio frequency engineering. They offer the possibility to send signals selectively in a certain directions or to receive incoming signals from a distinct direction. A prominent example for directional antennas is the antenna concept of Yagi and Uda [126]. Many antennas found on rooftops for receiving radio and television signals are based on this concept. In this section, we present Yagi-Uda antennas at optical frequencies. Recently, functional optical Yagi-Uda antennas were presented in emission mode [127, 23, 128, 129]. Here, we focus on Yagi-Uda antennas in receiving mode. With our aSNOM, we directly reveal the optical nearfields and proof coupling of the individual antenna elements.

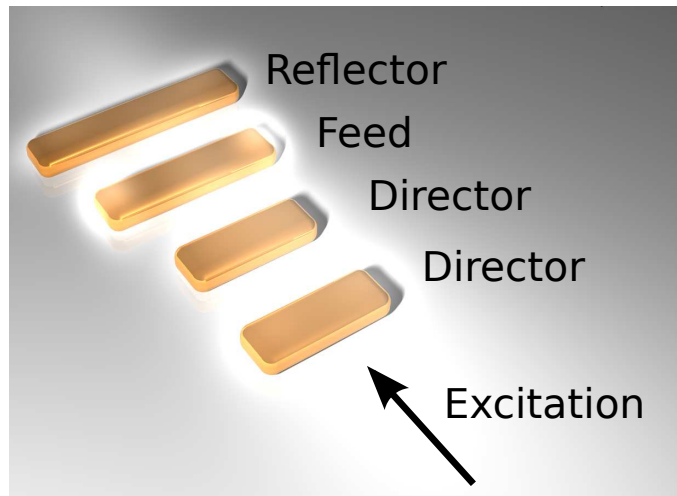


Figure 4.2.: Scheme of a Yagi-Uda antenna. A Yagi-Uda antenna consists of a feed element, a reflector and several directors. All wire elements couple electromagnetically to enhance feed excitation upon excitation from the forward direction.

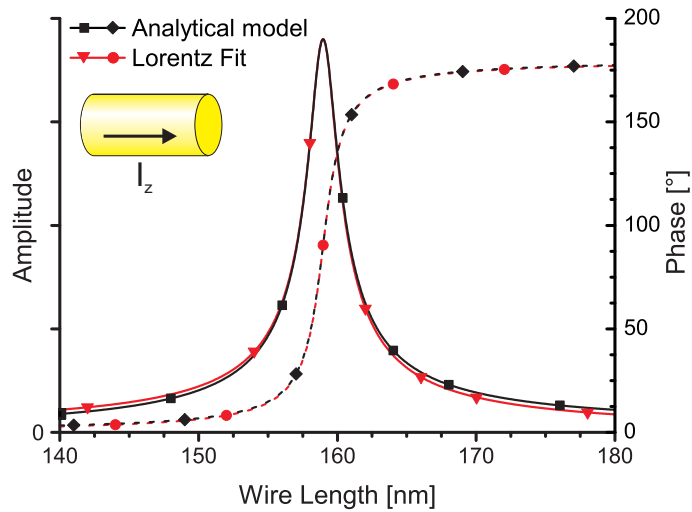


Figure 4.3.: Current in a thin wire antenna under plane wave illumination. Amplitude (solid line) and phase (dotted) are shown using an analytic model.[30] The antenna excitation is well approximated by a Lorentz curve (red). Short antennas couple capacitively (0° phase lag), large antennas inductively (180° phase lag) to the incident field.

Yagi-Uda antennas consist of several wire antennas: directors, the feed element and the reflector (see Fig. 4.2). The feed element is a resonant dipolar antenna. For radio antennas, this element is typically electrically connected. The director elements are smaller than the feed element, capacitively coupled to the incident radiation. They are arranged in emission direction with respect to the the feed element. The reflector element is placed opposite of the director. It is longer than the feed and couples inductively to the incident field (see Fig. 4.3). Director and reflector position are chosen so that they constructively couple to the feed element, enhancing its excitation upon illumination from the front. The enhancement strongly depends on the direction of incident light.

The antenna design of the structures investigated here is based on previous work [128], optimized by finite integration technique (FIT) simulations.[93] A series of antennas with varying resonance around the laser wavelength of 1064 nm is patterned using electron beam lithography with PMMA resist, gold evaporation and a lift-off process. The feed antenna length is centered around the nominal length of 198 nm with a difference of 10 nm between consecutive antennas. The lengths of director and reflector elements are scaled, accordingly. Width and height of all antennas are 80 nm and 30 nm, respectively.

In our aSNOM, the Yagi-Uda antennas are characterized in receiving mode: The structures are illuminated by s-polarized light and the z-component of the nearfield on the antenna is recorded. In Fig. 4.4, nearfield images of different sized Yagi-Uda antennas are shown. For antennas smaller than the nominal resonance length, only the longest element, the reflector, lights up. All other elements are far off-resonant, barely excitable by the incident radiation. In contrast, on a resonant Yagi-Uda antenna all elements are excited. The feed element shows strongest excitation. From the optical phase we conclude that the directors are capacitively coupled to the feed element with a phase lag of -64° compared to the feed element. The reflector is inductively coupled, with a corresponding phase lag of 64° . A similar phaseshift behavior is already expected for single antennas [30] (see also Fig. 4.3). For antennas longer than the resonant length antennas, the zone of excitation shifts from the feed element to the directors.

To check the directionality of the antenna, we compare the antenna nearfield under forward and backward illumination (see Fig. 4.5). We observe the feed element lights up much brighter than the other elements under forward illumination. Upon backward illumination, this is not the case. The excitation is spread over the whole antenna. The antennas couple constructively only upon forward illumination, exhibiting antenna directionality in the nearfield response. Despite the differences between the material response at radio frequencies and in the optical regime, the concept of Yagi and Uda is still applicable for directional antennas at optical frequencies. [130]

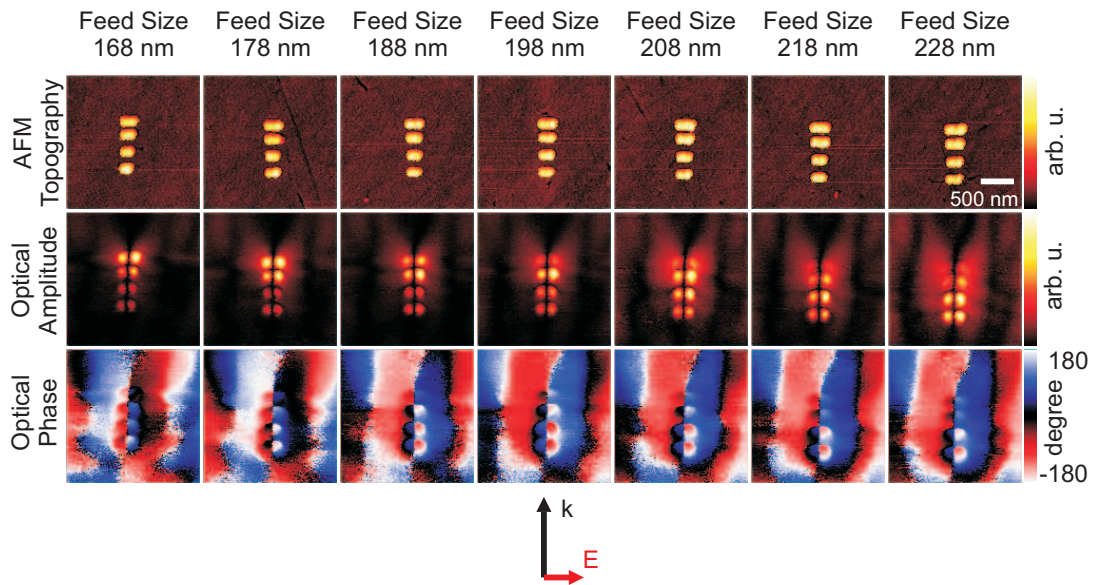


Figure 4.4.: Near-field optical images of Yagi-Uda Antennas. The antennas are fabricated of gold on a silicon dioxide substrate. They are illuminated in forward direction (from the lower side of the images) with $\lambda = 1064$ nm radiation. From left to right, the antenna size is tuned. The upper row shows the AFM topography of the antennas. The center row shows the optical amplitude and the lower row the optical phase simultaneously recorded. With increasing antenna size, the region of strongest excitation shifts from the reflector over the feed element to the directors.

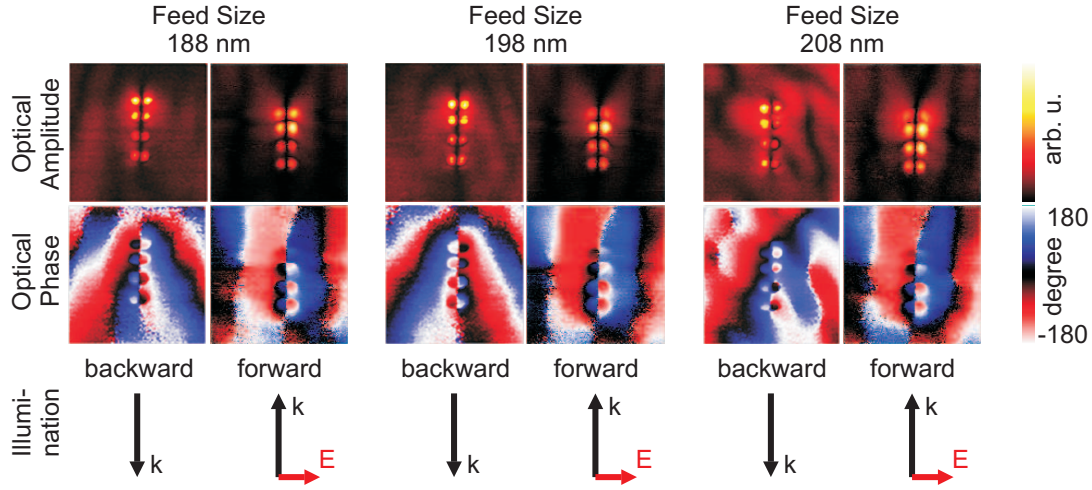


Figure 4.5.: Comparison of Yagi-Antennas under forward and backward illumination. Images under forward illumination are the same as in Fig. 4.4. Upon forward illumination, the field on the Yagi-Uda antennas is concentrated on the feed element. For the very same antennas under backward illumination, the field is distributed over the whole antenna area and no clear field enhancement can be observed. Colorscales of each image are individually set.

4.3. Unidirectional Plasmon Launchers

Plasmonic structures are usually difficult to excite directly by photonic fields due to mismatched wavevectors of photons and plasmons (see Fig. 1.1). In the language of electrical engineering, plasmonic and photonic modes suffer from considerable impedance mismatch. [131, 114, 132, 31, 133, 121] Efficient matching is achieved by optimizing the complete structure geometry with a specific figure of merit, employing full-field simulations.[134, 135, 121, 136] Alternatively, the illumination of a given structure can be optimized by coherent control methods in time and space.[137, 138, 139, 140] Here we employ an approach that borrows parts from all of the above concepts. To improve impedance matching, “coupling points”, that is, point-like resonant elements, excite the target structure via near-field coupling. The coupling points act as antennas, converting far-field photonic modes to plasmonic modes.[141, 19] Multiple couplers, which are designed and placed individually, thus allow for flexible construction rules and the excitation of nearly any desired eigenmodes (see Fig. 4.6).

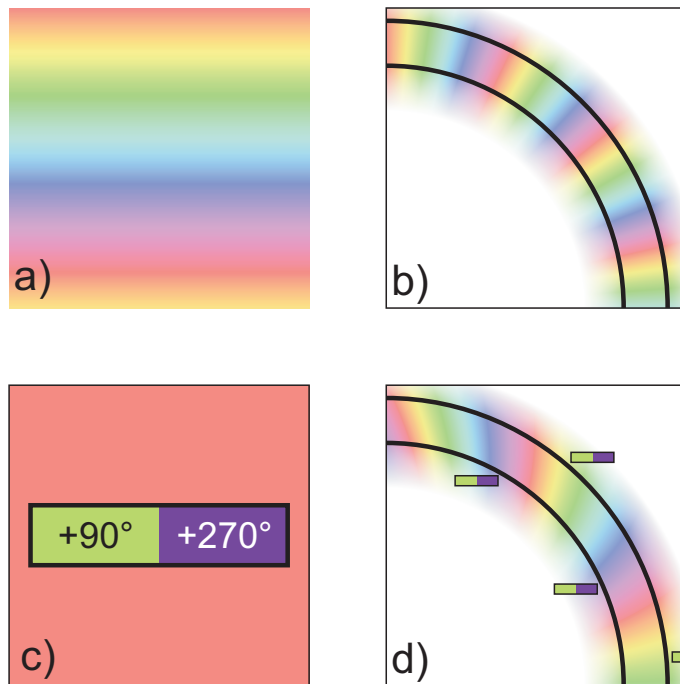


Figure 4.6.: Scheme of the phase engineering principle. (a) Given a phase pattern of the incident mode, e.g. a plane wave, to excite a desired mode, exemplified by a propagating wave on a bent waveguide (b). The desired mode couples only weakly to the incident light field. Efficient excitation of the structure can be utilized by using coupling points (c), that is, point-like elements that couple strongly to the incident radiation and can excite the structure by near-field coupling. The coupling points introduce a certain phase lag compared to the incident radiation. The optimal coupler positions can be found by subtracting the desired phase from the incident phase pattern. Couplers are placed where this difference matches the phase lag of the couplers.

Phase matching is the primary guiding principle for placing an individual coupling point. The response phase lag of the coupler $\Delta\phi_c$ has to compensate the difference between the phase ϕ^{inc} of the incident light field and the phase ϕ_s of the desired mode. The optimal coupler position is found where the phases match:

$$\phi^{inc} + \Delta\phi_c = \phi_s \quad (4.1)$$

For a given excitation wavelength, scaling length and width of a coupler shifts its resonance in or out of resonance. Both the plasmonic excitation amplitude and phase of the coupler can be optimized by these two parameters, as illustrated for thin antennas in Fig. 4.3.

By combining several coupling points, generally a configuration can be found where all couplers constructively excite the desired mode and suppress undesired ones. This is achieved by varying the coupling strength via the gap size, changing the coupler position, or by tuning the intrinsic phase delay of the coupler. A practical limitation to the total number of couplers is imposed by geometric consideration of the limited surface area. Also, too closely spaced couplers are generally detrimental as this leads to hybridization of their resonances, affecting the matching rule Eq. (4.1). However, as we will show below, hybridized aggregated subunits may be employed beneficially as a different kind of component coupling point. For our experiments we use gold structures patterned by electron beam lithography on a silicon substrate. The measurements are carried out using an apertureless scanning near-field optical microscope (aSNOM) in cross-polarization mode, measuring the z-component of the sample nearfield nearly without any perturbation by the probe.[78, 44, 97, 142] The proof-of-concept structures we fabricated are designed as efficient couplers of s-polarized light to a plasmonic waveguide. This is one of the basic functions for passive plasmonic elements. Couplers can be designed to selectively excite modes traveling from the coupler in the direction of a device. Directional coupling can be utilized for example in end-fire configuration by illuminating the end of a waveguide[143] or by using the direction-selective properties of asymmetric grating coupler configurations.[144] This spatially dispersive behavior also implies the advantage of such devices to be used as multiplexers. However, efficient gratings are typically several wavelengths long, and for high integration densities much smaller sizes are desirable. Here we demonstrate that subwavelength footprint couplers/multiplexers can be achieved with the concept of coupling points constructed from plasmonic antennas.

We consider long, thin gold wires as plasmonic waveguides (see Fig. 4.7). The waveguides are 3 μm long and of 40 nm width and 30 nm height. The wires themselves are only weakly excited by the incident radiation (see Fig. 4.8). In order to facilitate excitation of waveguided modes by plane wave excitation we place dipolar wire antennas as couplers next to the waveguide. The coupling elements are resonant dipolar antennas of 165 nm length and same width and height as the waveguide

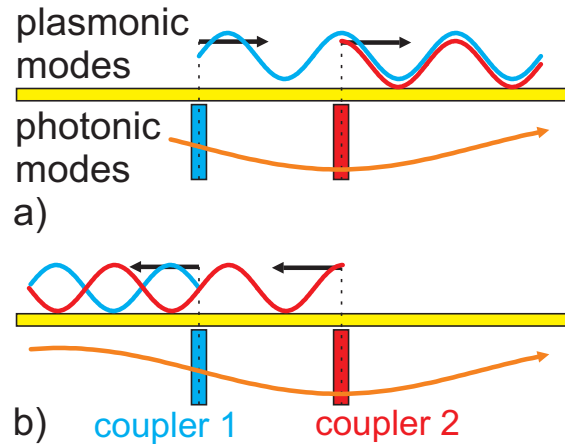


Figure 4.7.: Scheme of the unidirectional couplers. Dipolar antennas act as couplers of photonic far-field modes (orange) to a waveguide (yellow). Each coupler launches plasmons on the waveguide traveling in both forward (a) and backward direction (b). Interference between the plasmons launched by both antennas introduces directionality.

(compare to Fig. 4.3). The antennas are separated from the waveguide by a 15 nm wide gap. Upon successful launching, plasmons travel in the waveguide in both directions away from the coupling points. Similar to an optical grating, placement of several coupling points can result in directional plasmon launching.[145] The structures presented here are one of the smallest realizations of a grating coupler. Similar to the Yagi-Uda feed and director element previously discussed, also in the case of unidirectional launchers two antennas are placed in phase and position to constructively excite a desired mode in forward direction. In analogy to the feed-reflector behavior, interference is destructive in the backward direction.

Three different realizations of a waveguide coupler constructed with this principle are displayed in Fig. 4.8. The coupler in Fig. 4.8a clearly shows directional plasmon coupling to the waveguide. Placing coupling points on either side of the waveguide affords an additional 180° phase shift, reducing coupler size in the horizontal direction. The position of the couplers can be tuned to match plasmons travelling in the forward or backward direction compared to the incident light (see Fig. 4.8b-c). The antennas are placed employing the phase coupling principle: For an angle of incident light of 70° from the surface normal and radiation of 1064 nm wavelength we find the wavevector for retardation of incident light in the surface plane to be $k_{\parallel} = 2\pi/1132$ nm. The plasmon wavelength on 40 nm wide and 30 nm high wires around 410 nm is derived from previous work [31]. Using the phase matching principle described above, we optimize the coupler positions for destructive coupling in the forward or backward direction. This maximizes the forward/backward ratio. The vertical distances between both antennas are 160 nm (Fig. 4.8b), 150 nm (Fig. 4.8c),

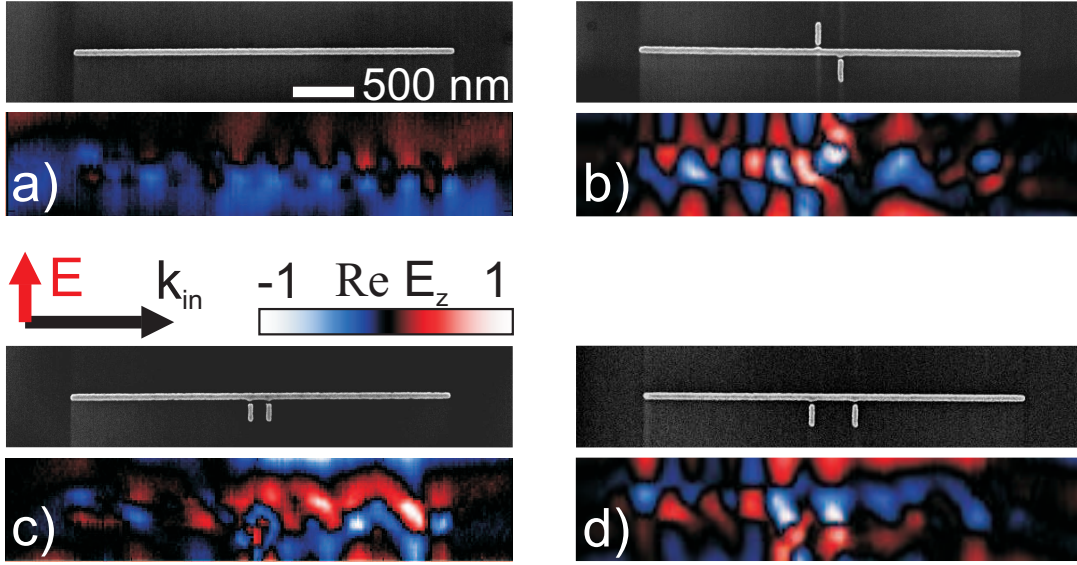


Figure 4.8.: Unidirectional plasmon launchers. The top image of each subfigure is a SEM micrograph of gold structures on silicon dioxide. The lower image shows the measured optical nearfields. The structures are illuminated with 1064 nm radiation 70° from the surface normal.

and 320 nm (Fig. 4.8d) for the respective antenna layouts.

The intrinsic phase delay of couplers can also be used to directionally excite plasmons on the wire (see Fig. 4.3), offering additional antenna positions. A structure with couplers consisting of two antennas of different size is shown in Fig. 4.9. Several coupled antennas constructively exciting a structure are reminiscent to Yagi-Uda antennas.[23, 146, 93, 24] For the composite coupler, the antennas on both sides are shifted by 160 nm with respect to each other, like in Fig. 4.8b. The sizes of the coupler components are optimized to increase coupling efficiency.

The coupling efficiency is indeed significantly higher than that of single wire couplers. We find that the phase difference between both antennas is 20° rather than 90° one would expect for uncoupled antennas. Evidently, the antennas interact with each other and a hybridized mode is excited by the incident radiation. The resulting hybrid antenna can be seen as a single, composite coupling element, which has a larger surface area exposed to the wire waveguide, and a correspondingly increased coupling strength. This structure allows for more efficient coupling, keeping the coupler footprint size on the order of the scale of single antenna coupling points.

Hybridization between sub-elements opens new opportunities for flexible construction of composite couplers: For example, Fano resonances can lead to spectrally very sharp in- and outcoupling of certain frequencies, internal phase optimization of a coupler can lead to improved directionality, or as in our case, the active surface area of the coupler is enhanced. In summary, we have shown a general approach

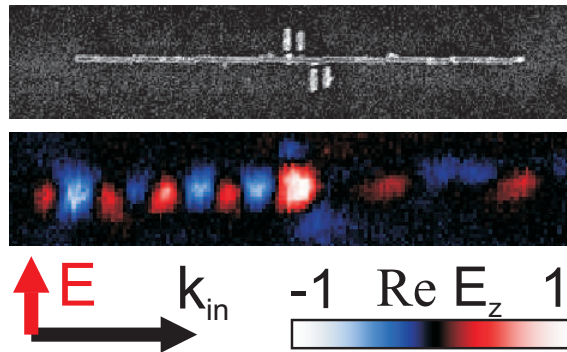


Figure 4.9.: Unidirectional plasmon launcher with composite couplers, consisting of two hybridized antennas each. Strong directionality is achieved, while keeping the coupler footprint almost constant compared to the coupler shown in Fig. 4.8b. No background subtraction has been applied to the measurement data.

for elastic plasmon excitation processes. Antennas act as coupling points converting photonic modes to localized or propagating plasmonic modes. Selective excitation of a desired plasmonic mode is achieved by tuning position and phase retardation of the couplers. As a demonstration of the concept we show launchers of unidirectional waveguided modes. The approach allows for extremely compact assemblies, where the total area of the coupler assembly is of deep subwavelength footprint. As an outlook, we draw attention to the recent demonstration of self-assembled growth of plasmonic logic gates.[18] The concepts presented in this Letter are well suited for performing improved addressing and read-out tasks with such circuitry. In combination with active elements, such as high speed modulators, they might also prove useful in amplifier plasmonics.[147]

Chapter 5.

Amorphous Plasmonic Systems

Metamaterials are artificial optical systems of subwavelength structures. They achieve optical functionalities not known from natural materials, like optical magnetism [148], ultrathin polarization manipulators [149, 150], and negative refractive index [151]. Often, their optical response can be described by effective permeabilities and permittivities, describing the average interaction of a light wave with the individual structures. Many metamaterials consist of periodic plasmonic structures, fabricated by sequential top-down techniques like electron beam lithography.

This chapter deals with aperiodic structures, consisting of small, coupled scattering objects. The optical response of plasmonic particles is determined by their material composition, size [25, 26, 12] and shape [27, 28, 29]. For multiple particles, also the inter-particle interaction plays a role. For dimers, consisting of two interacting particles, it was shown that excitation can be controlled [152, 153] by varying orientation [154, 155, 156] and distance [12, 157, 158, 159, 160, 161, 162, 163] between both particles. In two-dimensional amorphous metamaterials [164, 165], that is, randomly oriented plasmonic particles on a surface, excitation is also largely determined by interparticle interaction. As was previously published, the spectra of partially integrated differential cross sections of such materials strongly depend on illumination and collection angles.[166] For closely spaced plasmonic nanoparticles, studies of interaction between individual particles are only possible in the nearfield.

5.1. Distance Dependence of Interaction Strength

The samples investigated consist of gold nanodiscs on silicon dioxide substrate. They are produced using hole-mask colloidal lithography (HCL), allowing for large scale fabrication at low cost. [167] On the sample we find short-range ordered nanoplasmonic arrays of nanodiscs. The diameter and height of the discs are 190 nm and 25 nm, respectively. The dipolar resonance of the discs is around 800 nm. Three samples of different area disc density, that is, different average neighbor distance, are analyzed.

In our aSNOM, we illuminate a diffraction limited spot on the sample, containing multiple discs. The local excitation of the discs depends not only on the polarization

of the incident beam, but also on the interaction with neighboring discs. Similar to substrates for surface enhanced raman spectroscopy (SERS), the statistical arrangement of discs can lead to the formation of hotspots [168]. The measurements are performed on an area of $10\ \mu\text{m}$ by $10\ \mu\text{m}$ with a spatial resolution of 20 nm. The resolution is limited by acquisition time, which is around 6 hours for 500×500 data points. While recording, the setup has to be stable at least over a whole image.

In the nearfield images (see Fig. 5.1), a dipolar pattern on each disc is clearly visible. Most disc dipoles are oriented along the direction of incident electric field. However, on a closer look we see variations in the dipole angle. A statistical analysis of disc dipole orientations in the nearfield images [169] shows that for discs with a nearest neighbor distance of more than 2.5 disc diameters (center to center), the dipole orientation is more or less equal to the direction of incident radiation. For more closely packed arrangements of discs, we see deviations in the dipole orientation. The fluctuation of dipole moment around the incident polarization increases with disc density (see Fig. 5.2).

5.2. Simulation of the Systems

We perform FDTD simulations of the samples experimentally investigated. All parameters of the simulation are chosen to be identical with the experimental conditions as good as possible. To perform simulations on exactly the same disc arrangement, we extract the sample topography from the aSNOM measurement AFM channel. For simulation we assume s-polarized plane wave excitation and calculate the z-component of the nearfield 24 nm above the sample in absence of any probe tip. In the simulation, we see a similar trend as in experiment: the fluctuation of dipole angle increases with particle density. However, we find a quantitative discrepancy that in simulation the dipole angle fluctuation is much wider than in experiment.

5.3. Illumination Conditions

As both experiment and simulation deliver faithful images of the unperturbed sample nearfield, we search the origin of the discrepancy in different experimental conditions than in simulation. The only parameter left is that in simulation, we use plane wave excitation, whereas in experiment the incident light is focused on a $1.7\ \mu\text{m}$ diameter spot. The focused illumination results in different excitation conditions of particles far from the probe tip compared to plane wave illumination, leading to different interaction contributions from these particles. At inter-particle distances as measured on the sample, particle interaction is dominated by dipole-dipole coupling.[170] The field incident on each particle by scattering from other particles can be calculated

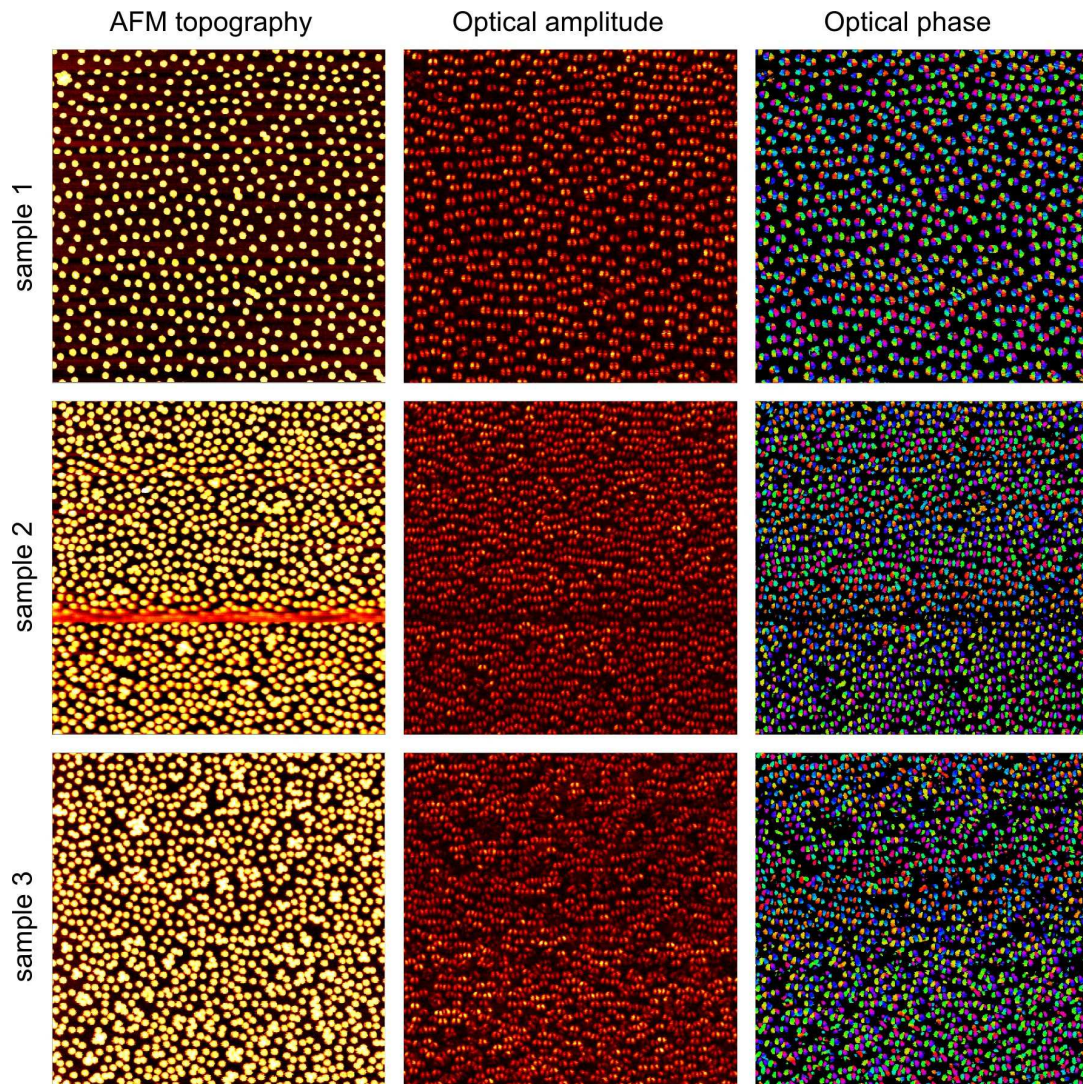


Figure 5.1.: Nearfield images on large area arrays of amorphously distributed gold discs. Three samples of different disc density are investigated. Each image is 10 times 10 μm . The sample is illuminated with a focal spot of 1.7 μm diameter and a wavelength of 911 nm.

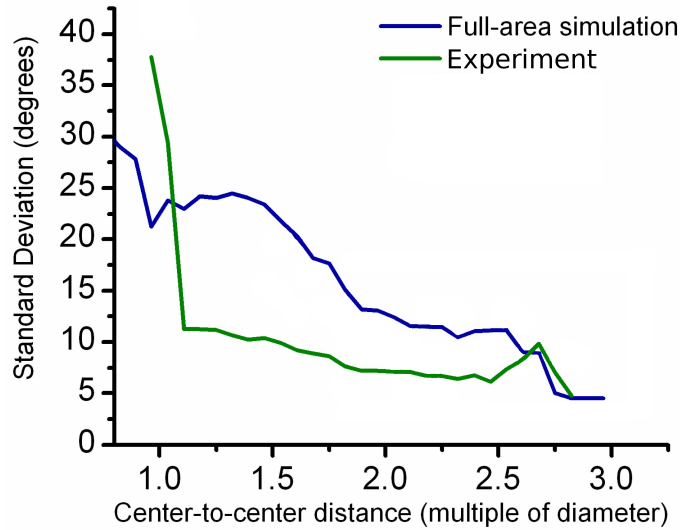


Figure 5.2.: Statistical analysis of dipole orientations in amorphously distributed gold disc samples. The fluctuation of dipole angle increases with decreasing nearest neighbor distance of each disc. A quantitative discrepancy shows up between simulation assuming plane wave excitation and experiment, carried out with focused radiation. [169]

using the Green formalism

$$\vec{E}^{sca}(\vec{r}) = \omega^2 \mu_0 \int_V d^3 r' \hat{G}(\vec{r}, \vec{r}') \Delta \hat{\epsilon}(\vec{r}') \vec{E}^{in}(\vec{r}') \quad (5.1)$$

The longest reaching term in the (vacuum) Green propagator decays with distance as $1/r$. The number of particles at this distance can be estimated considering a thin ring of radius r (see Fig. 5.3). The area of a ring of infinitesimal thickness dr is $2\pi r dr$ and thus the average number of particles within this ring increases with r . The larger number of particles at far distances balances out the weaker interaction with each individual particle: The average contribution of each ring of radius r is equal, independent of the distance (as long as all particles are equally illuminated by the incident radiation $\vec{E}^{in}(\vec{r}')$). We may terminate the summation over particle interactions at a certain distance only when the illumination spot is of finite extent.

To simulate our experiment with a finite illumination spot, one has to consider that the illumination spot moves over the sample with the tip. The whole system to be simulated changes for each tip position. Therefore, for each pixel, we would have to perform a full field simulation and evaluate the field at the tip position. This seems unreachable within our numeric capabilities. In experiment, however, we can come closer to plane wave illumination. We increase the illumination spot size in our

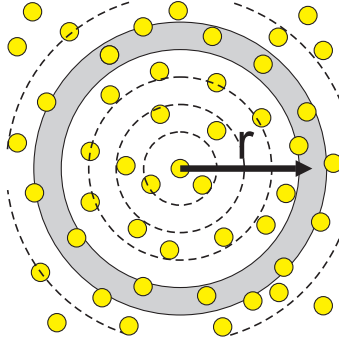


Figure 5.3.: The interaction between two individual dipolar discs decays with distance as $1/r$. However, the number of particles in a certain distance $r \pm dr$ increases linearly with r . The sum of their interaction may not vanish after a certain distance.

setup by placing an iris in the illumination path, reducing the numerical aperture of the incident beam. Experiment with different illumination spot sizes from $2 \mu\text{m}$ to about $4 \mu\text{m}$ are shown in Fig. 5.4. With increasing illumination size, the fluctuations in dipole angles become wider, closer to simulation (see Fig. 5.5). For the case of plane wave illumination, it eventually converges towards the simulated values.

From the measurements (Fig. 5.4) we conclude that the optical response of this amorphous metamaterial strongly depends on illumination conditions. Nearfields on the sample and the formation of hotspots can be manipulated by changing the numerical aperture of illumination. For SERS applications, this means that a surface does not have a "hotspot" by itself, but the formation of strong fields also depends on the incident radiation. As coherent interactions from long distance neighbors have to be considered, numerical predictions of hotspot positions on extended sample surfaces seem impossible.

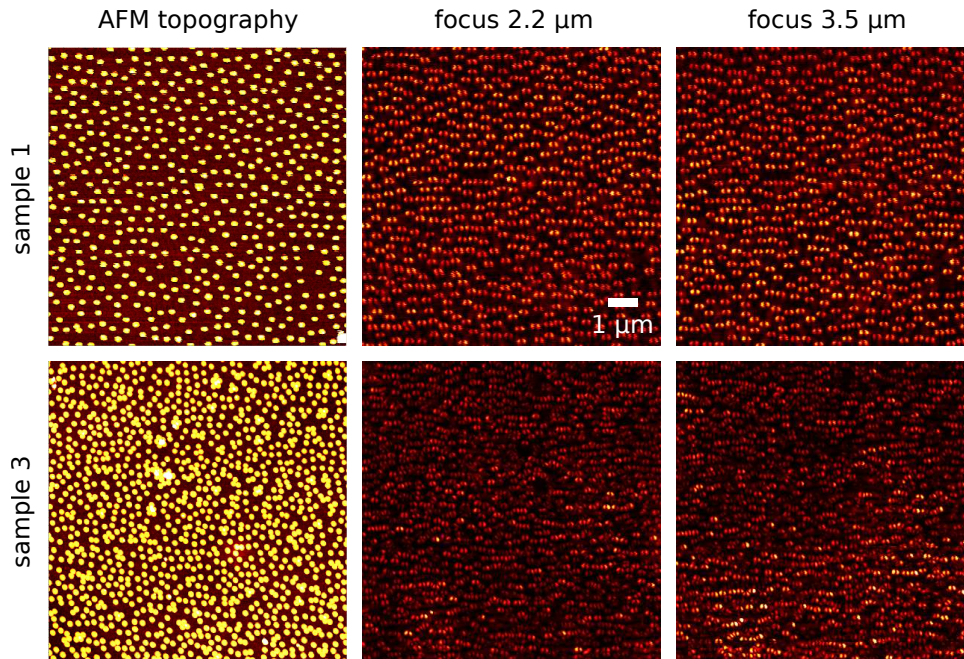


Figure 5.4.: Comparison of nearfield images taken with different illumination spot sizes. An iris is placed in the illumination beam path, reducing the numerical aperture of the incident focal spot. The laser power is increased to compensate for the intensity loss on the sample.

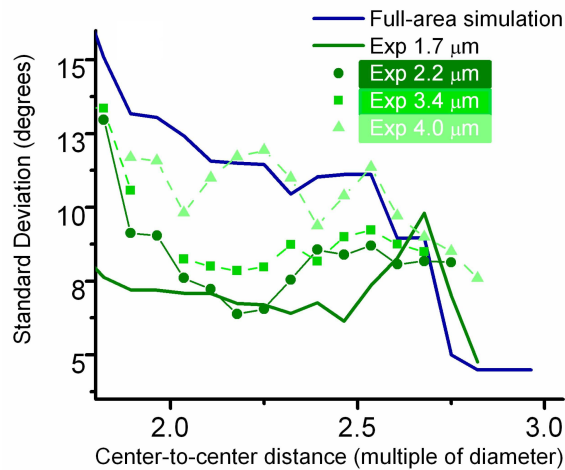


Figure 5.5.: Statistical analysis of dipole orientations for different illumination spot sizes. When increasing the focus spot diameter in experiment towards the simulation illumination condition, also the standard deviation of dipole orientations gets closer to the simulated values. [169]

Chapter 6.

Plasmons in Tensorial Media

Modern electronics is revolutionizing our lives in areas such as computing, telecommunication, or solar energy harvesting. Various performance characteristics are improving geometrically in time, following Moore's law. The current challenges to overcome on this continued track shift the focus of attention more and more on the interplay of electronic and optical material aspects. Indeed, electronic operating frequencies well beyond 10 – 100 GHz increasingly require a (far-infrared) optical rather than electronic description.

For instance, the critical bottleneck for faster computing lies currently not with the transistor-based processing units. Rather it is the data transmission lines that connect them through limited interface areas, which need to carry signal fields of ever higher frequencies yet ever smaller cross section. A solution may be found in surface plasmon polaritonic (SPP) waveguides.[15] In contrast to photonic modes bound in micron-sized dielectric waveguides, SPPs are confined within tens of nm,[171] exploiting the negative electric permittivity of metals at optical frequencies. However, intrinsic ohmic losses restrict operational SPP devices currently to short length scales of a few μm . Such limitations have resulted in increase efforts to search for alternative plasmonic materials beyond gold, silver and aluminium.[36] SPPs are one example of the generic class of polaritonic phenomena, whose common feature is the coupling of photonic modes with a resonance of the electronic crystal field.[172]

6.1. Introduction

Depending on the application, different materials appear favorable for plasmonic devices.[8, 173] Promising candidates have been found in doped semiconductors, which optically behave like metals with tunable plasma frequency.[37] Metal-like behavior, that is, negative permittivity allowing for subwavelength bound modes, can also be found in other non-metals, [172] as already demonstrated in nearfield measurements of phonon polariton modes.[40] In this report, we extend the search for plasmonic materials to non-metals. In addition to plasmon polaritons, also other quasi-particles like the phonon polariton or exciton polariton can achieve negative permittivities at frequencies close to strong and narrow material resonances.[172]

They offer a plethora of metal-like materials awaiting applications. In polaritronics, that is the combination of polaritonic modes and electronics, [174, 175, 176] many concepts from plasmonic circuitry can be generalized to polaritons.

Recently, combinations of plasmonic and electronic devices have been demonstrated, [177] converting electric currents to plasmons [178, 179] or vice versa. [180, 181] New possibilities open up when considering also non-metals for plasmonics or polaritronics, that cannot be achieved with metals: The optical response can be tuned by material doping, phononic and excitonic interactions can be utilized for strongly dispersive polaritonic modes and optical devices can be directly implemented into electronic circuits.

An example for this class of materials is graphite and its single layer version graphene. In addition to the plasmon polariton in the infrared [182], an exciton polariton is predicted at energies around 5 eV, [183], in agreement with recent absorption measurements.[184] Here, we concentrate on bismuth selenide (Bi_2Se_3). Bismuth selenide is a semiconductor with a bandgap of about 300 meV. Like graphite, it is a layered material. Five hexagonal atomic layers form a quintuple layer, that couples to adjacent layers by van-der-Waals forces. In analogy to graphite,[185] we expect an anisotropic optical response.

6.2. Ellipsometry

Optically, bismuth selenide was investigated earlier by reflectometry methods, [186] accessing the degenerate permittivity components in the hexagonal planes, and infrared ellipsometry. [187] In this report, we measure and reconstruct all components of the permittivity tensor by means of ellipsometry from near-IR to UV frequencies. We optically characterize a Bi_2Se_3 single crystal, grown by a vertical Bridgman method [188] in reflection geometry from the mid-IR to the UV spectrum (0.62 eV to 4.3 eV). The Bi_2Se_3 crystal is characterized at room temperature by generalized spectroscopy ellipsometry using a rotating analyzer spectroscopic ellipsometer (Woollam VASE). The measurements are carried out in the spectral range between 5000 to 35000 cm^{-1} (0.62 to 4.3 eV) with a resolution of 100 cm^{-1} . Measurements are performed at angles of incidence from 55° to 75° in steps of 10° . The optical properties of Bi_2Se_3 are modelled by an uniaxial single crystal model, with an xy-plane isotropy and anisotropy along the z direction, characterized by two equal components of the permittivity tensor along x and y and an independent function in the z direction. The obtained permittivity not only fits to all measured ellipsometric angles, but also perfectly describes the previously published reflectivity data at normal incidence. [186]

The reconstruction of the permittivity tensor shows that Bi_2Se_3 is optically anisotropic (see Fig. 6.2). The permittivity tensor is diagonal - in our convention with the z-direction aligned to the crystal c-axis. The two permittivity values in the Bi_2Se_3

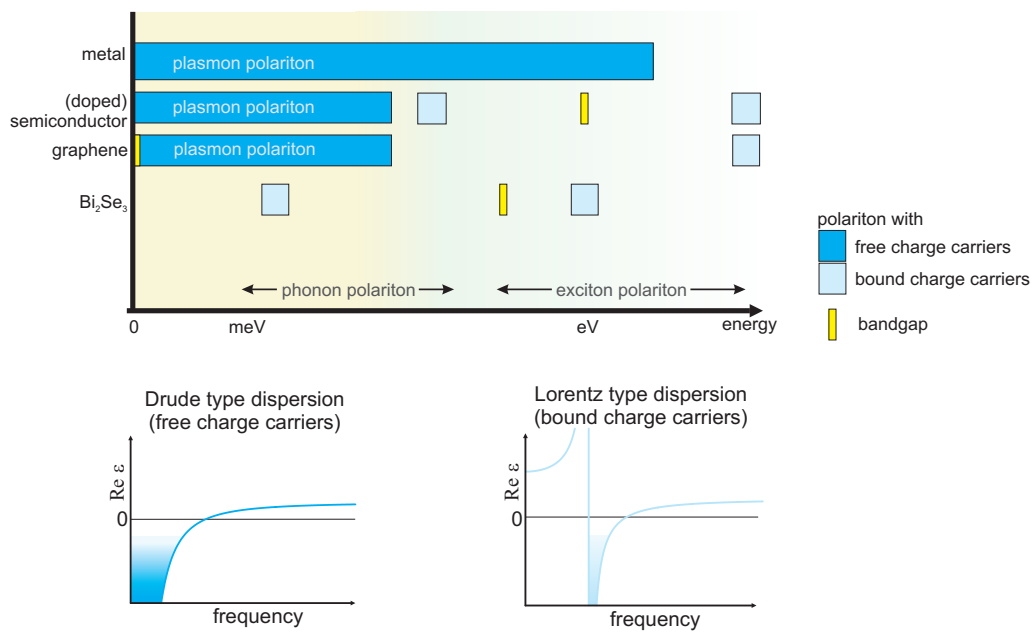


Figure 6.1.: Relative energy scales in different materials for polaritronics. It has been long appreciated that not only free electron Drude-type dispersion, but also Lorentz-type material resonances give rise to negative electric permittivity. Optically, such materials allow for bound optical modes similar to the plasmon polariton. This allows to adapt a multitude of applications from plasmonics to different types of polaritons.

quintuple layer planes are degenerate, leading to only two independent components in the permittivity tensor - the xy and the z-component. Each component shows an absorption peak in the spectral range observed. The absorption maxima appear clearly separated at 1.1 eV for the z-component and 1.7 eV for the xy-component, matching the positions of interband transitions at the Z- and F-point in the Brillouin zone, respectively.[189] The Kramers-Kronig relation links the absorption of these transitions to dispersion in the real part of the permittivity. The strength of the resonances is large enough so that the real part of the permittivity becomes negative. As the absorption peaks appear at different energies, both components are negative in different spectral regions. Bismuth selenide is a rather rare case of a strongly anisotropic material with crossings of the permittivity component real parts over the spectrum. It even has positive (dielectric) and negative (metal-like) components in its permittivity tensor in certain spectral regions. At energies between 1.1 and 1.7 eV, the xy-component is positive, while the z-component is negative. At 1.7 eV, the real parts of the permittivity tensor components cross at $\epsilon = -0.3$. The tensor components exchange their respective roles: At higher energies, both x and y components are negative, while the z-component behaves dielectric.

6.3. Planar Interfaces

Bismuth selenide shows negative dielectric permittivity, so in analogy to plasmonics one expects bound optical surface modes. Plasmon polaritons are found at interfaces of a positive and a negative permittivity material. The hybrid permittivity of bismuth selenide with positive and negative components leads to the question, whether polaritonic modes, bound to the surface, can also exist at the interface between Bi_2Se_3 and air. For scalar media, the plasmon dispersion relation is well known:

$$k_{scalar} = k_0 \sqrt{\frac{\epsilon_1 \epsilon_2}{\epsilon_1 + \epsilon_2}} \quad (6.1)$$

where k_0 is the vacuum wavenumber and all permittivities are measured relative to the vacuum dielectric constant. We call this mode a bound mode, if the fields decay in the direction normal to the surface. The surface mode dispersion between a scalar medium 1 and a diagonal tensorial medium 2 can be written in a similar way as [190]

$$k_{\parallel} = k_0 \alpha \sqrt{\frac{\beta \epsilon_{2\perp}}{\beta + \epsilon_{2\perp}}} \quad (6.2)$$

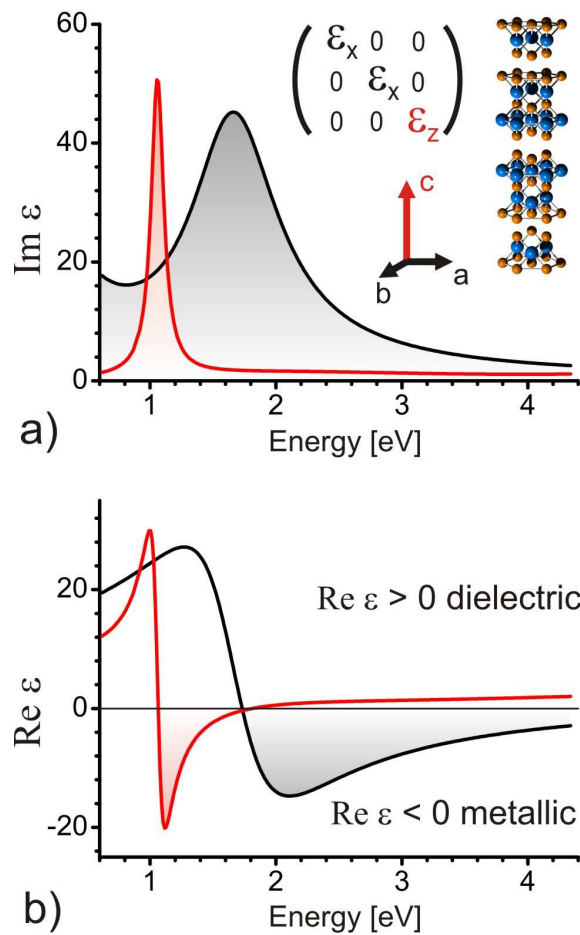


Figure 6.2.: Electric permittivity retrieved from ellipsometry measurements of Bi_2Se_3 . The permittivity tensor is diagonal and degenerate in the crystal ab plane. For clarity, the conventional Bi_2Se_3 unit cell is shown as inset in (a). Imaginary (a) and real part (b) of the permittivity tensor show strong anisotropy of Bi_2Se_3 .

with $\alpha = \sqrt{(\epsilon_1 - \epsilon_{2\parallel})/\epsilon_1}$ and $\beta = -\epsilon_1^2/\epsilon_{2\parallel}$. The index \parallel denotes components parallel to the plasmon wavevector and \perp the direction of the surface normal, respectively. A tensorial permittivity, as offered by Bi_2Se_3 , allows for additional degrees of freedom for electromagnetic surface modes. The polariton dispersion can be tuned by material composition, altering the parallel and perpendicular permittivity component and thus the ratio of α and β . Also, the polariton propagation constant depends on the direction on the surface.

For selected directions, calculated polariton dispersions of a bismuth selenide-air interface Eq. (6.2) are shown in Fig. 6.3. On the [0001] crystal surface facet (green line), calculations exhibit a weakly bound mode at high energies, degenerate for all directions in the surface plane. On [1000] facets, the surface mode dispersion is anisotropic. Between 1.1 eV and 1.7 eV, where the z-permittivity component is negative, there is a uniaxial mode: In direction of the crystal the b-axis (black line), no bound mode is found. Parallel to the c-axis (blue line), a bound polaritonic mode exists.

While surface plasmon polaritons are already used in commercial sensing devices, extending the sensing concept to all kinds of polaritons allows to use new materials to tune the polariton dispersion Eq. (6.2). Additional degrees of freedom are gained by structuring the polaritonic material. Particle resonances in colloids can be designed in size and shape to specifically increase sensitivity in certain spectral regions. Bismuth selenide particles show similar resonances.

6.4. Particle Polaritons

We choose thin Bi_2Se_3 nanowires as prototype system for sensor antennas and data transmission waveguides. The Bi_2Se_3 nano-rods for aSNOM measurements are grown by a catalyzed vapour transport mechanism [191, 192] in a horizontal tube furnace equipped with a quartz tube. Bi_2Se_3 powder (99.999 %, Alfa Aesar) is placed in the hot zone of a furnace (500°C). The substrate, thermally oxidized silicon covered with 5 nm of bismuth, is placed in the down stream zone 11 cm from the hot zone. The quartz tube is repeatedly evacuated to a pressure of about 10^{-3} mbar and flushed with ultrapure argon to remove residual oxygen. An argon flow of 50 sccm is applied at a pressure of 133 mbar. After 30 minutes of evaporation, the furnace is switched off, followed by natural cool down. The nano-rods are mechanically transferred on a thermally oxidized silicon (300 nm SiO_2/Si) substrate.

From the permittivity and the plasmon dispersion on planar surfaces, an illumination energy of 1.17 eV (1064 nm) appears favorable, as at that frequency Bi_2Se_3 has a negative permittivity in z-direction, while losses in this direction are not too high. We investigate the Bi_2Se_3 nanowires with our apertureless scanning near-field optical microscope (see Fig. 6.4). In the measurements, we observe strong field confinement on the Bi_2Se_3 nanowires as also seen in metal wires discussed in chap-

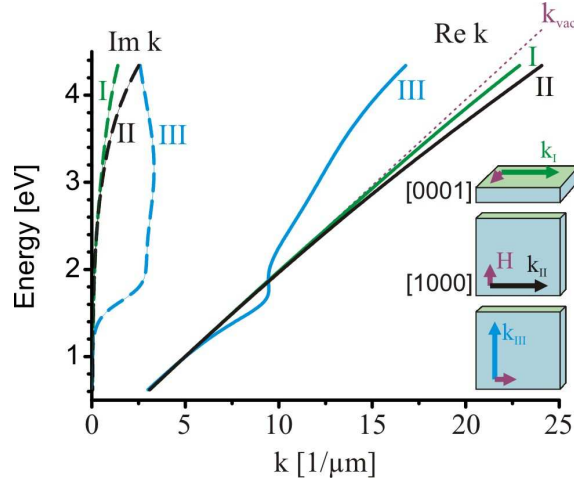


Figure 6.3.: Surface Plasmon dispersion of an Bi_2Se_3 -air interface. Absorption (dashed lines) and propagation constant (solid lines) of three modes on different Bi_2Se_3 crystal facets are shown. For comparison, the vacuum wavenumber is shown as dotted line. On the $[0001]$ facet (green), mode I is degenerate for all directions. On $[1000]$ facets (blue), the surface plasmon dispersion is anisotropic and both modes II and III can be excited.

ter 4. Metal nanowires are well described as quasi-one-dimensional Fabry Perot resonators forming standing wave patterns.[30, 193] In contrast, the local nearfield patterns on bismuth selenide wires appear considerably more complex than in the metal nanowire case. On the wires, we find points with zero optical intensity and phase singularities, that is, an optical phase accumulation of 2π when encircling the minimum.

For numerical simulations, we use our own finite difference time domain (FDTD) code with an analytical model for dispersion.[194] The anisotropy of the material is modeled by considering different permittivity values for lateral and vertical directions with our experimentally acquired permittivity data of bismuth selenide (see Fig. 6.2). The whole simulation domain is discretized by cubic Yee unit-cells of 5 nm size. For the outer boundaries, a higher order absorbing boundary condition is utilized.[195] It is noteworthy that this boundary condition is advantageous over the commonly used perfectly matched layers for large 3D simulations and allows to efficiently make use of the available memory for accurate numerical modeling of the main structure.

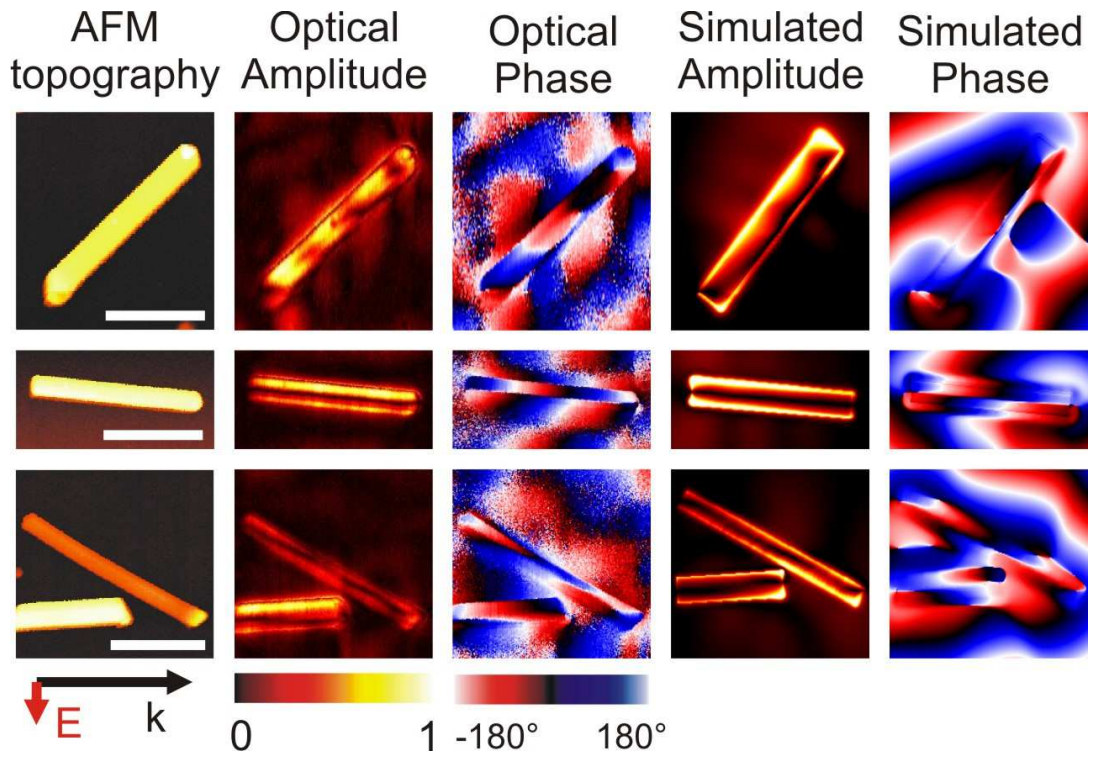


Figure 6.4.: aSNOM images of Bi_2Se_3 nanowires. The wires show complex near-field patterns with phase singularities. FDTD simulations (on the right) are in good agreement with measured optical amplitude and phase at $\lambda = 1064 \text{ nm}$. All scale bars are $1 \mu\text{m}$.

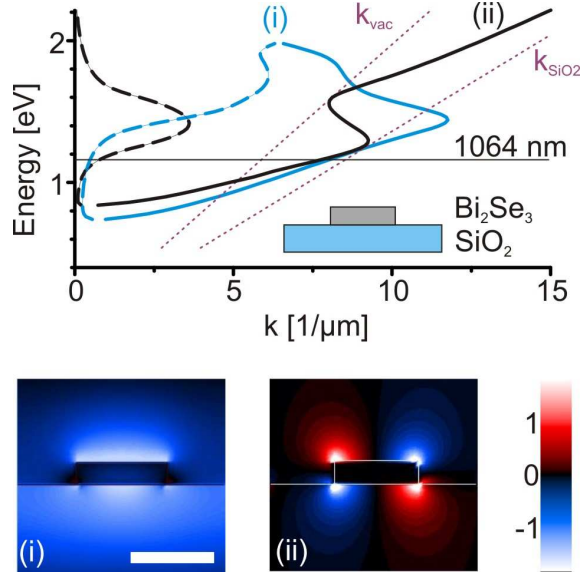


Figure 6.5.: a) Computed dispersion of a channel waveguide composed of a Bi_2Se_3 wire over a silica substrate. At $\lambda = 1064$ nm, two channel modes (i, ii) with low attenuation constants exist. Real part (solid line) and imaginary part (dashed line) of the propagation constants are shown. The instantaneous E_z fields of mode (i) and (ii) displayed below show distinct mode profiles. The scale bar is 200 nm.

We find that numerical and experimental results are in good agreement. Simulations nicely reproduce phase singularities observed in experiment. As bismuth selenide is known as a topological insulator, [189] one might be tempted to associate such phase singularities with the topological features of Bi_2Se_3 . However, topological nontrivial bands are inside the bandgap at much lower energy scales and play no significant role in the description of polaritons in the near-IR.[196, 197] Rather, our analysis points to a classical interference effect.

The anisotropic cross section of the bismuth selenide particles gives rise to multiple waveguide modes. We analyze the mode patterns of Bi_2Se_3 wire waveguides on silicon dioxide substrate with a two-dimensional finite difference frequency domain (FDFD) modal analysis.[198] In FDFD, the 3D simulation is mapped into a 2 dimensional domain, discretized by meshes of 5 nm length. The variation of the field in the third dimension is treated with time-harmonics $\exp(i(\omega t - k_z z))$. The waveguide cross-section of 200 x 60 nm is chosen to fit dimensions of typical wires experimentally observed. At the experimental laser wavelength of 1064 nm, two prominent channel modes (i and ii) are excitable by plane wave illumination (see Fig. 6.5).

The interference of both modes gives rise to the experimentally observed phase singularities and the complex nearfield patterns observed in experiment. This verifies that the experimentally observed mode patterns can be classically understood considering the anisotropic permittivity of Bi_2Se_3 . The dispersion degrees of freedom may be utilized to design special waveguide devices like polarization rotators or selectors.

6.5. Photocurrent on Bismuth Selenide Schottky Diodes

In semiconductor materials for plasmonics, a DC-conductivity with corresponding negative permittivity at low frequencies is achieved by doping. The plasmonic relevant spectral regions are below the bandgap. In contrast, Bi_2Se_3 exhibits a reversal of the energy scales relevant to electronics and polaritons. It has an energy gap of 300 meV, which is well below the photon energy where we observed the particle resonances (1.17 eV). This offers an exciting outlook to use the *same* material volume for both efficient capture of radiation and simultaneous conversion into electric signals. As a preliminary test of the concept, we perform photocurrent imaging in Bi_2Se_3 flakes.

The Bi_2Se_3 flakes are synthesized on a bare Si/SiO₂ substrate by a catalyst-free vapour-solid process similar to the growth mechanism of nanowires described above. The Bi_2Se_3 source material is heated up to 590°C at 80 mbar with a constant Ar flow of 150 sccm. The substrates are placed about 12 cm away from the source material in the down stream zone. We provide the platelets with two contacts patterned by electron beam lithography followed by evaporation of 4 nm Ti and 50 nm Au and a lift-off process.

The sample is locally illuminated with a white light supercontinuum source (Fianium), frequency filtered by an acousto-optical tunable filter and focused on the sample using a 0.8 NA objective (Leica Fluotar 50x) and raster-scanned by a 3 axis piezo stage (Physik Instrumente P-516). We simultaneously record the current generated between both electrodes and the sample reflection with a germanium photodiode in a confocal setup.

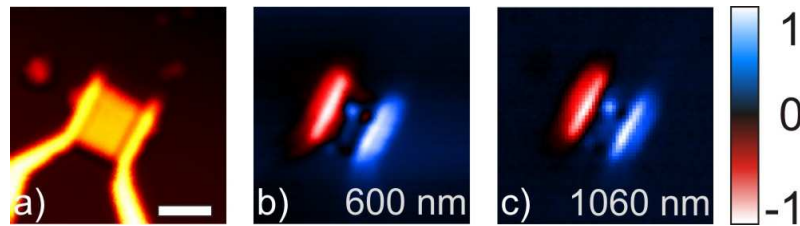


Figure 6.6.: Photocurrent measurements of a Bi_2Se_3 flake, contacted with gold electrodes. (a) Confocal reflection signal of the sample at 600 nm illumination wavelength. The Scale bar is 5 μm . Photocurrent maps are shown upon local illumination with (b) 600 nm and (c) 1064 nm radiation. Color scales in images (b) and (c) are set individually.

Upon illumination with the same wavelength as used for the nearfield characterization (1064 nm), a photocurrent is generated at the $\text{Bi}_2\text{Se}_3/\text{Au}$ interfaces. Typical photocurrent maps are depicted in Fig. 6.6. In the images we see currents only when illuminating the semi-transparent gold electrodes and the underlying interface to the semiconducting bismuth selenide. The currents are of opposite sign when illuminating the two electrodes. This is a clear indication for diode behavior of each interface. The metal contacts create Schottky barriers to the bismuth selenide. [199] A comparison of different illumination wavelengths shows that the shape of the local photocurrent emitting areas does not depend on the wavelength (see Fig. 6.6).

6.6. Discussion

Bi_2Se_3 represents of a whole new class of materials for plasmonics and polaritronics. Although dissipation losses of optical modes might circumvent a direct application in electronic devices, Bi_2Se_3 combines several intriguing properties that are also found in similar materials like bismuth telluride or layered materials in general.

Firstly, bismuth selenide is a semiconductor. Recently, for this material devices like field effect transistors with high on/off ratio have been shown. [200] Together with Bi_2Se_3 photoreceivers, this forms a direct link from optical excitation to electronic data processing.

Secondly, there is the polaritonic aspect. An exciton-polariton causes a negative permittivity at telecom wavelengths in the crystal c -direction. In analogy to the surface plasmon polariton, this property allows subwavelength confinement of light and the application of many design concepts from plasmonics. Another exciton at lower energies forms the basic semiconductor bandgap, usable for electronic devices. The high energy polariton can be directly detected with a photodiode in the same volume, which is a drastic simplification compared to today's standard technology, using metals for transport and a semiconductor for the photoreceiver. [201] In solar cells, plasmonic metal particles are used to concentrate electric fields on the active area. [202, 203, 204, 205] Having both concentration and conversion to electric power in one material, one can exploit the high enhancements directly on the particle surface. Polaritons therefore may achieve enhancement of photovoltaic efficiency in a suitable bandgap material.

The third aspect is the optical anisotropy of bismuth selenide. The rich mode structure in bismuth selenide offers additional degrees of freedom for engineering desired plasmonic response. Semiconductors in general can be doped to alter its optical response. On extended interfaces, the implied opportunities for band structure engineering make a strong case for revisiting many aspect of plasmonic excitations in anisotropic media. As an additional opportunity, we note that anisotropic plasmon propagation can also occur at the interface of scalar metals and anisotropic dielectrics.[190, 206, 207, 208] Another exciting application for anisotropic media has been proposed by Ramakrishna et.al. [209] Superlenses of metal-dielectric multilayers or multiple quantum-well structures [11] also have a metal-dielectric hybrid permittivity tensor. Although their tunability might be limited, bulk anisotropic materials have the appeal that fabrication of thick layers is much easier than for metamaterials.

Chapter 7.

Summary and Outlook

In this thesis, we provided a general and exact framework for the measurable signals in scanning nearfield optical microscopy.[142] The starting point is a form of reciprocity theory appropriate for dissipative, non-magnetic, reciprocal tips. As was already reported earlier by Carminati, Greffet, and coworkers,[68, 67, 65, 66] only the upward traveling components of the coupled tip-sample system contribute to any measurable signal. With the goal of an intuitive formulation that allows immediate conclusions about qualitative aspects of SNOM, our variant of the theory is expressed as an integral over the probing tip's volume, Eq. (2.55). It can be conveniently reduced to the point-like tip case, Eq. (2.56). This latter formulation constitutes an analog to the formula of Tersoff and Hamann for the analysis of scanning tunneling microscopy signals obtained with point-like electrodes.[57, 58] The theoretical framework is applied to typical SNOM configurations. In the crosspolarized aSNOM configuration, our theory verifies the empiric finding that we measure z -component of the electric field at the position of the tip, largely without perturbing the sample modes by the probe.[44, 78] This allows easy and intuitive interpretation of measurements, as shown for a variety of samples in this thesis.

We describe our experimental implementation of an aperturless nearfield microscope. Filtering techniques and systematic alignment of an aSNOM in cross-polarization lead to background-free optical nearfield images. We build upon the well-established techniques of higher harmonic demodulation for discrimination of nearfield signal against background scattering and homodyne interferometric amplification for increased signal strength and access to the complex optical field. The cross-polarization scheme ensures high-fidelity of nearfield optical microscopy. Earlier [44] we showed that signals measured in cross-polarization reproduce very well the vertical component of the electric field of the excited bare sample – as simulated in the absence of any probe tip. The alignment procedure routinely achieves background levels below the detector noise, as we show in various plasmonic device characterizations in this thesis.

In future instrumentation, one might replace all dispersive lenses in the setup by focusing mirrors, making the setup achromatic. This allows for spectroscopic measurements with high resolution in both energy and space. By the use of pulsed

radiation, nonlinear processes can be analyzed. A pump-probe setup affords time-resolution to characterize fast nonlinear processes with aSNOM.

With our aSNOM, we experimentally show the evolution of nearfields on optical Yagi-Uda antennas. Our measurement in optical amplitude and phase allows the reconstruction of the time-harmonic electric fields. In contrast to electron microscopy techniques, like transmission electron microscopy or cathodoluminescence, capacitively and inductively coupled elements of the antenna can be distinguished, giving deep insight into the antenna working principle. From nearfield images illuminating the antennas from the forward and backward direction we conclude the incident field is concentrated on the antenna feed element only upon forward illumination, giving a clear indication of antenna directionality. Optical antennas are suggested for on-chip data connections [210, 24], so high resolution antenna nearfield characterization – a standard tool in radio frequency technology[211] – will most likely gain more importance over the coming years.[93, 31, 212, 213]

In more complex plasmonic circuits, where not the antenna itself is the plasmonic device to be excited, the fields concentrated by antennas must be converted to modes exciting the actual device. We introduce a general approach for elastic plasmon excitation processes. Antennas act as coupling points converting photonic modes to localized or propagating plasmonic modes. Selective excitation of a desired plasmonic mode is achieved by tuning position and phase retardation of the couplers. As a demonstration of the concept we show launchers of unidirectional waveguided modes. The approach allows for extremely compact assemblies, where the total area of the coupler assembly is of deep subwavelength footprint, as small as $\lambda^2/10$. As an outlook, we draw attention to the recent demonstration of self-assembled growth of plasmonic logic gates.[18] The concepts presented are well suited for performing improved addressing and read-out tasks with such circuitry. In combination with active elements, such as high speed modulators, they might also prove useful in amplifier plasmonics.[147]

In addition to optimizing device geometry, also the illumination plays a significant role for efficient excitation of plasmonic devices. In samples of amorphously distributed scatterers, we find a long-range dipole interaction that governs the optical response of the structure. The ability to vary the local response of a plasmonic entity is of immediate interest to the field of hot-spot and energy concentration engineering with applications, for example, in enhanced Raman scattering spectroscopy. Our work also indicates that the very high-field enhancements achieved in SERS [214, 215] might not have their origin in the very local surrounding, but originate from coherent interaction of a larger region. [138]

Device performance can also be enhanced by the choice of suitable materials. On the search for new materials, we found strong optical anisotropy in bismuth selenide. At telecom wavelengths, bismuth selenide has positive and negative components in its dielectric tensor, resulting in an optical response being a hybrid of responses known from typical dielectric and metallic materials. In this spectral region, we

show confinement of light to subwavelength particle modes. The anisotropic nature of bismuth selenide leads to a rich mode structure on the particles, offering additional degrees of freedom in the design of future devices. We experimentally verify the implementation of photodiodes on bismuth selenide flakes in the same spectral region, enabling the conversion of polaritonic resonant modes to electronic circuitry in the same volume. To locally characterize photodiode elements, as a next step one could record the photocurrent injected by the strongly enhanced tip field under incident p-polarization. At the same time, the electric fields on the sample can be recorded in a reciprocal crosspolarization aSNOM configuration.

Bismuth selenide opens up a whole new class of materials to be investigated for suitability in polaritronics. For example with bismuth telluride or antimonide, being completely mixable with bismuth selenide, material properties can be continuously tuned. Also, the optical behavior at energies close to the bandgap is of interest. Experiments in this spectral region require either low temperatures or nonlinear effects like difference frequency generation microscopy with pulsed illumination.

Observing nonlinear optical effects is also necessary in all active optical devices that use polaritons not only for data transport. One example to gain fundamental understanding of light-matter interaction is to investigate electron-phonon coupling. Strong pump pulses heat the plasmonic structures, that then couple to phonons and start to oscillate. [216] A pump pulse reads out the oscillation state. Time-resolved nearfield microscopy is also required to characterize future devices for all-optical signal processing. In complex, subwavelength circuits, it provides high resolution characterization of devices to amplify or switch polaritons or convert them into other quasiparticles.

Bibliography

- [1] S. A. Maier. *Plasmonics: Fundamentals and Applications*. Springer, 2007.
- [2] J. N. Anker, W. P. Hall, O. Lyandres, N. C. Shah, J. Zhao, and R. P. Van Duyne. *Biosensing with plasmonic nanosensors*. *Nature Materials*, **7**(6):442–453, 2008.
- [3] N. L. Rosi and C. A. Mirkin. *Nanostructures in biodiagnostics*. *Chemical Reviews*, **105**(4):1547–1562, 2005. doi: 10.1021/cr030067f.
- [4] E. Ozbay. *Plasmonics: Merging photonics and electronics at nanoscale dimensions*. *Science*, **311**(5758):189–193, 2006. doi: 10.1126/science.1114849.
- [5] P. Neutens, P. Van Dorpe, I. De Vlamincx, L. Lagae, and G. Borghs. *Electrical detection of confined gap plasmons in metal-insulator-metal waveguides*. *Nature Photonics*, **3**:283–286, 2009. doi: 10.1038/nphoton.2009.47.
- [6] M. L. Brongersma, J. W. Hartman, and H. H. Atwater. *Plasmonics: Electromagnetic energy transfer and switching in nanoparticle chain-arrays below the diffraction limit*. *MRS Proceedings*, **582**:H10.5, 1999. doi: 10.1557/PROC-582-H10.5.
- [7] M. L. Brongersma and V. M. Shalaev. *The case for plasmonics*. *Science*, **328**(5977):440–441, 2010. doi: 10.1126/science.1186905.
- [8] D. K. Gramotnev and S. I. Bozhevolnyi. *Plasmonics beyond the diffraction limit*. *Nature Photonics*, **4**:83–91, 2010. doi: 10.1038/nphoton.2009.282.
- [9] C. M. Lieber. *Nanoscale science and technology: Building a big future from small things*. *MRS Bulletin*, **28**:486–491, 2003. doi: 10.1557/mrs2003.144.
- [10] K. L. Kelly, E. Coronado, L. L. Zhao, and G. C. Schatz. *The optical properties of metal nanoparticles: The influence of size, shape, and dielectric environment*. *The Journal of Physical Chemistry B*, **107**(3):668–677, 2003. doi: 10.1021/jp026731y.
- [11] S. A. Maier and H. A. Atwater. *Plasmonics: Localization and guiding of electromagnetic energy in metal/dielectric structures*. *Journal of Applied Physics*, **98**(1):011101, 2005. doi: 10.1063/1.1951057.

- [12] P. K. Jain and M. A. El-Sayed. *Surface plasmon coupling and its universal size scaling in metal nanostructures of complex geometry: Elongated particle pairs and nanosphere trimers*. The Journal of Physical Chemistry C, **112**(13):4954–4960, 2008. doi: 10.1021/jp7120356.
- [13] M. Yoshida and J. Lahann. *Smart nanomaterials*. ACS Nano, **2**(6):1101–1107, 2008. doi: 10.1021/nm800332g.
- [14] N. J. Halas. *Plasmonics: An Emerging Field Fostered by Nano Letters*. Nano Letters, **10**(10):3816–3822, 2010. doi: 10.1021/nl1032342.
- [15] D. Miller. *Device requirements for optical interconnects to silicon chips*. Proceedings of the IEEE, **97**:1166–1185, 2009. doi: 10.1109/JPROC.2009.2014298.
- [16] J. Grandidier, G. C. des Francs, S. Massenot, A. Bouhelier, L. Markey, J.-C. Weeber, C. Finot, and A. Dereux. *Gain-assisted propagation in a plasmonic waveguide at telecom wavelength*. Nano Letters, **9**(8):2935–2939, 2009. doi: 10.1021/nl901314u.
- [17] I. De Leon and P. Berini. *Amplification of long-range surface plasmons by a dipolar gain medium*. Nature Photonics, **4**:382–387, 2010. doi: 10.1038/nphoton.2010.37.
- [18] H. Wei, Z. Wang, X. Tian, M. Käll, and H. Xu. *Cascaded logic gates in nanophotonic plasmon networks*. Nature Communications, **2**:387, 2011. doi: 10.1038/ncomms1388.
- [19] L. Novotny and N. van Hulst. *Antennas for light*. Nature Photonics, **5**:83, 2011. doi: 10.1038/nphoton.2010.237.
- [20] P. Mühlischlegel, H.-J. Eisler, O. J. F. Martin, B. Hecht, and D. W. Pohl. *Resonant optical antennas*. Science, **308**(5728):1607–1609, 2005. doi: 10.1126/science.1111886.
- [21] P. Bharadwaj, B. Deutsch, and L. Novotny. *Optical antennas*. Advances in Optics and Photonics, **1**(3):438–483, 2009. doi: 10.1364/AOP.1.000438.
- [22] N. Liu, M. L. Tang, M. Hentschel, H. Giessen, and A. P. Alivisatos. *Nanoantenna-enhanced gas sensing in a single tailored nanofocus*. Nature Materials, **10**:631–636, 2011. doi: 10.1038/nmat3029.
- [23] A. G. Curto, G. Volpe, T. H. Taminiau, M. P. Kreuzer, R. Quidant, and N. F. van Hulst. *Unidirectional emission of a quantum dot coupled to a nanoantenna*. Science, **329**(5994):930–933, 2010. doi: 10.1126/science.1191922.

-
- [24] D. Dregely, R. Taubert, J. Dorfmueller, R. Vogelgesang, K. Kern, and H. Giessen. *3D optical Yagi-Uda nanoantenna array*. Nature Communications, **2**:267, 2011. doi: 10.1038/ncomms1268.
- [25] J. R. Heath. *Size-dependent surface-plasmon resonances of bare silver particles*. Physical Review B, **40**:9982–9985, 1989. doi: 10.1103/PhysRevB.40.9982.
- [26] T. V. Shahbazyan, I. E. Perakis, and J.-Y. Bigot. *Size-dependent surface plasmon dynamics in metal nanoparticles*. Physical Review Letters, **81**:3120–3123, 1998. doi: 10.1103/PhysRevLett.81.3120.
- [27] C. J. Orendorff, T. K. Sau, and C. J. Murphy. *Shape-dependent plasmon-resonant gold nanoparticles*. Small, **2**(5):636–639, 2006. doi: 10.1002/smll.200500299.
- [28] C. Noguez. *Surface plasmons on metal nanoparticles: The influence of shape and physical environment*. The Journal of Physical Chemistry C, **111**(10):3806–3819, 2007. doi: 10.1021/jp066539m.
- [29] C. L. Nehl and J. H. Hafner. *Shape-dependent plasmon resonances of gold nanoparticles*. The Royal Society of Chemistry, **18**:2415–2419, 2008. doi: 10.1039/b714950f.
- [30] J. Dorfmueller, R. Vogelgesang, W. Khunsin, C. Rockstuhl, C. Etrich, and K. Kern. *Plasmonic nanowire antennas: Experiment, simulation, and theory*. Nano Letters, **10**(9):3596–3603, 2010. doi: 10.1021/nl101921y.
- [31] J. Dorfmueller, R. Vogelgesang, R. T. Weitz, C. Rockstuhl, C. Etrich, T. Pertsch, F. Lederer, and K. Kern. *Fabry-Pérot resonances in one-dimensional plasmonic nanostructures*. Nano Letters, **9**(6):2372–2377, 2009. doi: 10.1021/nl900900r.
- [32] A. Boltasseva, T. Nikolajsen, K. Leosson, K. Kjaer, M. Larsen, and S. Bozhevolnyi. *Integrated optical components utilizing long-range surface plasmon polaritons*. Journal of Lightwave Technology, **23**(1):413–422, 2005. doi: 10.1109/JLT.2004.835749.
- [33] R. F. Oulton, V. J. Sorger, D. A. Genov, D. F. P. Pile, and X. Zhang. *A hybrid plasmonic waveguide for subwavelength confinement and long-range propagation*. Nature Photonics, **2**:496, 2008. doi: 10.1038/nphoton.2008.131.
- [34] D. E. Chang, A. S. Sørensen, P. R. Hemmer, and M. D. Lukin. *Quantum optics with surface plasmons*. Physical Review Letters, **97**:053002, 2006. doi: 10.1103/PhysRevLett.97.053002.

- [35] E. Altewischer, M. P. van Exter, and J. P. Woerdman. *Plasmon-assisted transmission of entangled photons*. Nature, **418**:304–306, 2002. doi: 10.1038/nature00869.
- [36] A. Boltasseva and H. A. Atwater. *Low-loss plasmonic metamaterials*. Science, **331**(6015):290–291, 2011. doi: 10.1126/science.1198258.
- [37] A. Frölich and M. Wegener. *Spectroscopic characterization of highly doped ZnO films grown by atomic-layer deposition for three-dimensional infrared metamaterials*. Optical Materials Express, **1**(5):883–889, 2011. doi: 10.1364/OME.1.000883.
- [38] J. Plumridge, E. Clarke, R. Murray, and C. Phillips. *Ultra-strong coupling effects with quantum metamaterials*. Solid State Communications, **146**:406–408, 2008. doi: 10.1016/j.ssc.2008.03.027.
- [39] G. D. Mahan and G. Obermair. *Polaritons at surfaces*. Physical Review, **183**:834–841, 1969. doi: 10.1103/PhysRev.183.834.
- [40] T. Taubner, D. Korobkin, Y. Urzhumov, G. Shvets, and R. Hillenbrand. *Near-field microscopy through a SiC superlens*. Science, **313**(5793):1595, 2006. doi: 10.1126/science.1131025.
- [41] R. Vogelgesang and A. Dmitriev. *Real-space imaging of nanoplasmonic resonances*. Analyst, **135**:1175–1181, 2010. doi: 10.1039/c000887g.
- [42] B. Knoll and F. Keilmann. *Enhanced dielectric contrast in scattering-type scanning near-field optical microscopy*. Optics Communications, **182**(4-6):321–328, 2000. doi: 10.1016/S0030-4018(00)00826-9.
- [43] R. Hillenbrand and F. Keilmann. *Optical oscillation modes of plasmon particles observed in direct space by phase-contrast near-field microscopy*. Applied Physics B, **73**:239–243, 2001. doi: 10.1007/s003400100656.
- [44] R. Esteban, R. Vogelgesang, J. Dorfmueller, A. Dmitriev, C. Rockstuhl, C. Etrich, and K. Kern. *Direct near-field optical imaging of higher order plasmonic resonances*. Nano Letters, **8**(10):3155–3159, 2008. doi: 10.1021/nl801396r.
- [45] A. Cvitkovic, N. Ocelic, and R. Hillenbrand. *Analytical model for quantitative prediction of material contrasts in scattering-type near-field optical microscopy*. Optics Express, **15**(14):8550–8565, 2007. doi: 10.1364/OE.15.008550.
- [46] E. Prodan, C. Radloff, N. J. Halas, and P. Nordlander. *A hybridization model for the plasmon response of complex nanostructures*. Science, **302**(5644):419–422, 2003. doi: 10.1126/science.1089171.

-
- [47] R. Vogelgesang, J. Dorfmueller, R. Esteban, R. T. Weitz, A. Dmitriev, and K. Kern. *Plasmonic nanostructures in aperture-less scanning near-field optical microscopy (aSNOM)*. *Physica Status Solidi B*, **245**(10):2255–2260, 2008. doi: 10.1002/pssb.200879617.
- [48] F. Hao, Y. Sonnefraud, P. Van Dorpe, S. A. Maier, N. J. Halas, and P. Nordlander. *Symmetry breaking in plasmonic nanocavities: Subradiant LSPR sensing and a tunable Fano resonance*. *Nano Letters*, **8**(11):3983–3988, 2008. doi: 10.1021/nl802509r.
- [49] A. García-Etxarri, I. Romero, F. J. García de Abajo, R. Hillenbrand, and J. Aizpurua. *Influence of the tip in near-field imaging of nanoparticle plasmonic modes: Weak and strong coupling regimes*. *Physical Review B*, **79**(12):125439, 2009. doi: 10.1103/PhysRevB.79.125439.
- [50] N. Verellen, Y. Sonnefraud, H. Sobhani, F. Hao, V. V. Moshchalkov, P. Van Dorpe, P. Nordlander, and S. A. Maier. *Fano resonances in individual coherent plasmonic nanocavities*. *Nano Letters*, **9**(4):1663–1667, 2009. doi: 10.1021/nl9001876.
- [51] J.-J. Greffet and R. Carminati. *Image formation in near-field optics*. *Progress in Surface Science*, **56**(3):133 – 237, 1997. doi: 10.1016/S0079-6816(98)00004-5.
- [52] P. S. Carney and J. C. Schotland. *Inverse scattering for near-field microscopy*. *Applied Physics Letters*, **77**(18):2798–2800, 2000. doi: 10.1063/1.1320844.
- [53] P. S. Carney, R. A. Frazin, S. I. Bozhevolnyi, V. S. Volkov, A. Boltasseva, and J. C. Schotland. *Computational lens for the near field*. *Physical Review Letters*, **92**:163903, 2004. doi: 10.1103/PhysRevLett.92.163903.
- [54] V. Kosobukin. *Theory of scanning near-field magneto-optical microscopy*. *Technical Physics*, **43**:824–829, 1998. doi: 10.1134/1.1259079.
- [55] J. N. Walford, J.-A. Porto, R. Carminati, and J.-J. Greffet. *Theory of near-field magneto-optical imaging*. *Journal of the Optical Society of America A*, **19**(3):572–583, 2002. doi: 10.1364/JOSAA.19.000572.
- [56] T. H. Taminiau, R. J. Moerland, F. B. Segerink, L. K. Kuipers, and N. F. van Hulst. *$\lambda/4$ resonance of an optical monopole antenna probed by single molecule fluorescence*. *Nano Letters*, **7**(1):28–33, 2007. doi: 10.1021/nl061726h.
- [57] J. Tersoff and D. R. Hamann. *Theory and application for the scanning tunneling microscope*. *Physical Review Letters*, **50**:1998–2001, 1983. doi: 10.1103/PhysRevLett.50.1998.

- [58] J. Tersoff and D. R. Hamann. *Theory of the scanning tunneling microscope*. Physical Review B, **31**:805–813, 1985. doi: 10.1103/PhysRevB.31.805.
- [59] J. Bardeen. *Tunnelling from a many-particle point of view*. Physical Review Letters, **6**:57–59, 1961. doi: 10.1103/PhysRevLett.6.57.
- [60] Pohl. *Near-field photon tunneling devices using liquid metal*, 1997.
- [61] J. Krenn, R. Wolf, A. Leitner, and F. Aussenegg. *Near-field optical imaging the surface plasmon fields of lithographically designed nanostructures*. Optics Communications, **137**(1-3):46–50, 1997. doi: 10.1016/S0030-4018(96)00710-9.
- [62] J. Krenn, A. Dereux, J. Weeber, E. Bourillot, Y. Lacroute, J. Goudonnet, G. Schider, W. Gotschy, A. Leitner, F. Aussenegg, and C. Girard. *Squeezing the optical near-field zone by plasmon coupling of metallic nanoparticles*. Physical Review Letters, **82**(12):2590–2593, 1999. doi: 10.1103/PhysRevLett.82.2590.
- [63] R. Carminati and J. J. Sáenz. *Scattering theory of Bardeen’s formalism for tunneling: New approach to near-field microscopy*. Physical Review Letters, **84**:5156–5159, 2000. doi: 10.1103/PhysRevLett.84.5156.
- [64] J. Koglin, U. C. Fischer, and H. Fuchs. *Material contrast in scanning near-field optical microscopy at 1–10 nm resolution*. Physical Review B, **55**:7977–7984, 1997. doi: 10.1103/PhysRevB.55.7977.
- [65] R. Carminati, J. J. Sáenz, J.-J. Greffet, and M. Nieto-Vesperinas. *Reciprocity, unitarity, and time-reversal symmetry of the S matrix of fields containing evanescent components*. Physical Review A, **62**:012712, 2000. doi: 10.1103/PhysRevA.62.012712.
- [66] J. A. Porto, R. Carminati, and J. J. Greffet. *Theory of electromagnetic field imaging and spectroscopy in scanning near-field optical microscopy*. Journal of Applied Physics, **88**(8):4845–4850, 2000. doi: 10.1063/1.1311811.
- [67] R. Carminati, M. Nieto-Vesperinas, and J.-J. Greffet. *Reciprocity of evanescent electromagnetic waves*. Journal of the Optical Society of America A, **15**(3):706–712, 1998. doi: 10.1364/JOSAA.15.000706.
- [68] E. Mendez, J.-J. Greffet, and R. Carminati. *On the equivalence between the illumination and collection modes of the scanning near-field optical microscope*. Optics Communications, **142**:7 – 13, 1997. doi: 10.1016/S0030-4018(97)00268-X.
- [69] H. De Raedt, A. Lagendijk, and P. de Vries. *Transverse localization of light*. Physical Review Letters, **62**(1):47–50, 1989. doi: 10.1103/PhysRevLett.62.47.

-
- [70] O. Steuernagel. *Equivalence between focused paraxial beams and the quantum harmonic oscillator*. American Journal of Physics, **73**(7):625–629, 2005. doi: 10.1119/1.1900099.
- [71] J. R. Carson. *A generalization of the reciprocal theorem*. Bell System Technical Journal, **3**:393–399, 1924.
- [72] J. D. Jackson. *Classical electrodynamics (Third ed.)*. New York: Wiley, 1998.
- [73] R. E. Collin. *Field Theory of Guided Waves*. Oxford University Press, 1990.
- [74] L. D. Landau and E. M. Lifshitz. *Electrodynamics of Continuous Media*. Pergamon Press, 1963.
- [75] J. Schwinger, L. Deraad Jr., K. Milton, W. Tsai, and J. Norton. *Classical Electrodynamics*. Westview Press, 1998.
- [76] J. Nye. *Physical Properties of Crystals: Their Representation by Tensors and Matrices*. Oxford University Press, 1957.
- [77] G. D. Monteath. *Applications of the Electromagnetic Reciprocity Principle*. Pergamon Press, 1973.
- [78] M. Esslinger, J. Dorfmueller, W. Khunsin, R. Vogelgesang, and K. Kern. *Background-free imaging of plasmonic structures with cross-polarized apertureless scanning near-field optical microscopy*. Review of Scientific Instruments, **83**(3):033704, 2012. doi: 10.1063/1.3693346.
- [79] A. S. Marathay. *Fourier transform of the green’s function for the helmholtz equation*. Journal of the Optical Society of America, **65**(8):964–965, 1975. doi: 10.1364/JOSA.65.000964.
- [80] C. A. Balanis. *Advanced Engineering Electromagnetics*. Wiley, 1989.
- [81] J. Sun and P. S. Carney. *Strong tip effects in near-field scanning optical tomography*. Journal of Applied Physics, **102**:103103, 2007. doi: 10.1063/1.2812545.
- [82] R. Vogelgesang, R. Esteban, and K. Kern. *Beyond lock-in analysis for volumetric imaging in apertureless scanning near-field optical microscopy*. Journal of Microscopy, **229**(2):365–370, 2008. doi: 10.1111/j.1365-2818.2008.01913.x.
- [83] R. Esteban, R. Vogelgesang, and K. Kern. *Simulation of optical near and far fields of dielectric apertureless scanning probes*. Nanotechnology, **17**(2):475–482, 2006. doi: 10.1088/0957-4484/17/2/022.

- [84] R. Hillenbrand and F. Keilmann. *Complex optical constants on a subwavelength scale*. Physical Review Letters, **85**(14):3029–3032, 2000. doi: 10.1103/PhysRevLett.85.3029.
- [85] M. B. Raschke and C. Lienau. *Apertureless near-field optical microscopy: Tip-sample coupling in elastic light scattering*. Applied Physics Letters, **83**(24):5089–5091, 2003. doi: 10.1063/1.1632023.
- [86] A. Bek. *Apertureless SNOM: A new Tool for Nano-Optics*. Ph.D. thesis, Ecole Polytechnique Federale de Lausanne, 2004.
- [87] A. Bek. *Apertureless SNOM: A New Tool for Nano-Optics*. Saarbrücken: Lap Lambert Academic Publishing, 2011.
- [88] J. Renger, S. Grafström, L. M. Eng, and R. Hillenbrand. *Resonant light scattering by near-field-induced phonon polaritons*. Physical Review B, **71**(7):075410, 2005. doi: 10.1103/PhysRevB.71.075410.
- [89] B. Deutsch, R. Hillenbrand, and L. Novotny. *Visualizing the optical interaction tensor of a gold nanoparticle pair*. Nano Letters, **10**(2):652–656, 2010. doi: 10.1021/nl9037505.
- [90] P. B. Johnson and R. W. Christy. *Optical constants of the noble metals*. Physical Review B, **6**:4370–4379, 1972. doi: 10.1103/PhysRevB.6.4370.
- [91] J. N. Walford, J. A. Porto, R. Carminati, J.-J. Greffet, P. M. Adam, S. Hudlet, J.-L. Bijeon, A. Stashkevich, and P. Royer. *Influence of tip modulation on image formation in scanning near-field optical microscopy*. Journal of Applied Physics, **89**(9):5159–5169, 2001. doi: 10.1063/1.1359153.
- [92] T. Zentgraf, J. Dorfmüller, C. Rockstuhl, C. Etrich, R. Vogelgesang, K. Kern, T. Pertsch, F. Lederer, and H. Giessen. *Amplitude- and phase-resolved optical near fields of split-ring-resonator-based metamaterials*. Optics Letters, **33**(8):848–850, 2008. doi: 10.1364/OL.33.000848.
- [93] J. Dorfmüller, D. Dregely, M. Esslinger, W. Khunsin, R. Vogelgesang, K. Kern, and H. Giessen. *Near-field dynamics of optical Yagi-Uda nanoantennas*. Nano Letters, **11**(7):2819–2824, 2011. doi: 10.1021/nl201184n.
- [94] M. Schnell, A. Garcia-Etxarri, J. Alkorta, J. Aizpurua, and R. Hillenbrand. *Phase-resolved mapping of the near-field vector and polarization state in nanoscale antenna gaps*. Nano Letters, **10**(9):3524–3528, 2010. doi: 10.1021/nl101693a.

-
- [95] P. Alonso-González, P. Albella, M. Schnell, J. Chen, F. Huth, A. García-Etxarri, F. Casanova, F. Golmar, L. Arzubiaga, L. Hueso, J. Aizpurua, and R. Hillenbrand. *Resolving the electromagnetic mechanism of surface-enhanced light scattering at single hot spots*. Nature Communications, **3**:684, 2012. doi: 10.1038/ncomms1674.
- [96] A. McLeod, A. Weber-Bargioni, Z. Zhang, S. Dhuey, B. Harteneck, J. B. Neaton, S. Cabrini, and P. J. Schuck. *Nonperturbative visualization of nanoscale plasmonic field distributions via photon localization microscopy*. Physical Review Letters, **106**(3):037402, 2011. doi: 10.1103/PhysRevLett.106.037402.
- [97] A. Bek, R. Vogelgesang, and K. Kern. *Apertureless scanning near field optical microscope with sub-10 nm resolution*. Review of Scientific Instruments., **77**(4):043703, 2006. doi: 10.1063/1.2190211.
- [98] J. Dorfmueller. *Optical Wire Antennas: Near-Field Imaging, Modeling and Emission Patterns*. Ph.D. thesis, Ecole Polytechnique Federale de Lausanne, 2010.
- [99] A. Bek, R. Vogelgesang, and K. Kern. *Optical nonlinearity versus mechanical anharmonicity contrast in dynamic mode apertureless scanning near-field optical microscopy*. Applied Physics Letters, **87**(16):163115, 2005. doi: 10.1063/1.2108125.
- [100] E. O. Potma, W. P. de Boeij, and D. A. Wiersma. *Femtosecond dynamics of intracellular water probed with nonlinear optical Kerr effect microspectroscopy*. Biophysics Journal, **80**(6):3019–3024, 2001. doi: 10.1016/S0006-3495(01)76267-4.
- [101] L. Gomez, R. Bachelot, A. Bouhelier, G. P. Wiederrecht, S.-H. Chang, S. Gray, F. Hua, S. Jeon, J. Rogers, M. Castro, S. Blaize, I. Stefanon, G. Lerondel, and P. Royer. *Apertureless scanning near-field optical microscopy: a comparison between homodyne and heterodyne approaches*. Journal of the Optical Society of America B, **23**(5):823–833, 2006. doi: 10.1364/JOSAB.23.000823.
- [102] Y. Oshikane, S. Hara, T. Matsuda, H. Inoue, M. Nakano, and T. Kataoka. *Observation of localized optical near-field generated by submicron two-hole structure for novel SNOM probe*. Surface and Interface Analysis, **40**(6-7):1054–1058, 2008. doi: 10.1002/sia.2830.
- [103] R. C. Dorf. *The electrical engineering handbook*. CRC Taylor & Francis, 2006.
- [104] D. J. Schroeder. *Astronomical Optics*. Academic Press, San Diego, 2 edition, 2000.

- [105] R. Loudon. *The Quantum Theory of Light*. Oxford University Press, Oxford, New York, 3rd edition, 2000.
- [106] B. Deutsch, R. Hillenbrand, and L. Novotny. *Near-field amplitude and phase recovery using phase-shifting interferometry*. *Optics Express*, **16**(2):494–501, 2008. doi: 10.1364/OE.16.000494.
- [107] N. Ocelic, A. J. Huber, and R. Hillenbrand. *Pseudoheterodyne detection for background-free near-field spectroscopy*. *Applied Physics Letters*, **89**(10):101124, 2006. doi: 10.1063/1.2348781.
- [108] L. Novotny, R. Bian, and X. Xie. *Theory of nanometric optical tweezers*. *Physical Review Letters*, **79**(4):645–648, 1997. doi: 10.1103/PhysRevLett.79.645.
- [109] M. Rang, A. C. Jones, F. Zhou, Z.-Y. Li, B. J. Wiley, Y. N. Xia, and M. B. Raschke. *Optical near-field mapping of plasmonic nanoprisms*. *Nano Letters*, **8**(10):3357–3363, 2008. doi: 10.1021/nl801808b.
- [110] R. Esteban, R. Vogelgesang, and K. Kern. *Tip-substrate interaction in optical near-field microscopy*. *Physical Review B*, **75**(19):195410, 2007. doi: 10.1103/PhysRevB.75.195410.
- [111] C. Hafner. *Die MMP-Methode*. *Archiv für Elektrotechnik*, **69**:321–325, 1986. doi: 10.1007/BF01574747.
- [112] T. Kalkbrenner, M. Ramstein, J. Mlynek, and V. Sandoghdar. *A single gold particle as a probe for apertureless scanning near-field optical microscopy*. *Journal of Microscopy*, **202**(1):72–76, 2001. doi: 10.1046/j.1365-2818.2001.00817.x.
- [113] Z. H. Kim and S. R. Leone. *High-resolution apertureless near-field optical imaging using gold nanosphere probes*. *The Journal of Physical Chemistry B*, **110**(40):19804–19809, 2006. doi: 10.1021/jp061398+.
- [114] J.-J. Greffet. *Nanoantennas for light emission*. *Science*, **308**(5728):1561–1563, 2005. doi: 10.1126/science.1113355.
- [115] T. H. Taminiau, F. D. Stefani, F. B. Segerink, and N. F. van Hulst. *Optical antennas direct single-molecule emission*. *Nature Photonics*, **2**:234 – 237, 2008. doi: 10.1038/nphoton.2008.32.
- [116] B. Lounis and M. Orrit. *Single-photon sources*. *Reports on Progress in Physics*, **68**(5):1129, 2005. doi: 10.1088/0034-4885/68/5/R04.
- [117] H. Giessen and M. Lippitz. *Directing light emission from quantum dots*. *Science*, **329**(5994):910–911, 2010. doi: 10.1126/science.1194352.

-
- [118] L. Novotny. *Effective wavelength scaling for optical antennas*. Physical Review Letters, **98**:266802, 2007. doi: 10.1103/PhysRevLett.98.266802.
- [119] T. H. Taminiau, F. D. Stefani, and N. F. van Hulst. *Optical nanorod antennas modeled as cavities for dipolar emitters: Evolution of sub- and super-radiant modes*. Nano Letters, **11**(3):1020–1024, 2011. doi: 10.1021/nl103828n.
- [120] R. Esteban, T. V. Teperik, and J. J. Greffet. *Optical patch antennas for single photon emission using surface plasmon resonances*. Physical Review Letters, **104**:026802, 2010. doi: 10.1103/PhysRevLett.104.026802.
- [121] J. Li, A. Salandrino, and N. Engheta. *Shaping light beams in the nanometer scale: A Yagi-Uda nanoantenna in the optical domain*. Physical Review B, **76**:245403, 2007. doi: 10.1103/PhysRevB.76.245403.
- [122] T. Pakizeh and M. Käll. *Unidirectional ultracompact optical nanoantennas*. Nano Letters, **9**(6):2343–2349, 2009. doi: 10.1021/nl900786u.
- [123] M. Righini, P. Ghenuche, S. Cherukulappurath, V. Myroshnychenko, F. J. Garcia de Abajo, and R. Quidant. *Nano-optical trapping of Rayleigh particles and Escherichia coli bacteria with resonant optical antennas*. Nano Letters, **9**(10):3387–3391, 2009. doi: 10.1021/nl803677x.
- [124] M. Schnell, A. Garcia-Etxarri, A. J. Huber, K. B. Crozier, A. Borisov, J. Aizpurua, and R. Hillenbrand. *Amplitude- and phase-resolved near-field mapping of infrared antenna modes by transmission-mode scattering-type near-field microscopy*. The Journal of Physical Chemistry C, **114**(16):7341–7345, 2010. doi: 10.1021/jp909252z.
- [125] S. C. Schneider, S. Grafström, and L. M. Eng. *Scattering near-field optical microscopy of optically anisotropic systems*. Physical Review B, **71**(11):115418, 2005. doi: 10.1103/PhysRevB.71.115418.
- [126] H. Yagi. *Beam transmission of ultra short waves*. Proceedings of the Institute of Radio Engineers, **16**(6):715 – 740, 1928. doi: 10.1109/JRPROC.1928.221464.
- [127] T. H. Taminiau, F. D. Stefani, and N. F. van Hulst. *Enhanced directional excitation and emission of single emitters by a nano-optical Yagi-Uda antenna*. Optics Express, **16**(14):10858–10866, 2008. doi: 10.1364/OE.16.010858.
- [128] T. Kosako, Y. Kadoya, and H. F. Hofmann. *Directional control of light by a nano-optical Yagi-Uda antenna*. Nature Photonics, **4**:312–315, 2010. doi: 10.1038/nphoton.2010.34.

- [129] A. Ahmed and R. Gordon. *Directivity enhanced Raman spectroscopy using nanoantennas*. Nano Letters, **11**(4):1800–1803, 2011. doi: 10.1021/nl200461w.
- [130] R. W. P. King, G. J. Fikioris, and R. B. Mack. *Cylindrical Antennas and Arrays, 2nd ed.* Cambridge University Press, 2002.
- [131] S. A. Shelkunoff. *The impedance concept and its application to problems of reflection, shielding and power absorption*. Bell System Technical Journal, **17**:17–48, 1938.
- [132] T. P. Meyrath, T. Zentgraf, and H. Giessen. *Lorentz model for metamaterials: Optical frequency resonance circuits*. Phys. Rev. B, **75**:205102, 2007. doi: 10.1103/PhysRevB.75.205102.
- [133] J.-S. Huang, T. Feichtner, P. Biagioni, and B. Hecht. *Impedance matching and emission properties of nanoantennas in an optical nanocircuit*. Nano Letters, **9**(5):1897–1902, 2009. doi: 10.1021/nl803902t.
- [134] S. Linden, J. Kuhl, and H. Giessen. *Controlling the interaction between light and gold nanoparticles: Selective suppression of extinction*. Physical Review Letters, **86**:4688–4691, 2001. doi: 10.1103/PhysRevLett.86.4688.
- [135] W. Nomura, M. Ohtsu, and T. Yatsui. *Nanodot coupler with a surface plasmon polariton condenser for optical far/near-field conversion*. Applied Physics Letters, **86**(18):181108, 2005. doi: 10.1063/1.1920419.
- [136] A. Rashidi and H. Mosallaei. *Array of plasmonic particles enabling optical near-field concentration: A nonlinear inverse scattering design approach*. Physical Review B, **82**:035117, 2010. doi: 10.1103/PhysRevB.82.035117.
- [137] M. I. Stockman, D. J. Bergman, and T. Kobayashi. *Coherent control of nanoscale localization of ultrafast optical excitation in nanostructures*. In *Conference on Lasers and Electro-Optics*, p. QMJ4. Optical Society of America, 2003.
- [138] M. Aeschlimann, M. Bauer, D. Bayer, T. Brixner, F. J. G. de Abajo, W. Pfeiffer, M. Rohmer, C. Spindler, and F. Steeb. *Adaptive subwavelength control of nano-optical fields*. Nature, **446**:301–304, 2007. doi: 10.1038/nature05595.
- [139] G. Volpe, S. Cherukulappurath, R. Juanola Parramon, G. Molina-Terriza, and R. Quidant. *Controlling the optical near field of nanoantennas with spatial phase-shaped beams*. Nano Letters, **9**(10):3608–3611, 2009. doi: 10.1021/nl901821s.

-
- [140] B. Gjonaj, J. Aulbach, P. M. Johnson, A. P. Mosk, L. Kuipers, and A. Lagendijk. *Active spatial control of plasmonic fields*. Nature Photonics, **5**:360–363, 2011. doi: 10.1038/nphoton.2011.57.
- [141] M. W. Knight, N. K. Grady, R. Bardhan, F. Hao, P. Nordlander, and N. J. Halas. *Nanoparticle-mediated coupling of light into a nanowire*. Nano Letters, **7**(8):2346–2350, 2007. doi: 10.1021/nl071001t.
- [142] M. Esslinger and R. Vogelgesang. *Reciprocity theory of apertureless scanning near-field optical microscopy with point-dipole probes*. ACS Nano, **6**(9):8173–8182, 2012. doi: 10.1021/nn302864d.
- [143] Z. Fang, L. Fan, C. Lin, D. Zhang, A. J. Meixner, and X. Zhu. *Plasmonic coupling of bow tie antennas with Ag nanowire*. Nano Letters, **11**(4):1676–1680, 2011. doi: 10.1021/nl200179y.
- [144] M.-D. He, J.-Q. Liu, Z.-Q. Gong, S. Li, and Y.-F. Luo. *Directional excitation of surface plasmon polaritons in structure of subwavelength metallic holes*. Optics Communications, **285**(2):182 – 185, 2012. doi: 10.1016/j.optcom.2011.09.020.
- [145] H. L. Offerhaus, B. van den Bergen, M. Escalante, F. B. Segerink, J. P. Korterik, and N. F. van Hulst. *Creating focused plasmons by noncollinear phasematching on functional gratings*. Nano Letters, **5**(11):2144–2148, 2005. doi: 10.1021/nl0515089.
- [146] G. Lerosey. *Nano-optics: Yagi-Uda antenna shines bright*. Nature Photonics, **4**:267–268, 2010. doi: 10.1038/nphoton.2010.78.
- [147] K. F. MacDonald, Z. L. Samson, M. I. Stockman, and N. I. Zheludev. *Ultrafast active plasmonics*. Nature Photonics, **3**:55–58, 2009. doi: 10.1038/nphoton.2008.249.
- [148] C. Enkrich, G. Dolling, M. W. Klein, J. Zhou, T. Koschny, C. M. Soukoulis, S. Burger, F. Schmidt, and M. Wegener. *Photonic metamaterials: Magnetism at optical frequencies*. IEEE Journal of Selected Topics in Quantum Electronics, **12**:1097–1105, 2006. doi: 10.1109/JSTQE.2006.880600.
- [149] J. K. Gansel, M. Thiel, M. S. Rill, M. Decker, K. Bade, V. Saile, G. von Freymann, S. Linden, and M. Wegener. *Gold helix photonic metamaterial as broadband circular polarizer*. Science, **325**(5947):1513–1515, 2009. doi: 10.1126/science.1177031.
- [150] L. V. Alekseyev, E. E. Narimanov, T. Tumkur, H. Li, Y. A. Barnakov, and M. A. Noginov. *Uniaxial epsilon-near-zero metamaterial for angular filtering and polarization control*. Applied Physics Letters, **97**:131107–131107–3, 2010. doi: 10.1063/1.3469925.

- [151] V. M. Shalaev. *Optical negative-index metamaterials*. Nature Photonics, **1**:41–48, 2007. doi: 10.1038/nphoton.2006.49.
- [152] W. L. Barnes, A. Dereux, and T. W. Ebbesen. *Surface plasmon subwavelength optics*. Nature, **424**:824–830, 2003. doi: 10.1038/nature01937.
- [153] S. Lal, S. Link, and N. J. Halas. *Nano-optics from sensing to waveguiding*. Nature Photonics, **1**:641–648, 2007. doi: 10.1038/nphoton.2007.223.
- [154] C. Tabor, R. Murali, M. Mahmoud, and M. A. El-Sayed. *On the use of plasmonic nanoparticle pairs as a plasmon ruler: The dependence of the near-field dipole plasmon coupling on nanoparticle size and shape*. The Journal of Physical Chemistry A, **113**(10):1946–1953, 2009. doi: 10.1021/jp807904s.
- [155] A. M. Funston, C. Novo, T. J. Davis, and P. Mulvaney. *Plasmon coupling of gold nanorods at short distances and in different geometries*. Nano Letters, **9**(4):1651–1658, 2009. doi: 10.1021/nl900034v.
- [156] C. Tabor, D. Van Haute, and M. A. El-Sayed. *Effect of orientation on plasmonic coupling between gold nanorods*. ACS Nano, **3**(11):3670–3678, 2009. doi: 10.1021/nn900779f.
- [157] M. L. Sandrock and C. A. Foss. *Synthesis and linear optical properties of nanoscopic gold particle pair structures*. The Journal of Physical Chemistry B, **103**(51):11398–11406, 1999. doi: 10.1021/jp992176x.
- [158] H. Tamaru, H. Kuwata, H. T. Miyazaki, and K. Miyano. *Resonant light scattering from individual Ag nanoparticles and particle pairs*. Applied Physics Letters, **80**:1826, 2002. doi: 10.1063/1.1461072.
- [159] W. Rechberger, A. Hohenau, A. Leitner, J. Krenn, B. Lamprecht, and F. Aussenegg. *Optical properties of two interacting gold nanoparticles*. Optics Communications, **220**:137 – 141, 2003. doi: 10.1016/S0030-4018(03)01357-9.
- [160] K.-H. Su, Q.-H. Wei, X. Zhang, J. J. Mock, D. R. Smith, and S. Schultz. *Interparticle coupling effects on plasmon resonances of nanogold particles*. Nano Letters, **3**(8):1087–1090, 2003. doi: 10.1021/nl034197f.
- [161] T. Atay, J.-H. Song, and A. V. Nurmikko. *Strongly interacting plasmon nanoparticle pairs: From dipole–dipole interaction to conductively coupled regime*. Nano Letters, **4**(9):1627–1631, 2004. doi: 10.1021/nl049215n.
- [162] P. K. Jain, S. Eustis, and M. A. El-Sayed. *Plasmon coupling in nanorod assemblies: Optical absorption, discrete dipole approximation simulation, and exciton-coupling model*. The Journal of Physical Chemistry B, **110**(37):18243–18253, 2006. doi: 10.1021/jp063879z.

-
- [163] I. Romero, J. Aizpurua, G. W. Bryant, and F. J. G. D. Abajo. *Plasmons in nearly touching metallic nanoparticles: singular response in the limit of touching dimers*. Optics Express, **14**(21):9988–9999, 2006. doi: 10.1364/OE.14.009988.
- [164] C. Helgert, C. Rockstuhl, C. Etrich, C. Menzel, E.-B. Kley, A. Tünnermann, F. Lederer, and T. Pertsch. *Effective properties of amorphous metamaterials*. Physical Review B, **79**:233107, 2009. doi: 10.1103/PhysRevB.79.233107.
- [165] N. Papasimakis, V. A. Fedotov, Y. H. Fu, D. P. Tsai, and N. I. Zheludev. *Coherent and incoherent metamaterials and order-disorder transitions*. Physical Review B, **80**:041102, 2009. doi: 10.1103/PhysRevB.80.041102.
- [166] M. W. Knight, J. Fan, F. Capasso, and N. J. Halas. *Influence of excitation and collection geometry on the dark field spectra of individual plasmonic nanostructures*. Optics Express, **18**(3):2579–2587, 2010. doi: 10.1364/OE.18.002579.
- [167] H. Fredriksson, Y. Alaverdyan, A. Dmitriev, C. Langhammer, D. Sutherland, M. Zäch, and B. Kasemo. *Hole-mask colloidal lithography*. Advanced Materials, **19**(23):4297–4302, 2007. doi: 10.1002/adma.200700680.
- [168] M. I. Stockman, S. V. Faleev, and D. J. Bergman. *Localization versus delocalization of surface plasmons in nanosystems: Can one state have both characteristics?* Physical Review Letters, **87**:167401, 2001. doi: 10.1103/PhysRevLett.87.167401.
- [169] W. Khunsin, B. Brian, J. Dorfmüller, M. Esslinger, R. Vogelgesang, C. Etrich, C. Rockstuhl, A. Dmitriev, and K. Kern. *Long-distance indirect excitation of nanoplasmonic resonances*. Nano Letters, **11**(7):2765–2769, 2011. doi: 10.1021/nl201043v.
- [170] B. Lamprecht, G. Schider, R. T. Lechner, H. Ditlbacher, J. R. Krenn, A. Leitner, and F. R. Aussenegg. *Metal nanoparticle gratings: Influence of dipolar particle interaction on the plasmon resonance*. Physical Review Letters, **84**:4721–4724, 2000. doi: 10.1103/PhysRevLett.84.4721.
- [171] J. A. Schuller, E. S. Barnard, W. Cai, Y. C. Jun, J. S. White, and M. L. Brongersma. *Plasmonics for extreme light concentration and manipulation*. Nature Materials, **9**:193–204, 2010. doi: 10.1038/nmat2630.
- [172] J. J. Hopfield. *Theory of the contribution of excitons to the complex dielectric constant of crystals*. Physical Review, **112**:1555–1567, 1958. doi: 10.1103/PhysRev.112.1555.

- [173] C. M. Soukoulis and M. Wegener. *Past achievements and future challenges in the development of three-dimensional photonic metamaterials*. Nature Photonics, **5**:523–530, 2011. doi: 10.1038/nphoton.2011.154.
- [174] B. Deveaud-Plédran. *Solid-state physics: Polaritronics in view*. Nature, **453**:297–298, 2008. doi: 10.1038/453297a.
- [175] S. I. Tsintzos, N. T. Pelekanos, G. Konstantinidis, Z. Hatzopoulos, and P. G. Savvidis. *A GaAs polariton light-emitting diode operating near room temperature*. Nature, **453**:372–375, 2008. doi: 10.1038/nature06979.
- [176] M. Beresna, M. Gecevičius, P. G. Kazansky, T. Taylor, and A. V. Kavokin. *Exciton mediated self-organization in glass driven by ultrashort light pulses*. Applied Physics Letters, **101**(5):053120, 2012. doi: 10.1063/1.4742899.
- [177] J. C. Prangma, J. Kern, A. G. Knapp, S. Grossmann, M. Emmerling, M. Kamp, and B. Hecht. *Electrically connected resonant optical antennas*. Nano Letters, **12**(8):3915–3919, 2012. doi: 10.1021/nl3007374.
- [178] D. Koller, A. Hohenau, H. Ditlbacher, N. Galler, F. Reil, F. Aussenegg, A. Leitner, E. List, and J. J.R. Krenn. *Organic plasmon-emitting diode*. Nature Photonics, **2**:684–687, 2008. doi: 10.1038/nphoton.2008.200.
- [179] P. Bharadwaj, A. Bouhelier, and L. Novotny. *Electrical excitation of surface plasmons*. Physical Review Letters, **106**:226802, 2011. doi: 10.1103/PhysRevLett.106.226802.
- [180] M. W. Knight, H. Sobhani, P. Nordlander, and N. J. Halas. *Photodetection with active optical antennas*. Science, **332**(6030):702–704, 2011. doi: 10.1126/science.1203056.
- [181] D. W. Pohl, S. G. Rodrigo, and L. Novotny. *Stacked optical antennas*. Applied Physics Letters, **98**(2):023111–023111–3, 2011. doi: 10.1063/1.3541544.
- [182] F. H. L. Koppens, D. E. Chang, and F. J. Garcia de Abajo. *Graphene plasmonics: A platform for strong light-matter interactions*. Nano Letters, **11**(8):3370–3377, 2011. doi: 10.1021/nl201771h.
- [183] R. Warmbier, G. S. Manyali, and A. Quandt. *Surface plasmon polaritons in lossy uniaxial anisotropic materials*. Physical Review B, **85**:085442, 2012. doi: 10.1103/PhysRevB.85.085442.
- [184] D.-H. Chae, T. Utikal, S. Weisenburger, H. Giessen, K. v. Klitzing, M. Lipitz, and J. Smet. *Excitonic Fano resonance in free-standing graphene*. Nano Letters, **11**(3):1379–1382, 2011. doi: 10.1021/nl200040q.

-
- [185] A. G. Marinopoulos, L. Reining, V. Olevano, A. Rubio, T. Pichler, X. Liu, M. Knupfer, and J. Fink. *Anisotropy and interplane interactions in the dielectric response of graphite*. Physical Review Letters, **89**:076402, 2002. doi: 10.1103/PhysRevLett.89.076402.
- [186] D. Greenaway and G. Harbeke. *Band structure of bismuth telluride, bismuth selenide and their respective alloys*. Journal of Physics and Chemistry of Solids, **26**(10):1585 – 1604, 1965. doi: 10.1016/0022-3697(65)90092-2.
- [187] A. D. LaForge, A. Frenzel, B. C. Pursley, T. Lin, X. Liu, J. Shi, and D. N. Basov. *Optical characterization of bi_2se_3 in a magnetic field: Infrared evidence for magnetoelectric coupling in a topological insulator material*. Physical Review B, **81**:125120, 2010. doi: 10.1103/PhysRevB.81.125120.
- [188] H. M. Benia, C. Lin, K. Kern, and C. R. Ast. *Reactive chemical doping of the bi_2se_3 topological insulator*. Physical Review Letters, **107**:177602, 2011. doi: 10.1103/PhysRevLett.107.177602.
- [189] H. Zhang, C.-X. Liu, X.-L. Qi, X. Dai, Z. Fang, and S.-C. Zhang. *Topological insulators in Bi_2Se_3 , Bi_2Te_3 and Sb_2Te_3 with a single Dirac cone on the surface*. Nature Physics, **5**:438 – 442, 2009. doi: 10.1038/nphys1270.
- [190] V. N. Lyobimov and D. G. Sannikov. *Surface electromagnetic waves in a uniaxial crystal*. Soviet Physics - Solid State, **14**:575–579, 1972.
- [191] D. Kong, J. C. Randel, H. Peng, J. J. Cha, S. Meister, K. Lai, Y. Chen, Z.-X. Shen, H. C. Manoharan, and Y. Cui. *Topological insulator nanowires and nanoribbons*. Nano Letters, **10**(1):329–333, 2010. doi: 10.1021/nl903663a.
- [192] B. F. Gao, P. Gehring, M. Burghard, and K. Kern. *Gate-controlled linear magnetoresistance in thin Bi_2Se_3 sheets*. Applied Physics Letters, **100**(21):212402, 2012. doi: 10.1063/1.4719196.
- [193] T. H. Taminiau, F. D. Stefani, and N. F. van Hulst. *Optical nanorod antennas modeled as cavities for dipolar emitters: Evolution of sub- and super-radiant modes*. Nano Letters, **11**(3):1020–1024, 2011. doi: 10.1021/nl103828n.
- [194] P. G. Etchegoin, E. C. L. Ru, and M. Meyer. *An analytic model for the optical properties of gold*. The Journal of Chemical Physics, **125**(16):164705, 2006. doi: 10.1063/1.2360270.
- [195] P. Tirkas, C. Balanis, and R. Renaut. *Higher order absorbing boundary conditions for the finite-difference time-domain method*. Antennas and Propagation, IEEE Transactions on, **40**(10):1215 –1222, 1992. doi: 10.1109/8.182454.

- [196] A. Karch. *Surface plasmons and topological insulators*. Phys. Rev. B, **83**:245432, 2011. doi: 10.1103/PhysRevB.83.245432.
- [197] O. Roslyak, G. Gumbs, and D. H. Huang. *Plasmons in single- and double-component helical liquids: Application to two-dimensional topological insulators*. arXiv, **1201**:2359, 2012.
- [198] Z. Zhu and T. Brown. *Full-vectorial finite-difference analysis of microstructured optical fibers*. Opt. Express, **10**(17):853–864, 2002.
- [199] E. J. Lee, K. Balasubramanian, J. Dorfmueller, R. Vogelgesang, N. Fu, A. Mews, M. Burghard, and K. Kern. *Electronic-band-structure mapping of nanotube transistors by scanning photocurrent microscopy*. Small, **3**(12):2038–2042, 2007. doi: 10.1002/sml.200700418.
- [200] H. Yuan, H. Liu, H. Shimotani, H. Guo, M. Chen, Q. Xue, and Y. Iwasa. *Liquid-gated ambipolar transport in ultrathin films of a topological insulator Bi_2Te_3* . Nano Letters, **11**(7):2601–2605, 2011. doi: 10.1021/nl201561u.
- [201] I. Fischer, M. Esslinger, R. Vogelgesang, J.-L. Wu, and J. Schulze. *CMOS-compatible plasmon propagation and detection in vertical Si and Ge p-i-n diodes*. Silicon-Germanium Technology and Device Meeting (ISTDM), 2012 International, pp. 1 –2, 2012. doi: 10.1109/ISTDM.2012.6222415.
- [202] H. A. Atwater and A. Polman. *Plasmonics for improved photovoltaic devices*. Nature Materials, **9**:205–213, 2010. doi: 10.1038/nmat2629.
- [203] K. R. Catchpole, S. Mokkaapati, F. Beck, E.-C. Wang, A. McKinley, A. Basch, and J. Lee. *Plasmonics and nanophotonics for photovoltaics*. MRS Bulletin, **36**:461–467, 2011. doi: 10.1557/mrs.2011.132.
- [204] H. Shen, P. Bienstman, and B. Maes. *Plasmonic absorption enhancement in organic solar cells with thin active layers*. Journal of Applied Physics, **106**(7):073109, 2009. doi: 10.1063/1.3243163.
- [205] Y. Akimov, W. Koh, and K. Ostrikov. *Enhancement of optical absorption in thin-film solar cells through the excitation of higher-order nanoparticle plasmon modes*. Optics Express, **17**(12):10195–10205, 2009. doi: 10.1364/oe.17.010195.
- [206] R. F. Wallis, J. J. Brion, E. Burstein, and A. Hartstein. *Theory of surface polaritons in anisotropic dielectric media with application to surface magnetoplasmons in semiconductors*. Physical Review B, **9**:3424–3437, 1974. doi: 10.1103/PhysRevB.9.3424.

-
- [207] Y. Chevalier, M. Louzar, and G. A. Maugin. *Surface-wave characterization of the interface between two anisotropic media*. The Journal of the Acoustical Society of America, **90**(6):3218–3227, 1991. doi: 10.1121/1.401431.
- [208] M. Liscidini and J. E. Sipe. *Quasiguidded surface plasmon excitations in anisotropic materials*. Physical Review B, **81**:115335, 2010. doi: 10.1103/PhysRevB.81.115335.
- [209] S. A. Ramakrishna, J. B. Pendry, M. C. K. Wiltshire, and W. J. Stewart. *Imaging the near field*. Journal of Modern Optics, **50**(9):1419–1430, 2003. doi: 10.1080/09500340308235215.
- [210] A. Alù and N. Engheta. *Wireless at the nanoscale: Optical interconnects using matched nanoantennas*. Physical Review Letters, **104**:213902, 2010. doi: 10.1103/PhysRevLett.104.213902.
- [211] A. Yaghjian. *An overview of near-field antenna measurements*. IEEE Transactions on Antennas and Propagation, **34**(1):30 – 45, 1986. doi: 10.1109/TAP.1986.1143727.
- [212] A. C. Jones, R. L. Olmon, S. E. Skrabalak, B. J. Wiley, Y. N. Xia, and M. B. Raschke. *Mid-IR plasmonics: Near-field imaging of coherent plasmon modes of silver nanowires*. Nano Letters, **9**(7):2553–2558, 2009. doi: 10.1021/nl900638p.
- [213] M. Schnell, A. Garcia-Etxarri, A. J. Huber, K. Crozier, J. Aizpurua, and R. Hillenbrand. *Controlling the near-field oscillations of loaded plasmonic nanoantennas*. Nature Photonics, **3**:287–291, 2009. doi: 10.1038/nphoton.2009.46.
- [214] S. Nie and S. R. Emory. *Probing single molecules and single nanoparticles by surface-enhanced Raman scattering*. Science, **275**(5303):1102–1106, 1997. doi: 10.1126/science.275.5303.1102.
- [215] I. Khan, D. Cunningham, S. Lazar, D. Graham, W. Ewen Smith, and D. W. McComb. *A TEM and electron energy loss spectroscopy (EELS) investigation of active and inactive silver particles for surface enhanced resonance raman spectroscopy (SERRS)*. Faraday Discussions, **132**:171–178, 2006. doi: 10.1039/b506644a.
- [216] M. A. van Dijk, M. Lippitz, and M. Orrit. *Detection of acoustic oscillations of single gold nanospheres by time-resolved interferometry*. Physical Review Letters, **95**:267406, 2005. doi: 10.1103/PhysRevLett.95.267406.

Acknowledgements

I want to acknowledge everyone who contributed to this thesis and without whom this work would not have been possible.

I want to thank Klaus Kern for the opportunity to write my thesis in his department and constructive criticism on my work.

I also want to thank Prof. Cécile Hébert, Prof. Olivier Martin, Prof. Christian Hafner and Prof. Christoph Lienau for agreeing to be on my thesis jury.

My group leader Ralf Vogelgesang for guidance throughout the thesis, for advice, teaching me a lot, for his support with MMP simulations and for a lot more.

Worawut Khunsin and Jens Dorfmueller for teaching me how to use the machine, sharing measurement time and ideas, working together on projects, and many memorable free time activities.

Matthias Brandstetter and Marcus Rommel for many discussions, the friendly atmosphere in the lab, and also a lot of fun besides work.

Nahid Talebi for fruitful contributions and support with finite difference numerical methods.

Tongda Wei for helping me with measurements.

Markus Oster and Jyh-Lih Wu for their help on projects on the confocal setup.

The ultrafast nanooptics group, specifically Markus Lippitz, Thorsten Schumacher, and Klas Lindfors for being very supportive.

My office-mates Thomas Weitz, Stephan Rauschenbach, Thomas Dufaux, Thomas Maurer, Sören Krotzky, Pascal Gehring, and Sina Habibian for the great time.

All other coauthors and collaborators: Daniel Dregely, Harald Giessen, Christoph Etrich, Carsten Rockstuhl, Björn Brian, Alexandre "Sascha" Dmitriev, Bruno Gompf, Stefano de Zuani, Inga Fischer, Ma Dongling, Yong Qin, and Mato Knez for supporting my work or allowing me to contribute to theirs.

The cleanroom service group Thomas Reindl, Ulrike Waizmann, Marion Hagel, and

Bibliography

Bernhard Fenk for their patience and help.

Sebastian Stepanow for being expert on my 1-year exam and a nice trip to Lausanne.

Everyone in the department. It was fun to work with you.

My school physics teacher Andreas Drechsel, who laid the foundation of my physics education.

I want to thank my wife and my parents, who were always there for me.

And all the people I have forgotten here.

Appendix A.

Publications and Curriculum Vitae

A.1. Publications

- C. Wagner, D. Kasemann, C. Golnik, R. Forker, M. Esslinger, K. Müllen, and T. Fritz. *Repulsion between molecules on a metal: Monolayers and submonolayers of hexa-peri-hexabenzocoronene on Au(111)*. Phys. Rev. B, **81**:035423, 2010. doi: 10.1103/PhysRevB.81.035423.
- W. Khunsin, B. Brian, J. Dorfmueller, M. Esslinger, R. Vogelgesang, C. Etrich, C. Rockstuhl, A. Dmitriev, and K. Kern. *Long-distance indirect excitation of nanoplasmonic resonances*. Nano Letters, **11**(7):2765–2769, 2011. doi: 10.1021/nl201043v.
- J. Dorfmueller, D. Dregely, M. Esslinger, W. Khunsin, R. Vogelgesang, K. Kern, and H. Giessen. *Near-field dynamics of optical Yagi-Uda nanoantennas*. Nano Letters, **11**(7):2819–2824, 2011. doi: 10.1021/nl201184n.
- M. Esslinger, J. Dorfmueller, W. Khunsin, R. Vogelgesang, and K. Kern. *Background-free imaging of plasmonic structures with cross-polarized apertureless scanning near-field optical microscopy*. Review of Scientific Instruments, **83**(3):033704, 2012. doi: 10.1063/1.3693346.
- I. Fischer, M. Esslinger, R. Vogelgesang, J.-L. Wu, and J. Schulze. *CMOS-compatible plasmon propagation and detection in vertical Si and Ge p-i-n diodes*. Silicon-Germanium Technology and Device Meeting (ISTDM), 2012 International, pp. 1–2, 2012. doi: 10.1109/ISTDM.2012.6222415.
- Y. Qin, R. Vogelgesang, M. Eßlinger, W. Sigle, P. van Aken, O. Moutanabbir, and M. Knez. *Bottom-up tailoring of plasmonic nanopeapods making use of the periodical topography of carbon nanocoil templates*. Advanced Functional Materials, **22**(24):5157–5165, 2012. doi: 10.1002/adfm.201201791.
- M. Esslinger and R. Vogelgesang. *Reciprocity theory of apertureless scanning near-field optical microscopy with point-dipole probes*. ACS Nano, **6**(9):8173–8182, 2012. doi: 10.1021/nm302864d.

- M. Esslinger, Worawut Khunsin, N. Talebi, T. Wei, J. Dorfmueller, R. Vogelgesang, and K. Kern. *Phase Engineering of Subwavelength Unidirectional Plasmon Launchers*. (submitted)
- M. Esslinger, R. Vogelgesang, N. Talebi, W. Khunsin, P.l Gehring, S. de Zuani, B. Gompf, and K. Kern. *Anisotropic Polaritonics at Optical Frequencies*. (in preparation)

A.2. Curriculum Vitae

Name

Name	Moritz Eßlinger
Date of Birth	December 06, 1984
Place of Birth	Ludwigsburg, Germany
Nationality	German

School education

1991 - 1993	Grundschule Rohrhof
1993 - 1994	Schillerschule Grund- und Hauptschule Brühl
1994 - 1995	Grundschule Bernhard Kellermann Freiberg
1995 - 2003	Geschwister-Scholl-Gymnasium Freiberg

Military Service

2003 - 2004	Compulsory military service in Erfurt and Chemnitz
-------------	--

University Education

2004 - 2009	Studies of Physics at the University of Technology Dresden
2008 - 2009	Diploma thesis in the group of Prof. Karl Leo at the Institut für angewandte Photophysik (IAPP) Dresden Title: <i>Hexa-peri-hexabenzocoronene auf Gold als Grundlage für organisch-organische heteroepitaktische Systeme</i>

Professional Experience

2009 - 2013	PhD Student in the Group of Prof. Kern at the Max Planck Institute for Solid State Research, Stuttgart, Germany
-------------	---